Diese Arbeit wurde vorgelegt am Institut für Quanteninformation.
The present work was submitted to the Institute for Quantum Information.

Spin-Coherent Conveyor-Mode Shuttling of Electrons in Si/SiGe

by
Tobias Offermann

Master's Thesis in Physics

presented to

The Faculty of Mathematics, Computer Science and Natural Sciences at RWTH Aachen University

Department of Physics, Institute II C

October 2023

supervised by

Dr. Lars Schreiber
Prof. Hendrik Bluhm, PhD
PD Dr. Alexander Pawlis

Abstract

The pursuit of efficient quantum computation relies on the development of scalable quantum computing architectures. This master's thesis explores the realm of spin qubit shuttle (SQS) devices as a mid-range coherent link within such architectures. Through meticulous experimentation and analysis, this study investigates the spin coherence and decoherence dynamics of electrons in Si/-SiGe heterostructures, coupled with the assessment of valley splitting and characterization of various heterostructure configurations.

Operating within a cryogenic environment at millikelvin temperatures, the research delves into the behavior of SQS, focusing on coherent shuttling of spin states over distances up to several micrometers. A significant outcome is the observation of indications of motional narrowing, highlighting the coherent nature of electron transport within the device.

The primary objectives of this master's thesis encompass the identification of suitable experimental devices, the comparative assessment of distinct Si/SiGe heterostructures, and the comprehensive examination and theoretical description of electron spin coherence and motional narrowing. The outcomes of this work bear implications for the realization of scalable quantum computing paradigms based on spin qubits. By attaining coherent shuttling capabilities, a significant advancement has been achieved towards the implementation of practical and scalable quantum computation architectures.

Acknowledgements

First and foremost, I want to thank Lars Schreiber. His guidance throughout the whole research phase was outstanding, and I'm sincerely grateful for the efforts he made to integrate me into the scientific community early in my career. I also want to thank Hendrik Bluhm for allowing me to conduct my research in his group and for the fruitful discussions about my work. Further, I want to acknowledge Alexander Pawlis for willingly agreeing to be my second examiner.

I am enormously grateful for having had Tom Struck and Mats Volmer, or as we call ourselves, the 'coherent colleagues', as my supervisors. As the trio of the Nirvana Lab, we not only studied countless oscillations, but we also oscillated through highs (such as the first results showing spin-coherent shuttling) and lows (like scaffolds unexpectedly appearing in our lab and damaging our sample) together. I will never forget all our discussions ranging from spin-qubit physics to the probability of God existing, and I couldn't have wished for better supervisors.

Furthermore, my gratitude runs deep for having had the chance to work alongside Arnau Sala during the measurements at 4 K. From long nights at the Himmel Lab working on single measurements to almost industrializing the pre-screening procedure, the journey has been truly rewarding. During all these measurements, we not only glued and bonded samples but also glued together and bonded as a team. An essential part of this team includes Denny Dütz and Sammy Umezawa, whom I thank for their significant help with the measurements. Additionally, I appreciate the efforts of Malte Neul, Lino Visser, and especially Max Beer for introducing us to the setup and assisting in getting the measurements up and running.

The clarity and coherence of this thesis owe much to my diligent proofreaders: Nils Ciroth, Lukas Delventhal, Sarah Friedrich, Michelle Hoock, Patricia Pesch, Norbert Rahn, Arnau Sala, Tom Struck and Mats Volmer. Their insights and meticulous attention have been invaluable. Moreover, I want to thank Victor Schwan for keeping me company during those late-night writing sessions.

Last but not least, my heartfelt thanks go to my family, who've stood by my side not just this past year, but throughout every step of my life. Without their constant support and belief in me, I surely wouldn't be where I am today.

Additionally, a nod to coffee, my silent partner in countless endeavors - you've fueled late-night epiphanies and kick-started many early mornings. Thank you for being a constant in the whirlwind of research and writing.

Publications

Some of the research conducted during the course of this thesis has been disseminated in the following forms:

Papers

1. Tom Struck, Mats Volmer, Lino Visser, **Tobias Offermann**, Ran Xue, Jhih-Sian Tu, Stefan Trellenkamp, Łukasz Cywiński, Hendrik Bluhm and Lars R. Schreiber (2023). *Spin-EPR-pair separation by conveyor-mode single electron shuttling in Si/SiGe*. Under review at *Nature Communications*. Preprint available at arXiv:2307.04897.

Conference Presentations

1. **Tobias Offermann**, Tom Struck, Lino Visser, Mats Volmer, Ran Xue, Hendrik Bluhm and Lars R. Schreiber (2023). *Coherent Conveyor Mode Shuttling of Electrons and their Spin*. DPG Spring Meeting of the Condensed Matter Section, Dresden, Germany.

Contents

List of Figures

List of Tables

List of Abbreviations

1DEC one-dimensional electron channel

2DEG two-dimensional electron gas

ALD atomic layer deposition

AWG arbitrary waveform generator

CSD charge stability diagram

DQD double quantum dot

EPR Einstein-Podolsky-Rosen

FCP frequency correlation plot

GA gradient accumulation

hf hyperfine interactions

HS heterostructure

LD Loss-DiVincenzo

LIA Lock-in amplifier

MN motional narrowing

PCB printed circuit board

PSB Pauli spin blockade

QD quantum dot

QW quantum well

RF radio frequency

SEM scanning electron microscope

SET single electron transistor

SMU Source Measure Unit

SQS spin qubit shuttle

SE standard error

TMA trimethylaluminum

ttf tuning toolkit framework

Chapter 1

Introduction

1.1 Motivation

Moore's Law, the compass guiding decades of exponential classical computing prowess through the consistent doubling of transistor counts on integrated circuits approximately every two years, now finds itself on the brink of its own limitations [1–3]. As the constraints stemming from the physical attributes of semiconductor technology become progressively apparent [4–6], a resounding call emerges to embrace quantum computing as the pivotal successor. This quantum revolution bears the promise not only to navigate around these constraints but also to perpetuate and amplify the trajectory of computational advancement.

With this, it has the potential to guide us into the next generation of computing, possibly solving some of the hardest problems efficiently. First sources already report a quantum advantage in comparison to classical computers [7, 8]. In order to solve genuine problems, we need quantum computers with up to a million quantum bits [9], so called qubits, which is the smallest unit of information in a quantum computer and therefore the analogue to bits in a classical computer [10].

While all of the necessary ingredients to build such a quantum computer have been implemented on different hardware platforms, the scaling of those to large qubit numbers remains a challenge in all of them [11, 12].

In 2022, IBM released the "Osprey" quantum processor [13]. Boasting 433 superconducting qubits, it holds the record for the most qubits in a quantum computer as of that date. However, this count remains far from the required number of qubits needed to construct a truly useful quantum computer. While state-of-the-art methodologies for constructing and maintaining such systems are effective for this relatively modest qubit count, a significant increase in the number of qubits entails addressing the extensive tuning effort demanded by current devices. Furthermore, a pressing challenge arises from the limitation of conventional dilution refrigerators, which are ill-equipped to handle thousands or even millions of control lines. The potential for a dense arrangement of numerous spin qubits within a confined space further exacerbates the intricacy of the wiring scheme [14, 15]. This

issue, known as the fan-out problem, represents another significant bottleneck in quantum computing [16].

Spin qubits serve a pivotal role in this context. Solid-state qubits, utilizing electron spin as an inherent implementation of a two-level system, were initially proposed by Daniel Loss and David DiVincenzo in 1998 [17]. The electrons are postulated to be confined within quantum dots, a discovery that was recently honored with the Nobel Prize in Chemistry in 2023. Even though the work of Bawendi, Brus and Ekimov is completely different to the sense in which we use quantum dots, the Nobel Committee explicitly honors the fact that this work was conducive to quantum dots in semiconductor structures as we use them [18]. Essential foundational components requisite for the operation of a silicon spin-qubit based quantum computer have been successfully demonstrated, including high single- and two-qubit gate fidelities[19–25], alongside new readout strategies[26, 27] as well as robust readout fidelities[28, 29].

To date, devices accommodating up to six individually controllable, physical spin qubits have been realized [30]. Moreover, several proposals for spin-qubit-based architectures have emerged [14, 15, 31, 32], promising both facile scalability and compatibility with industrial applications [16, 33, 34]. One important part of all the proposed architectures is a mid-range coherent link between qubits or qubit registers, which will be the main issue for this thesis.

1.2 Outline

In this thesis, we describe one implementation of such a mid-range coherent link, which we call a *spin qubit shuttle* (SQS) device [35].

In chapter 2, we will further introduce some of the concepts previously mentioned. First, we will explain the theoretical foundation of single-electron-transistors, quantum dots and spin qubits. We will then describe recent advancements in silicon-based spin qubit systems as well as different architecture proposals to scale up such systems. Next, the exact layout and implementation of a SQS will be discussed. Lastly, we will briefly introduce the terminology and theory of valley multiplicity in silicon and describe the problems it causes for the operation of qubits.

In the next part of the thesis, chapter 3, we describe the process of finding a sample suitable to perform shuttling experiments with. For this, we did a mass-characterization of in-house fabricated devices at a temperature of about 4 K. We will explain the experimental setup and the whole measurement workflow. Also, exemplary data to each measurement and analyse metrics and performance of different heterostructures will be shown.

After having found a suitable device, one can cool this down to millikelvin temperatures to perform shuttling experiments. Chapter 4 addresses charge shuttling experiments, a type of experiment investigating the movement of electron charge without consideration of the spin state. As an introduction to shuttling, we will explain the experimental setup, the pulse sequence and we will show how to optimize pulse parameters for these types of experiments.

The main part of the thesis, the measurements of spin-coherence while shuttling, will be presented in chapter 5. We will mention the differences in initialization and readout compared to charge shuttling experiments, introduce our measurement scheme and describe how to extract the decoherence time T_2^* and how to theoretically describe its correlation to the shuttled distance.

The last part of this thesis, chapter 6, will be on the measurement and mapping of valley splitting. As an important parameter for the performance of a SQS, the results of these measurements will hint on how to proceed to make the SQS work.

Finally, chapter 7 will give a conclusion on everything that was done as well as a short outlook on the future of this research.

Chapter 2

The Spin Qubit Shuttle device

This chapter will introduce the background knowledge necessary to understand the experiments presented in this thesis. For this, we will explain the theory behind spin qubits and valley splitting as well as introducing the device design and proposed architecture.

2.1 Theoretical background of spin qubits

First, we will discuss some basic properties of qubits. After this, we list different approaches on how to realize a qubit with an electron spin system. Lastly, we discuss properties of basic concepts used in the remainder of the thesis, such as single-electron transistors and (double) quantum dots.

2.1.1 Qubits and decoherence

As already mentioned in the introduction, a qubit is the basic unit of information in a quantum computer. Similar to a classical bit having 0 or 1 as possible values, the state of a qubit can be any superposition of a ground state $|0\rangle$ and an excited state $|1\rangle$ in a quantum mechanical two-level system. More specifically, we can write a general qubit state as

$$|\Psi\rangle = \alpha\,|0\rangle + \beta\,|1\rangle\,, \tag{2.1.1}$$

with $\alpha, \beta \in \mathbb{C}$ and $|\alpha|^2 + |\beta|^2 = 1$. This state can be depicted as a state vector on the so-called *Bloch sphere*, as shown in figure 2.1a. The probability amplitudes of the qubit state relate to the position of this state vector by

$$\alpha = \cos\left(\frac{\theta}{2}\right) \quad \text{and} \quad \beta = e^{i\varphi}\sin\left(\frac{\theta}{2}\right), \tag{2.1.2}$$

with $\theta, \varphi \in [0, 2\pi]$. Here, one degree of freedom was omitted by dropping a global phase factor $e^{i\delta}$ as it has no influence on physical observables. The Bloch sphere representation not only makes it easy to visualize qubit operations but also decoherence mechanisms, which will be exceedingly important for the remainder of the thesis. We differentiate between two different types of decoherence, *relaxation* (fig. 2.1b) and *pure dephasing* (fig.

2.1c), described by a relaxation time T_1 and a dephasing time T_2^*, correspondingly. For spin qubits implemented in Si/SiGe, T_1 times of several seconds as well as T_2^* times of $\mathcal{O}(10\,\mu s)$ have been achieved. Even though the physical realization of our system is not fully comparable to these values, the underlying physical principles are the same and the Bloch sphere visualisation of the decoherence processes still holds.

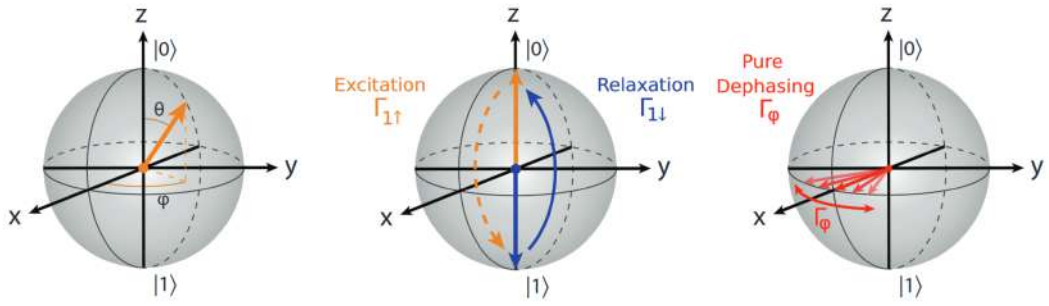

(a) **(b)** **(c)**

Figure 2.1: Bloch sphere representation of qubits and decoherence mechanisms. (a) Bloch sphere representation of a qubit and a state vector. (b) Relaxation and excitation depicted on a Bloch sphere. (c) Pure dephasing depicted on a Bloch sphere. The different decoherence mechanisms are denoted as $\Gamma_{1\downarrow} = 1/T_1$ and $\Gamma_\varphi = 1/T_2^*$. Figures adapted from [36].

2.1.2 Implementing qubits with electron spins

Any quantum mechanical two-level system can be realized as our qubit. In comparison to superconducting qubits, where the anharmonicity of the qubit and the presence of higher states plays an important role in the operation of the qubit [36], spin qubits seem to be the perfect contender to avoid these problems. When we use a spin-1/2 particle, the spin can be either $|\uparrow\rangle$ or $|\downarrow\rangle$. This is a natural realization of a qubit without any higher states we have to take into account. This allows us to use the spin of a single electron as a qubit. We call these kinds of qubits *Loss-DiVincenzo* (LD) qubits, since they were first proposed by Daniel Loss and David P. DiVincenzo in 1998 [17]. Such a qubit can be described by the Hamiltonian

$$H(t) = \frac{1}{4}\sum_{\langle i,j\rangle} J_{ij}(t)\sigma_i \cdot \sigma_j + \frac{1}{2}\sum_i g_i \mu_B B_i \cdot \sigma_i, \tag{2.1.3}$$

which assumes tight electron confinement. Here, J_{ij} is the exchange coupling, σ_i, $i \in x, y, z$ are the Pauli operators, μ_B is the Bohr magneton, B_i is the effective magnetic field and g_i the g-factor, each at site i. Besides using a single spin as a qubit, since we only require a two-level system, there is another possibility of implementing a qubit with spins. We can use two electrons and thus two spins to implement our qubit instead. For this, we use the singlet state $|S\rangle = \frac{1}{\sqrt{2}}(|\uparrow\downarrow\rangle - |\downarrow\uparrow\rangle)$ and the triplet state $|T_0\rangle = \frac{1}{\sqrt{2}}(|\uparrow\downarrow\rangle + |\downarrow\uparrow\rangle)$ as our

two-level system. This type of qubit can be described by the Hamiltonian

$$H_{ST_0} = J_{12}\frac{\sigma_z}{2} + \mu_B \Delta(gB^z)\frac{\sigma_x}{2}, \tag{2.1.4}$$

with $\Delta(gB^z)$ being the magnetic field gradient of the two electrons in a global magnetic field in z-direction. Even though this realization of a qubit might intuitively seem to be more complicated than just using a single spin, it has the advantage to not be dependent on oscillating fields, which can be hard to control in nanoscale devices [37]. For the experiments probing the coherence of the shuttling process, we will use *Einstein-Podolsky-Rosen* (EPR) spin-pairs. In its most general form, an EPR pair is a pair of two qubits that are in a maximally entangled state [38]. As the physics of such an EPR pair can be described as analogous to the physics of a ST_0-qubit, it is evident why it is useful to know the behaviour of an EPR pair as well.

2.1.3 Quantum dots and single electron transistors

To control and operate our qubits, we need to be able to confine and isolate electrons. This is done by trapping them in a *quantum dot* (QD), which can be seen as a small semiconductor "box" containing an integer number of electrons. Electrons are confined vertically by the given heterostructure as well as laterally by the metallic gates on top of the device. That way, all sides impose repelling electric fields on our electrons, allowing us to trap and control them.

Quantum dots are an important building block of a *single electron transistor* (SET) which our devices use both as an electron reservoir and a charge sensor. Usually, a SET consists of a quantum dot, also called an *island*, which is connected to a source and drain through tunnel junctions. This island is connected to a third electrode, the *gate*, which is capacitively coupled to the island and allows for control of its electrochemical potential. The SET makes use of the *Coulomb blockade* effect, which states that applying a positive voltage to the gate lifts the blockade, and electrons can tunnel through the SET.

2.1.4 Double quantum dots and charge stability diagrams

The layout of our devices now allows for multiple quantum dots next to each other. To initialize an EPR pair or a ST_0-qubit in our device, we already need two neighboring quantum dots. Such a system is called *double quantum dot* (DQD) [39–41]. We further assume the chemical potentials of the two QDs to be independently controllable by the gate voltages V_{G1} and V_{G2}, respectively. Each dot can be occupied by an integer number of electrons. We denote these occupation numbers in the DQD as (n_1, n_2), with $n_i \in \mathbb{N}_0$ and $i \in 1, 2$. By changing the gate voltages $V_{G,i}$, we can change the occupation of each

quantum dot. Assuming that the dots are capacitively coupled, adding an electron to one of the dots changes the electrostatic energy of the other dot. An important concept to map the occupation of the quantum dots at certain gate voltages and to quantify coupling strength is the so-called *charge stability diagram* (CSD). Figure 2.2 shows a sketch of a charge stability diagram for both an uncoupled DQD, as well as for a more realistic, coupled double quantum dot. To conclude this section on theoretical concepts, it is worth

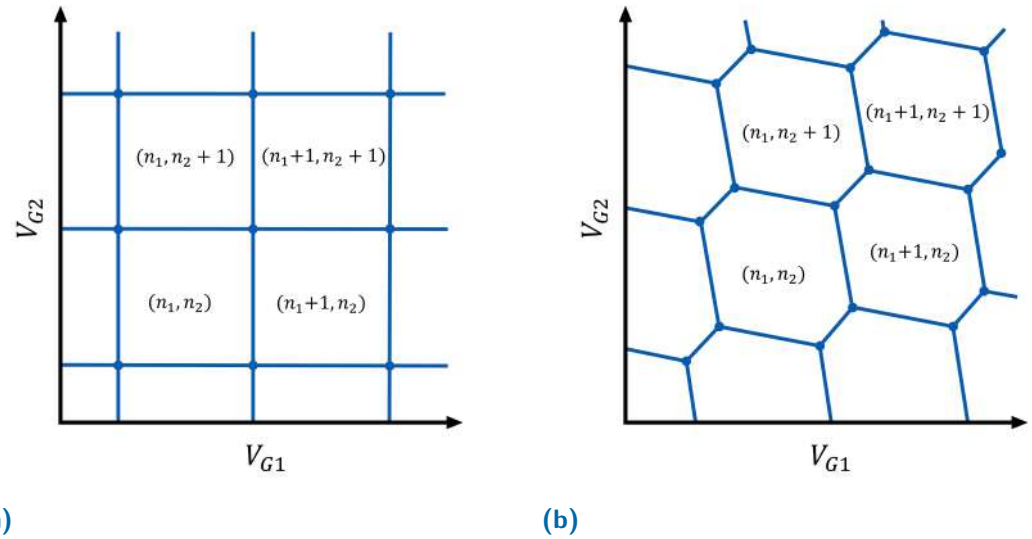

Figure 2.2: Charge stability diagram of a double quantum dot. (a) Two uncoupled dots. (b) Two capacitively coupled dots with gate crosstalk.

noting that the description of the DQD and the form of the CSD can be explained purely from a classical perspective and does not require any quantum mechanical concepts. This is because the above description of a DQD, as well as the charge stability diagrams, completely neglect the spin of the electrons. We will come back to how to modify the theory correspondingly in chapter 5.1.

2.2 Recent advancements in silicon spin qubits

This chapter offers a concise yet comprehensive overview of recent advancements, showcasing the state-of-the-art in silicon-based spin qubit systems. As highlighted in the introduction, this type of qubit is notable for its exceptional single- and two-qubit gate fidelities [19–25, 42, 43], which surpass the threshold required for topological error correction [21]. The confinement of electrons in Si/SiGe heterostructures is particularly promising [16, 44–46] due to their prolonged coherence times [47–49] and compatibility with silicon-based industrial fabrication methods [16, 33, 34, 50, 51].

To realize practical quantum computers and networks, qubits must be effectively coupled. Techniques exist to bridge distances up to millimeters by transferring the spin state to a photon within a cavity [52–56]. However, these methods, due to the spatial extension of cavities, are unsuitable for coupling electrons at the micron scale. As a solution, the transfer of electrons between two quantum dots emerges as the favored approach. While transfers have been achieved using surface acoustic waves [57–60], they introduce issues such as uncontrolled orbital excitations from the globally generated shuttling waves. These problems are absent when using quantum dots governed by a metallic gate array [61–64]. Initial techniques in these systems shifted electrons by individually controlling the tunnel barrier of each interdot transition, a method termed bucket-brigade mode shuttling. This technique has recently enabled shuttling through an array of four quantum dots [65].

However, simply scaling up these systems does not address the fan-out problem [35]. This challenge is addressed by conveyor-mode shuttling. Unlike the bucket-brigade method, conveyor-mode requires only a consistent number of input lines to move an electron across nearly any distance [35, 66]. The research detailed in this thesis picks up where conveyor-mode shuttling was recently proven as a viable concept [66], and where the theoretical underpinnings of single-electron shuttling have been established [35]. Within the past year, spin-coherent shuttling in longer devices at increased speeds has been demonstrated [67, 68]. Additionally, slow charge shuttling over a length of 10 µm has been realized, serving as a crucial proof-of-concept given its requisite length for scalable architecture [69]. A significant challenge in operating these shuttle devices arises from valley splitting [70]. Recognizing that these devices can also be employed to map and identify [68] valley splitting, the onus is now on material science to develop better heterostructures with enhanced valley splitting.

Nevertheless, achieving effective coupling is merely the initial step in scaling up spin qubit systems into full-fledged quantum computers, which also necessitates additional qubits. The highest number of individually controllable silicon spin qubits produced in an academic setting to date is six [30]. On a commercial front, Intel recently unveiled "Tunnel Falls", a twelve-qubit processor slated for release to research institutions [71]. While systems with even larger qubit counts have been developed [72], they lack individual controllability, imposing further constraints on potential algorithms.

2.3 Architecture proposals for scalable quantum computing

The previous chapter listed numerous experiments that show that we are able to define and initialize qubits and perform single- and two-qubit gates. But building a large-scale fault-tolerant quantum computer requires millions of qubits. Thus, we need a *scalable* architecture, in which the addition of physical resources must significantly raise the per-

formance of the quantum computer while the influence of negative effects is not raised accordingly [73]. For spin qubits in Si/SiGe, we expect better scalability compared to other hardware platforms, as we can make use of the silicon industry infrastructure and foundries. Approaches to scale up a semiconductor-based architecture using spin qubits can mainly be divided into two classes, sparse-grid and dense-array architectures. An example for a dense array architecture, the crossbar network [74], is shown in figure 2.3a. While such an approach needs only limited control resources, it has some evident drawbacks such as a higher demand on qubit homogeneity and larger cross-talk between qubits. On the other hand, examples for a sparse-grid architecture are depicted in figures 2.3b and 2.4a [16, 69]. The SQS device studied in this thesis can serve as a mid-range coherent

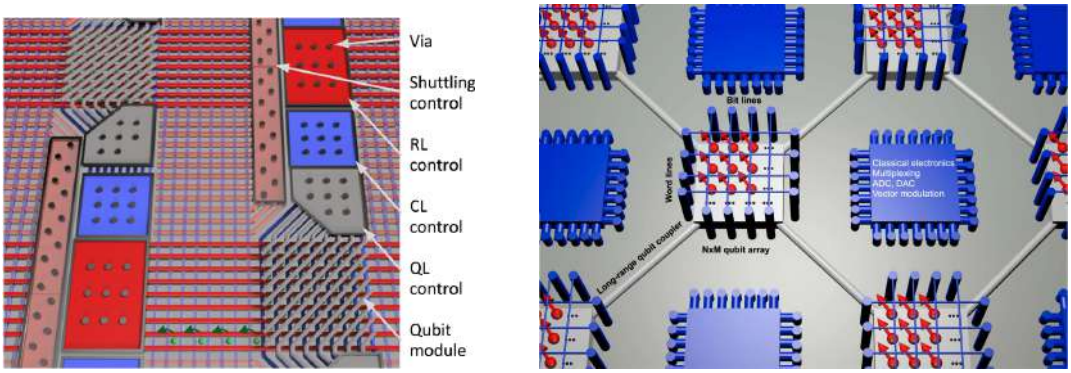

Figure 2.3: Architecture proposals for scaling up spin qubit systems. (a) Crossbar network architecture. Figure taken from [74]. (b) Sparse-grid architecture. Figure taken from [16]

qubit link for several architecture proposals, mostly sparse-array architectures. Nevertheless, it is tailored for the *SpinBus* architecture [69], shown in figure 2.4. This architecture proposal would include a large number of the unit cells shown in 2.4b. They consist of multiple SQS as shuttling lanes, as well as T-junctions to ensure scalability in two dimensions, manipulation zones to perform single- and two-qubit gates, and dedicated zones for initialization and readout of qubits. This proposal offers the benefit of requiring only a minimal number of input lines. Additionally, different cells can share the same input lines, enhancing its scalability relative to alternative methods. Also, the large spatial distance between qubits practically excludes unwanted crosstalk effects. Regardless of the exact implementation, the SQS should be able to operate on length scales about $\mathcal{O}(10\,\mu\text{m})$.

2.4 Device layout

Next, we further describe the design and layout of the device used in the thesis. Since devices of similar layout will be used in all parts of the thesis, the design choices and device properties stated here apply to everything in the remainder of this thesis, unless stated otherwise. As mentioned before, we will call the device SQS, short for spin qubit shuttle.

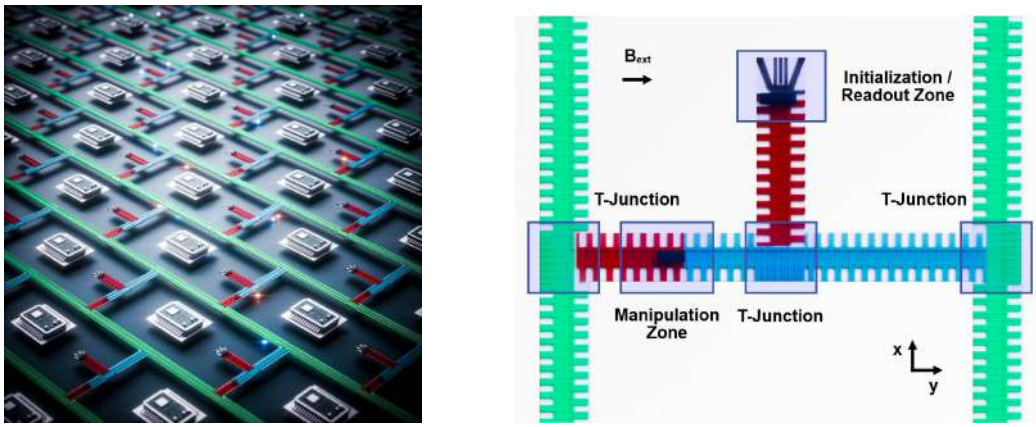

(a) (b)

Figure 2.4: SpinBus architecture for scalable spin qubit systems. (a) Envisioned architecture for a quantum computer that contains several unit cells as well as cryoelectronics for qubit control. Figure adapted from [69]. (b) Unit cell of the SpinBus architecture showing shuttling lanes, T-junctions and dedicated zones for initialization, manipulation and readout. Figure taken from [69].

It is worth mentioning that in other references it might be also referred to as quantum bus or QuBus, SQuS and squsi [75, 76].

2.4.1 Device stack and Si/SiGe heterostructure

To use electrons as spin-qubits, we must isolate and confine them in all three spatial dimensions by trapping them in a *quantum dot* (QD). We vertically confine electrons by employing a heterostructure, in our case a Si/SiGe heterostructure, which is sketched in figure 2.5. We confine the electron and operate the qubit in the middle part of this material stack, the silicon *quantum well* (QW). This silicon layer lies between two layers of silicon-germanium, more specifically $Si_{0.7}Ge_{0.3}$. We refer to this three-layer-stack Si/SiGe heterostructure. On top of this material stack we find a thin silicon cap to prevent oxidation of $Si_{0.7}Ge_{0.3}$. We laterally confine our electrons by employing metallic gates made of Ti:Pt on top of the device. In order to isolate these gates both from each other and from the device, they are separated by an oxide layer, consisting of Al_2O_3.

2.4.2 Gate layout

The aforementioned gate layout of the Ti:Pt gates on top of the material stack defines the lateral confinement of electrons and therefore highly influences the potential in the QW and the functionality of the device. A sketch of the general gate layout is shown in figure 2.6. Since the middle part of an SQS is periodic, this structure can be fabricated in any desired length, but the same working principle remains. We show SEM pictures of two different examples of devices with a different length in figure 2.7. In the following, we

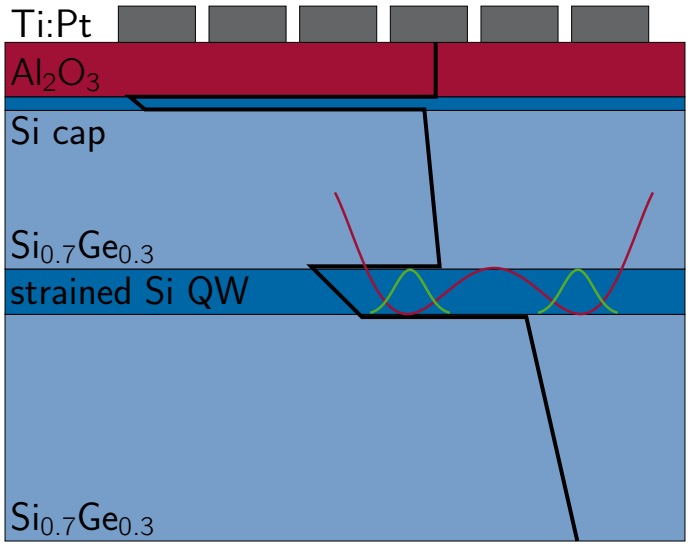

Figure 2.5: Sketch of the material stack used for the SQS devices, consisting of a Si/SiGe heterostructure, an oxide layer (Al_2O_3) and metallic gates. The black line shows the vertical potential landscape, the red line indicates the horizontal potential landscape once voltages are applied. The green line shows the probability distribution of electrons trapped in the red potential. Figure adapted from [77].

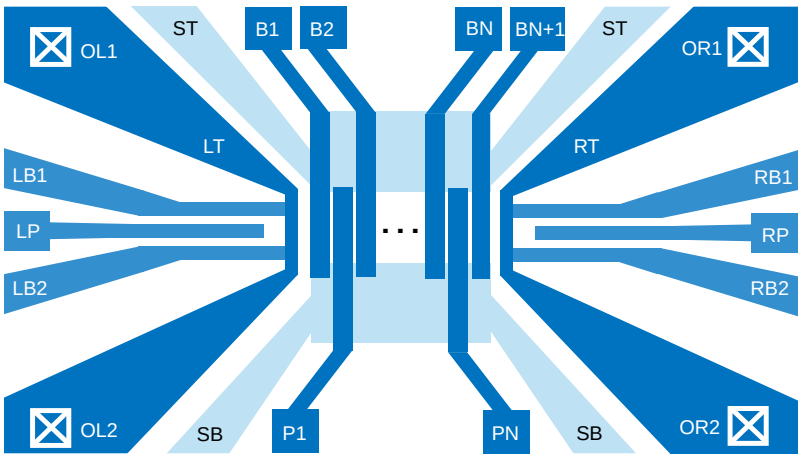

Figure 2.6: General gate layout of a SQS device. The dots in the middle indicate that the device is theoretically infinitely scalable to N plunger gates and N+1 barrier gates. Besides that, there is a top gate, a plunger gate and two barrier gates on each side to form an SET. Also, ohmic contacts are implanted on each side.

refer to the gate layout shown in figure 2.7a as 8-dot device, while the structure shown in figure 2.7b will be called long SQS. The gates shown in figure 2.6 are fabricated in three different layers. On the first layer, there are two so-called screening gates, labelled as ST (for top) and SB (for bottom). They confine the channel through which we want to shuttle the electrons. In this channel, we realise a sinusoidal potential, controlled by the clavier gates on top of the channel. The second gate layer hosts the plunger gates Pi. They define the depth of each quantum dot. Their counterpart, the barrier-gates Bi, are fabricated on the third layer. They determine the height of the tunnel barrier between the dots. These plunger and barrier gates are together referred to as clavier gates. On

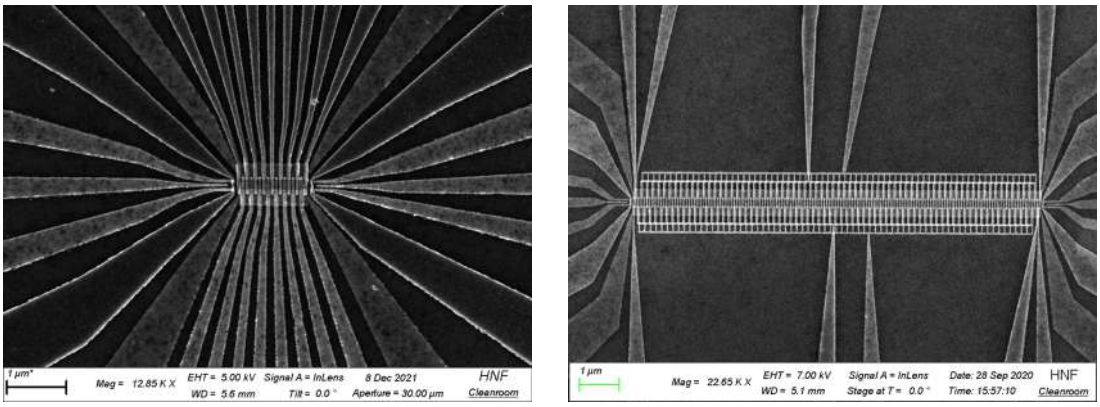

(a) **(b)**

Figure 2.7: SEM pictures of different device layouts. (a) Picture of an 8-dot SQS device with each gate being individually controllable. (b) Picture of a long SQS device. In contrast to (a), the four gate sets are already connected.

the left (L) and right (R) side of the channel, you see four gates that form an SET. Each SET consists of two barrier gates (XBi) and a plunger gate (XP), X $\in$ {L, R}, to form a quantum dot. These gates are also fabricated on the second layer. A top gate XT on the third layer serve as a guide for the current path. Further, two ohmic contacts, here called OXi, are implanted on each side of the device in the region of the top gate.

2.4.3 Potential in the SQS

With the SQS, we want to be able to trap an electron in a quantum dot and move this quantum dot together in space. For this, we connect each fourth clavier gate to the same voltage, thus defining four gate sets. These are depicted at the top of figure 2.8a. This configuration allows us to only use four input lines to theoretically generate arbitrarily many quantum dots throughout the channel. When we now want to move the electron and shuttle it through the channel, we have to apply a voltage

$$V_i = A_S \cos(\varphi(t) - \Delta\varphi_i), \tag{2.4.1}$$

with $\varphi(t) = 2\pi f t$,

$$\Delta\varphi_i = \frac{\pi}{2}(i-1) \tag{2.4.2}$$

to the four gate sets $i \in \{1, 2, 3, 4\}$. Here, t is the time and f the frequency of our signal. A sketch of this is shown in figure 2.8b. This pulse sequence will be further described in chapter 4.2.

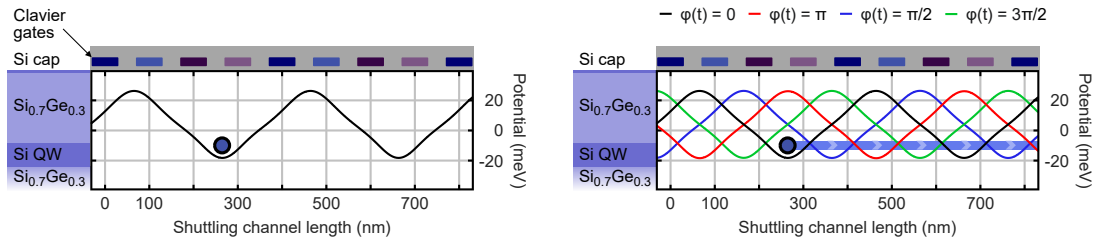

Figure 2.8: Sketch of the potentials in an SQS device. (a) Static potential with multiple quantum dots arising in the QW. Figure adapted from [69]. (b) Time-dependent potential for shuttling processes. The intended path of the electron is indicated in blue. Figure taken from [69].

2.5 Theoretical background of valley splitting

In perfect bulk silicon, the conduction band minimum is six-fold degenerate, as sketched in figure 2.9. The geometry of our heterostructure causes this degeneracy to be lifted. The lattice constants of silicon and germanium differ [78], leading to strain when they are integrated into a heterostructure. Importantly, this strain remains stable only within specific boundaries [79]. Beyond a certain germanium concentration or when the quantum well exceeds a particular thickness, the strain starts to relax, resulting in the formation of dislocations. This strain splits the degeneracy into two subbands, an upper, four-fold degenerate Δ-band, and a lower, two-fold degenerate Γ-band. The energy difference of these two bands is about 200 meV and therefore does not further concern us. However, the remaining degeneracies are also lifted because of the spatial confinement caused by the heterostructure. More precisely, the spatial confinement leads to an overlap of Bloch waves with the SiGe potential barrier. The Γ-subband splits into two energy levels with an energy difference on the order of 100 µeV, where the exact value can vary depending on the germanium content and ordering. We call this energy difference *valley splitting*, and the two states upper and lower valley. We denote the valleys as $|+\rangle$ and $|-\rangle$, respectively. With this notation, we can express the state of the electron as the tensor product of a spin state and a valley state, e.g. $|\uparrow,+\rangle \equiv |\uparrow\rangle \otimes |+\rangle$. The level structure of the silicon ground state under consideration of the mentioned geometric restrictions is sketched in figure 2.10. In our heterostructure, the emergence of two distinct states allows us to create an addressable qubit. Nonetheless, a small valley splitting can lead to complications. A larger valley splitting is thus preferable for the efficient operation of spin qubits, making it a primary challenge in Si/SiGe systems. The problems arising due to a small valley splitting can be mainly divided into two classes. Firstly, there can be excitations from the lower to the upper valley. These can occur as Landau-Zener transitions while shuttling. The valleys usually have a small g-factor difference, which causes a random, uncontrollable phase being picked up while the electron is in the upper valley. Here, the randomness

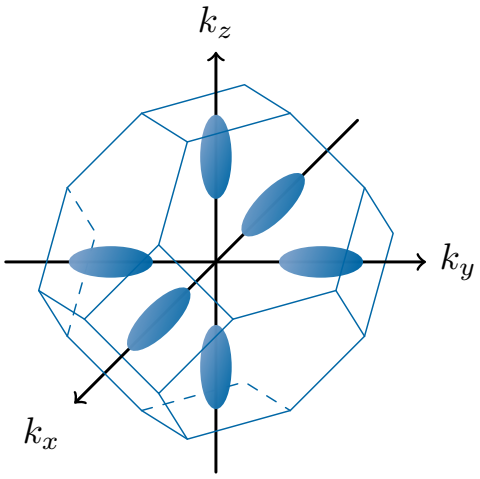

Figure 2.9: Sixfold degeneracy of the ground state in bulk silicon. The ground state is depicted as blue ellipsoids in a silicon Wigner-Seitz cell in the reciprocal space.

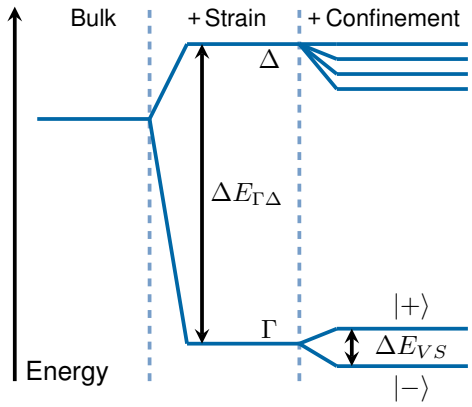

Figure 2.10: Energy levels of strained and confined silicon. The sixfold degenerate ground state of bulk silicon is sketched. Under strain, this ground state splits up into a Δ-band and a Γ-band. The latter again splits up under confinement, defining two valley states and valley splitting as their energy difference. Figure adapted from [76].

arises from the non-deterministic behavior of the Landau-Zener transitions. Also, it is not directly possible to influence or control when transitions to the upper valley happen. It is practically impossible to correct for this random phase, thus leading to information loss [35]. Secondly, a small valley splitting allows for spin-flips from the $|\uparrow\rangle$-state to the $|\downarrow\rangle$-state. As the valley splitting is fundamentally caused by the overlap of the wave function in the QW with the SiGe layer serving as a potential barrier, small atomic steps in the interface and atomic-scale crystal variations are believed to cause so-called valley splitting hotspots, at which the valley splitting is exceptionally small and therefore a huge problem in the operation of the SQS device [37, 76]. Due to that, mapping the valley splitting, finding valley splitting hotspots and trying to circumvent them, is an important goal that is to be discussed further in chapter 6.

Chapter 3

Mass-characterization of in-house fabricated devices

In this chapter, we will describe the mass-characterization of in-house fabricated devices. The goals of these measurements are to compare different heterostructures and find out which yields the best results as well as finding a sample that is suitable for further measurements at millikelvin temperatures. The work presented here was an equal collaboration Arnau Sala and myself. Additionally, some of the measurements were performed by Denny Dütz and Sammy Umezawa. The measurement workflow used here is adapted and modified from the workflows developed by Niels Focke [80] and Max Beer [81].

3.1 Experimental setup for measurements at 4 K

As the samples must be cooled down to millikelvin temperatures to ensure a stable quantum behaviour, even the pre-characterization to test basic functionalities must be performed at low temperatures. For this, we mount a PCB with the sample connected to it to a dipstick that we dipped in a dewar filled with liquid helium and thus cooling it down to a temperature of approximately 4 K. The dipstick itself is made of stainless steel. Before each measurement, it is evacuated to remove the influence of gases that condense inside the dipstick as well as moisture. Thereafter it is refilled with a bit of helium that serves thermal exchange gas. From inside the dipstick, 23 DC connections lead up to a breakout box that breaks out the wiring and allows for connecting other measurement equipment with BNC connectors. This breakout box is connected to the wiring inside the dipstick via a hermetic Fischer connector. Linked to the breakout box, we connect two Stanford SR830 Lock-in amplifiers (LIAs) [82], two Keithley 2400 Source Measure Units (SMUs) [83] and one in-house built voltage source inspired by the Harvard DecaDAC. The LIAs each come with a voltage divider at their output, that reduces the voltage by a factor of 10^{-4}. We connect the LIA to the ohmic contacts of the sample, which we use to perform the transport measurements. The SMUs are connected to the top gate and thus serve to measure the leakage current to the top gate while supplying a voltage to it at the same time. The remaining lines are connected to the DecaDAC. All of these instruments are connected to a measurement computer that comes with an Adlink USB/LPCI/LPCIe-3488A

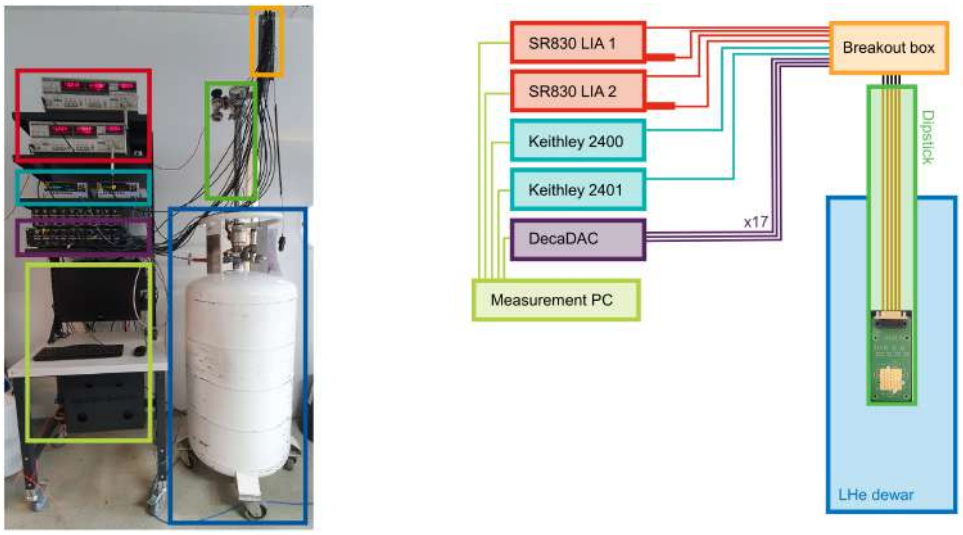

(a) (b)

Figure 3.1: Experimental setup for measurements at 4 K. (a) Picture of the setup with important parts indicated by colored frames. (b) Sketch of the setup and wiring scheme. Colors correspond to the colored frames in (a).

IEEE488 GPIB card [84]. The full periphery of this setup including all of the instruments listed above as well as the dipstick inside of the dewar and the measurement computer is shown in figure 3.1a and sketched in figure 3.1b. Inside the dipstick, at its bottom, we have the sample to be cooled down. The sample is connected to the DC lines inside the dipstick through a stack of two other parts. The sample sits on an interposer, which itself sits on a DC printed circuit board (PCB). The PCB is then mounted on a brass holder inside the dipstick for thermal exchange and connected to the lines in the dipstick with a 25-pin D-Sub connector. These three layers needed to connect a sample to the dipstick, being the sample itself, the interposer, and the PCB, are depicted in figure 3.2. When practically setting up the experiment and starting a cooldown, first, a sample that is to

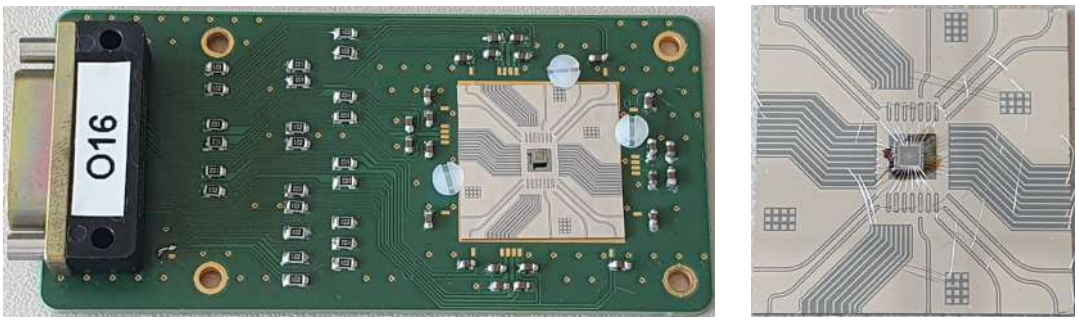

(a) (b)

Figure 3.2: Connection layers that connect the sample to the wiring and the dipstick. (a) PCB that is attached to the dipstick. An interposer is mounted to the PCB and attached by nylon screws. The lines on the interposer are bonded to the golden bond pads at its sides. (b) interposer with a sample glued to it. The sample is bonded from bond pads on it to lines on the interposer.

be tested must be chosen from a batch of samples. These batches are fabricated in the cleanroom at the Helmholtz Nano Facility (HNF) [85]. This is done by pre-screening with an optical microscope, as described in section 3.2. Next, the samples must be glued to an interposer. This is a silicon chip that allows for flexible usage of different sample designs on the same PCB. Furthermore, they have a high resistance at cryogenic temperatures, which additionally helps to protect a sample from noise. In addition to that, they are equipped with metallized routes to conduct signals from PCB to the sample. A wafer of interposers as we get it from fabrication is shown in figure 3.3a, a close up view can be seen in 3.3b. Each interposer is 20 mm × 20 mm in size. The interposers must be cleaned before they are ready to use. For this, we first detach the interposers from the plastic foil. Then, we put all interposers for 5 min in a bowl filled with acetone, which we in turn put in an ultrasonic bath. After this, we put it for another 5 min in isopropanol. Once the interposer is cleaned, we can glue the sample to the center of the interposer using GE varnish as it can still be operated at cryogenic temperatures [86]. In the next step, we establish an electrical connection between all three parts by bonding the sample to the interposer as well as bonding the interposer to the PCB. This is done with a West-Bond Luxuray 2 bonder equipped with an Olympus SZ51 microscope and bond wired made of aluminum. Two pictures of the bonded device can be seen in figure 3.4.

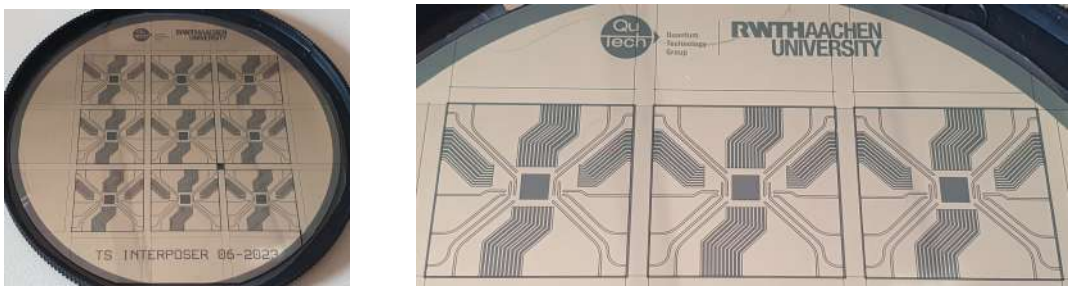

(a) (b)

Figure 3.3: (a) Wafer with interposers after fabrication and dicing. (b) Close up of the wafer in fig. 3.3a.

During the course of this characterization measurements, we used three different versions of the interposer with a different layout each. The different designs, as `GDS` files opened in *KLayout* [87], are shown in figure 3.5. After we started measurements with the first version (fig. 3.5a), we soon realized the need for more high-frequency lines as well as a possibility to easily connect multiple gates to a gate set. These problems were fixed with the second version (fig. 3.5b) and further improved to ensure easier and more flexible bonding in a third and final version (3.5c). The flexibility is important here as the sample, depending on its behavior at low temperatures, can either be used for shuttling experiments (cf. chapter 5) or for magnetospectroscopy measurements (cf. section 6.1), where both types of experiments have slightly different requirements to bonding.

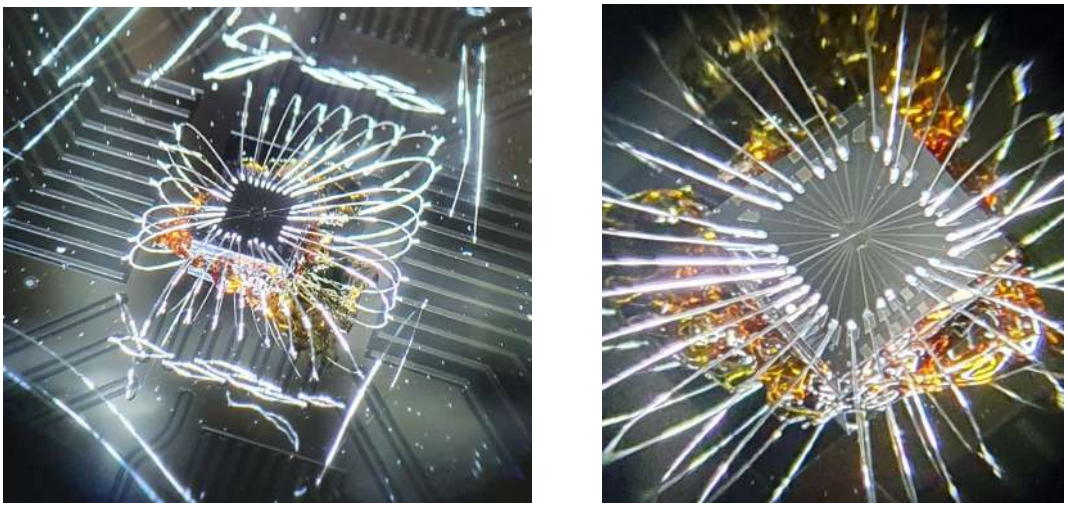

(a) (b)

Figure 3.4: (a) Picture of a bonded sample. (b) Close-up view of a bonded sample.

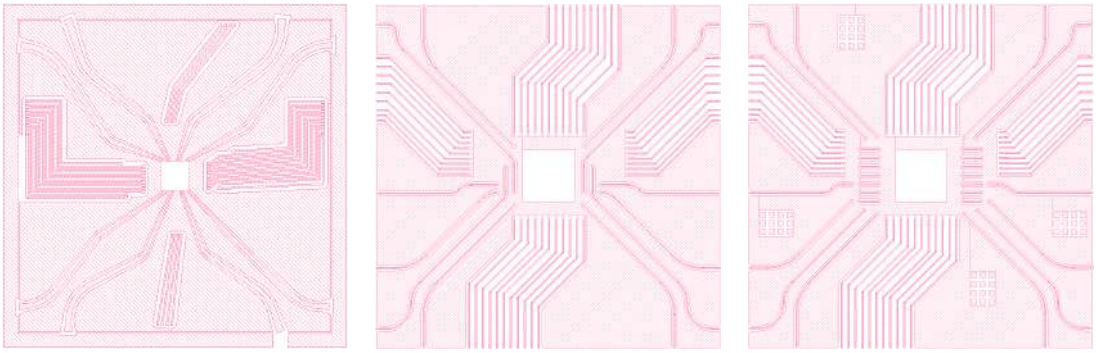

(a) (b) (c)

Figure 3.5: Different interposer design files used for our measurements, opened in KLayout. (a) First version of the interposer which we started our measurements with. (b) Version 2, improved by more high-frequency lines and a different course of these close to the sample, making it easier to connect multiple gates to one line. (c) Version 3, a final version of the interposer, again improved by additional bonding islands on the chip and by splitting up the aforementioned lines to enable easy connection of different gates while still bonding to different distances from the sample.

3.2 Optical microscope for pre-characterization

The first step of the workflow, that comes before any transport measurements is the optical investigation of the sample. This is done by looking at it with a Leica DFC850 optical microscope at 5x magnification. While this is certainly not suitable for resolving the SQS structure as depicted on 2.7a, it definitely allows to see some larger errors in fabrication or results of careless handling. Some examples of this are shown in figure 3.6.

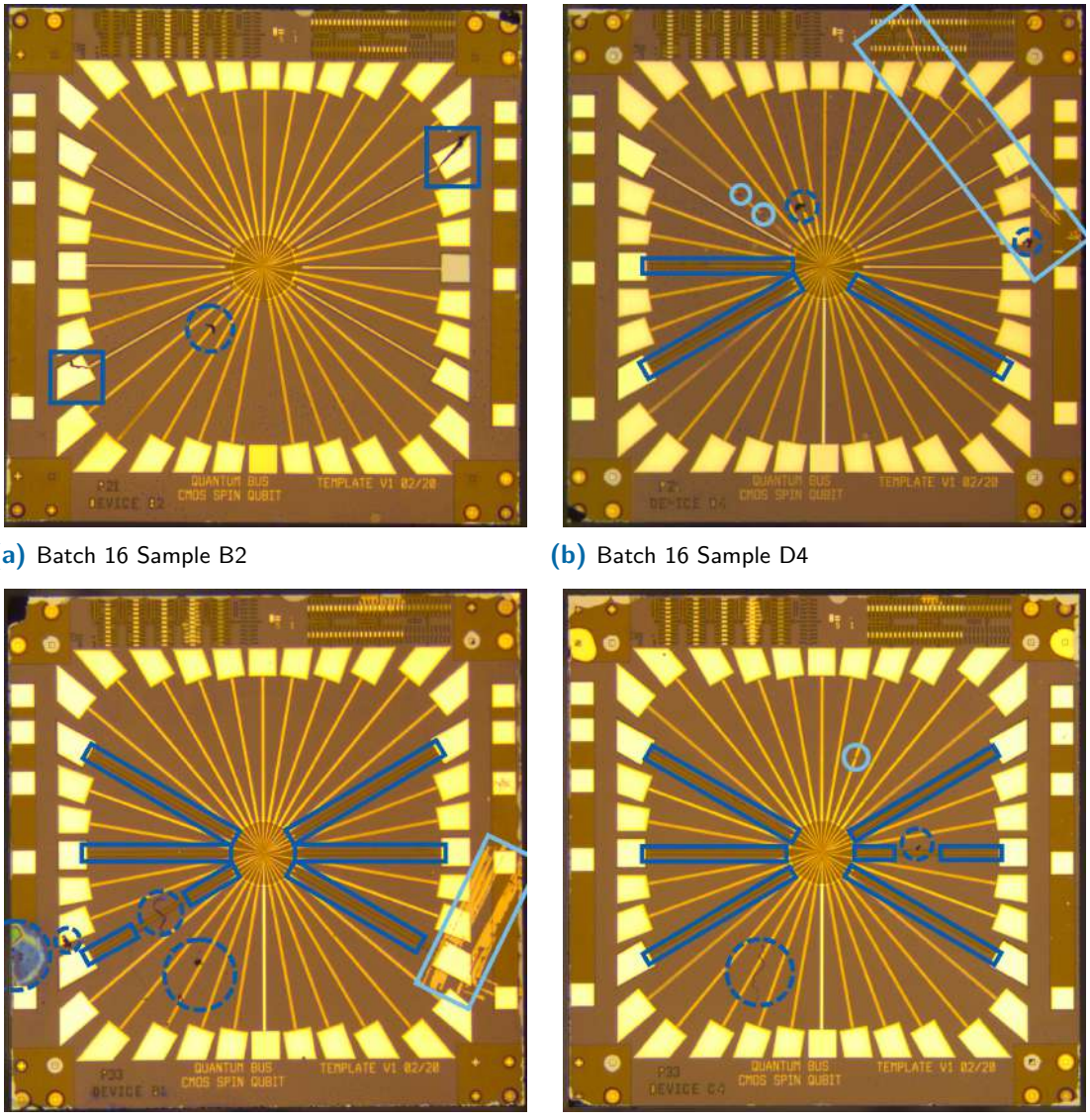

(a) Batch 16 Sample B2

(b) Batch 16 Sample D4

(c) Batch 16 Sample B1

(d) Batch 16 Sample C4

Figure 3.6: Samples under the microscope for optical pre-screening. Dark blue boxes indicate peeled off gates or bond pads, dark blue circles show dust and other residues on the samples. Light blue boxes show large-scale scratches, light blue circles mark gates broken only at one position. All samples shown here are taken from Batch 16. Pictures are taken with a Leica DM2700M camera integrated in the microscope.

The samples shown here all come with a selection of typical fabrication faults that we observe in this optical screening. The solid, dark blue boxes indicate bond pads that are peeling off or ohmic contact lines that are missing. The dashed, light blue rectangles show large-scale scratches that can occur during dicing or careless handling of the samples. Since such scratches almost always also hit gates and destroy larger structures, we will not use these samples further. The light blue, solid circles show broken gates. While in this case, the fabricated structure is generally present and almost fully intact, it is broken in some small regions which prevents a current from flowing there. Lastly, the dark blue dashed circles mark dust and other unwanted residues either from fabrication or from transportation and sample handling. For some of the samples, it could also be of interest to check the sample under a *scanning electron microscope* (SEM) before cooling it down. Some examples of SEM pictures taken after the measurement are shown and further discussed in chapter 3.5. Typical failure modes in the gate structure are damaged gates or misalignments in the fabrication. Both cases cannot be seen by a conventional optical microscope but can be visualized by using an SEM.

3.3 Measurement workflow

Once the sample is selected and cooled down as explained in chapter 3.1, the actual measurements can start. We use a standardized workflow that consists of the following steps:

1. Accumulation of a current through the SET
2. Time stability measurement of the current through the SET
3. SET barrier-barrier pinch-off sweep
4. SET barrier-plunger pinch-off sweep
5. SET plunger 1D pinch-off sweep
6. Accumulation of a current through the channel without screening gates
7. Screening-gate aided accumulation of a current through the channel
8. Pinching off the current through the channel with individual clavier gates and gate sets

Usually, for a fully working device, these measurements would be executed in exactly that order to determine the functionality of all parts. More precisely, measurements 1 to 5 check the functionality of the SETs and are thus performed once for each side. Measurements 6 to 8 on the other hand check the functionality of the actual SQS structure. They require to some extent successful previous measurements. It is also worth noting that measurement

5 and measurement 7 are optional and often (but not necessarily) only performed after the previous measurement failed. In the following, we will examine the full workflow step by step. For this, we will first give a short explanation of the goal and measurement procedure for each step, including a sketch of which gates to sweep and which gates to keep at another, constant voltage. We then show one exemplary measurement to point out what results we would expect for a fully functional device. Also, we will give a table of the exact voltage ranges we apply to each of the gates, using the gate naming convention from chapter 2.4.2. Lastly, we will discuss several failure modes, possible reasons for failure, and give a guide on how to proceed in case of error.

3.3.1 Accumulation of a current through the SET

As first part of the pre-screening, we test if we can accumulate electrons in the QW. For this, we apply a positive voltage to all SET gates (XP, XB1, XB2) as well as to the top gate (XT). Here, X is to be replaced with the left side L or right side R, as mentioned in chapter 2.4.2. In addition to that, we apply a bias to the ohmic contacts (OX1 and OX2). This is sketched in figure 3.7. In case we can accumulate electrons in the QW, the bias applied to the ohmic contacts will lead to a transport current which proves the accumulation. The possibility to accumulate electrons in the QW is essential to operate spin qubits, as we require a *two-dimensional electron gas* (2DEG), which on the other hand can only be established if we can accumulate electrons in the QW. An example of

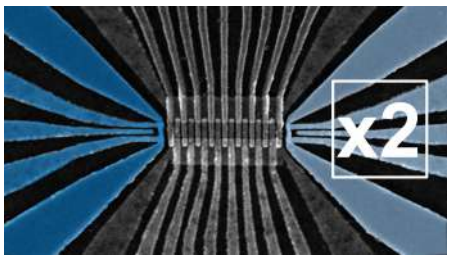

Figure 3.7: Gate layout of a SQS device with the gates to which we apply a voltage highlighted. Gates marked with the same color are always on the same voltage. The label "x2" on the right side indicates that the measurement is performed in exactly this way also for the other SET.

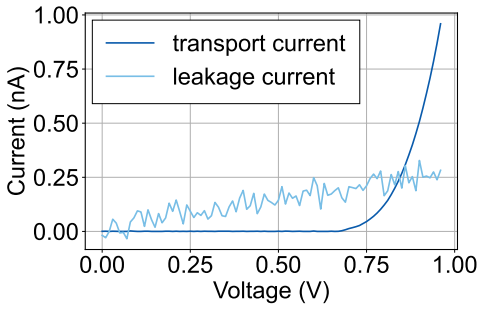

Figure 3.8: Measurement of accumulation of a current through the SET. The transport current is shown in dark blue, the leakage current in light blue.

how a successful measurement usually looks like is given in figure 3.8. Here, both the current measured by the LIA as well as the current measured by the SMU on one side of the device is plotted. The latter shows the current leaking through the top gate, which we

expect to reach values of up to 500 pA after applying some voltage. Due to the unwanted capacitances of charged gates, we expect a linear behaviour between voltage applied and leakage current measured. We record this value as an additional check of how well isolated the gates are from each other. Exceptionally high leakage currents will thus be treated as failure mode of this measurement, see below. For the transport current measured by the LIA, we expect not to see a current until a certain voltage is crossed. We define this value as pinch-off voltage V_{po}. After having crossed this threshold, we expect an exponential rise of current. We terminate the measurement once one of the two currents has reached the break condition, corresponding to a voltage of $V_{\mathrm{break}} = V(I_{\mathrm{SET}} = 1\,\mathrm{nA})$. This current is high enough to either verify that we can accumulate electrons in the QW as expected or classify a leakage current as too high and stop the measurement to prevent the device from being damaged. Experience of previous pre-screening experiments [81] suggest to sweep the voltage applied to all involved gates back to the point where the transport current reached about 200 pA. We define this point as operating point or *threshold voltage* V_{th}. Thus, we also define a measurement successful if we are able to reach this current. If the voltage has reached 1.5 V and the transport current is still below 200 pA, the measurement has failed. All of aforementioned values and applied voltage ranges are summed up in table 3.1. Notably, the LIAs should be set to different frequencies for both SETs. This is because significant cross-talk can occur in case two ohmic contacts from different SETs are bonded very close to each other on the interposer. This can result in a current being picked up by the wrong SET, that in case of two different frequencies will be filtered out. Next,

Table 3.1: Measurement parameters for an accumulation of a current through the SET.

Mode	Gate	Instrument	Voltage	Resolution	Break Condition
Variable	XT	SMU	0V - 1.5 V	10 mV	I(OX) > 1 nA or I(XT) > 1 nA
Variable	XB1 XP XB2	DecaDAC	0 V - 1.5 V	10 mV	I(OX) > 1 nA or I(XT) > 1 nA
Constant	OX1 OX2	LIA	100 µV		

we will discuss some failure modes that can occur during this measurement. Examples of measurements with each of the most commonly observed failure modes can be seen in figure 3.9. Figure 3.9a shows the most common failure mode, in which the SET shows no dependence on the voltage. This behaviour can be the result of a variety of effects, such as broken gates or electrostatic discharge. The next two examples, figs. 3.9b and 3.9c, show failure modes in which accumulation of a current is generally possible, but not satisfactory. In figure 3.9b, a current is accumulated, but saturates relatively early. This behaviour is typical for samples of the R2203 heterostructure, see chapter 3.5. It makes the sample inconvenient to use due to the small operation window and oftentimes does not even allow a current to reach the operating point. The example in figure 3.9c shows a fluctuating curve that is not monotonously rising. This can be an indication of instabilities in the

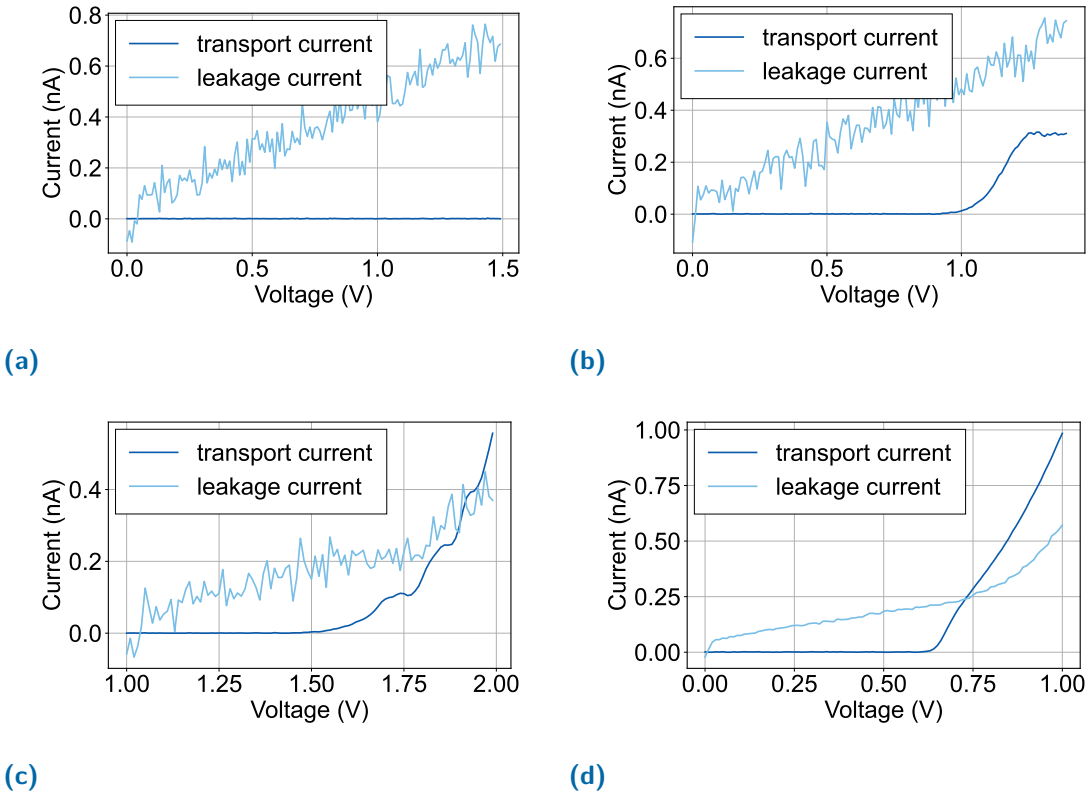

Figure 3.9: Failure modes for accumulating a current through the SET. (a) No current can be accumulated and no voltage dependence of the current is visible. (b) Low accumulation and early saturation of current. (c) Unusual noise, bumps and peaks in the transport current curve. (d) Diode-like behaviour of the leakage current.

ohmic contacts or the wiring, making this sample overall not reliable. The last failure mode shown here, figure 3.9d, shows a relatively normal looking transport current. However, the leakage current shows a diode-like behaviour instead of the usual linear dependence on the applied voltage. This could happen because of some impurities or imperfections in the material stack leading to shorts and thus a high, systematic leakage. In addition to these failure modes, a *charging* of the device can happen. This means that to many charge carriers are accumulated in a part of the device, influencing the transport current in a way that it becomes unstable and only occurs at increasingly higher pinch-off voltages. This failure mode can only be resolved by a thermal cycle, meaning the sample must be warmed up and cooled down again.

3.3.2 Time stability measurement of the current through the SET

Assuming the accumulation measurement was successful, we perform a time stability measurement next. For this, we keep all previously used gates at their operating point voltage V_{op}, as shown in figure 3.10. We again measure both leakage current to the top gate and transport current and observe their time stability over a time span of 80 s. Again, an exemplary, desirable result is shown in figure 3.11. The only possible failure mode here is that

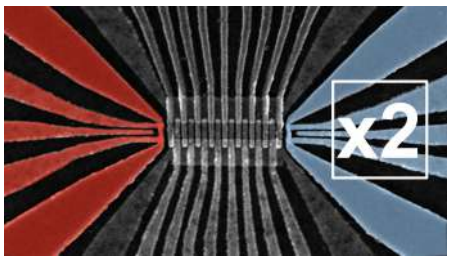

Figure 3.10: Gate scheme for time stability measurements of the current through the SET. The SET gates shown in red are all on the same voltage, being the operation point V_{op} from the previous measurement. The gates marked in light blue on the right side indicate that this measurement is repeated for both sides.

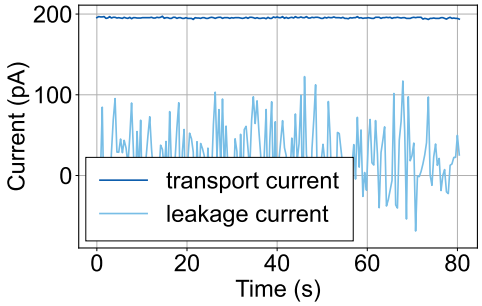

Figure 3.11: Results of a time stability measurement of the current through the SET. The transport current is shown in dark blue, the leakage current in light blue.

time stability is not given. It is quite subjective how different experimenters performing those measurements interpreted a good time stability. As a general definition that roughly matches this uncertainty, we define a sample as not stable in time if the transport current is below 150 pA (which means that it significantly fell of in between of the measurements) or if the current decreases by 2 % or more during the 80 s time span. An example for each of these cases can be seen in figure 3.12. However, it is worth mentioning that it can be possible to continue with the measurements and get satisfactory results for the following tests even if this condition is not fully met. Nevertheless, this measurement is important to learn about the behaviour of the sample and possibly explain unsatisfactory results in further experiments.

3.3.3 SET barrier-barrier pinch-off sweeps

Continuing the SET characterization, we now start to investigate not only the SET as a whole, but certain parts of it. To start off, we conduct a two-dimensional sweep of both barriers, XB1 and XB2, of each SET (fig. 3.13). This measurement will tell us about

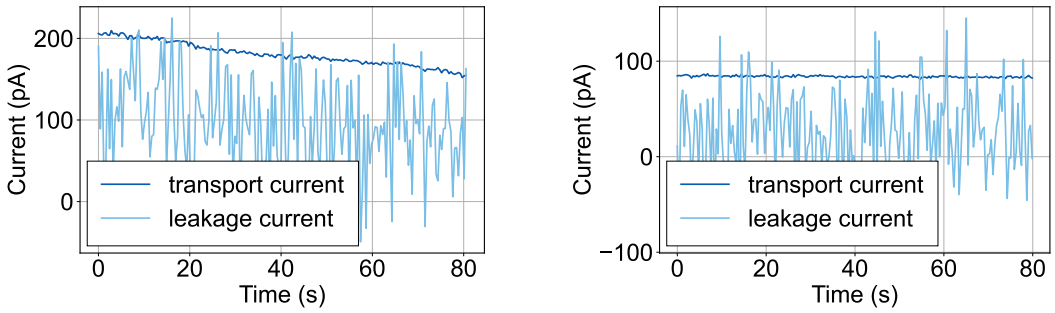

Figure 3.12: Failure modes of a time stability measurement in a SET. (a) Heavily decreasing current. (b) Constant current that started below 150 mV.

the interplay and cross-talk of these two gates. It is important to have two individually controllable barriers that do not influence each other strongly to form a proper quantum dot at lower temperatures. To ensure that this property is given, we investigate if the barriers are able to pinch-off the transport current independent from each other. Consequently, plotting this measurement as in figure 3.14, we expect a rectangular region, so-called *conductive region*, in the top right corner of the plot. This is as current should be able to flow only if both barriers are so positive that the current path is open. The

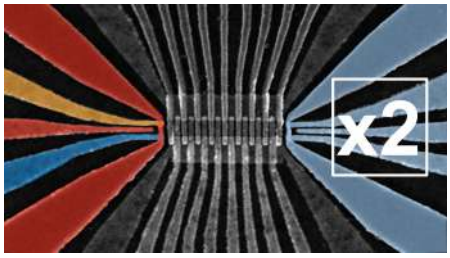

Figure 3.13: Gate scheme for SET barrier-barrier pinch-off sweeps. The gates on the operating point voltage V_{op} are indicated in red, the gates being swept in dark blue and yellow. All gates of the right SET are colored in light blue to indicate that this measurement is repeated for both sides.

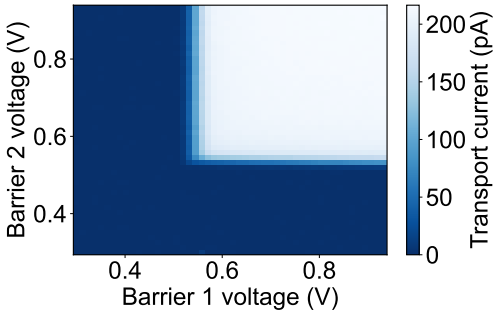

Figure 3.14: A successful SET barrier-barrier pinch-off sweep showing a well-defined conductive region in die upper right corner.

voltage ranges applied to the barrier gates and constant voltages at which we keep the other gates are summed up in table 3.2. Noticeably, for our standard resolution of 20×20 data points, this measurement takes significantly longer than the 80 s long time stability measurement before. This means, even though we assume the currents to be stable in

Table 3.2: Measurement parameters for an SET barrier-barrier pinch-off sweep.

Mode	Gate	Instrument	Voltage	Steps	Break Condition
Variable	XB1	DecaDAC	0V - V_{op}	20	I(OX) $>$ 1 nA
Variable	XB2	DecaDAC	0V - V_{op}	20	I(OX) $>$ 1 nA
Constant	XP	DecaDAC	V_{op}		
Constant	XT	SMU	V_{op}		
Constant	OX1 OX2	LIA	100 µV		

time at this point, we should take into account the possibility that failed measurements went wrong due to a slowly decaying current and not due to non-functional barrier gates. Having this in mind, we classify the four measurement outcomes depicted in figure 3.15 as possible failure modes. In this measurement, figure 3.15a is a typical example of one

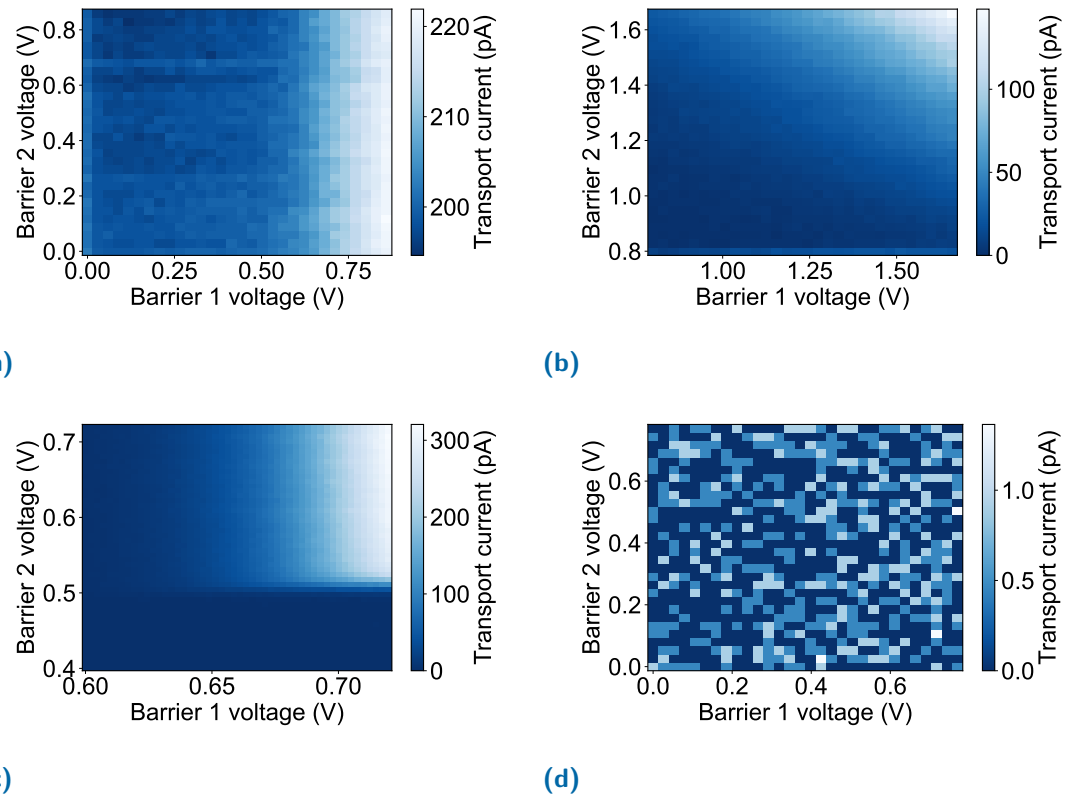

Figure 3.15: Failure modes of a SET barrier-barrier pinch-off sweep. (a) Sweep with only one barrier influencing the transport current. (b) Sweep for which the two barriers have a strong cross-talk. (c) No sharp pinch-off. Conductive region fades out to one side. (d) Only noise and no transport current despite previously possible accumulation in the SET.

barrier gate (here barrier 2) which does not have any influence on the current. While sweeping the first barrier gate allows for the current to be pinched off, the second barrier gate seemingly does not influence the measurement at all. The exact opposite is depicted in figure 3.15b. Here, the conductive region is triangular instead of rectangular. This

means that the barrier gates strongly influence each other and the pinch-off voltage of each barrier is highly dependent on the other. Such a high crosstalk is undesirable as we want to be able to control both barrier gates individually. The third example, figure 3.15c, shows a conductive region which has the right shape, but is faded out to one side. For such a result, it is not possible to properly define a pinch-off voltage due to the lack of a sharp transition between a current flowing and no current flowing. However, both barrier gates seem to be individually controllable in this sample. As a result, a sample showing this behaviour could be further investigated if handled carefully. The last example in figure 3.15d shows the rare result that we do not see any kind of conductive region, making it basically impossible to further operate this SET. This could be a consequence of an insufficient time stability. Trying to reaccumulate the device might resolve this issue.

3.3.4 SET barrier-plunger pinch-off sweeps

In the same manner as for the previously explained barrier-barrier sweeps, we now want to verify the functionality of the plunger gate as well as characterize its cross-talk to the adjacent barrier gates. Again, we perform a two-dimensional sweep. On the one axis, we sweep the two barrier gates XB1 and XB2 simultaneously. The voltage range for each barrier is given by a diagonal line cut through the conductive region in the last measurement. On the other axis, we sweep the voltage applied to the plunger gate XP. This is sketched in figure 3.16. Here, we expect a similar plot as for the barrier-barrier sweep, as shown in the example figure 3.17. The voltage ranges and measurement parameters for

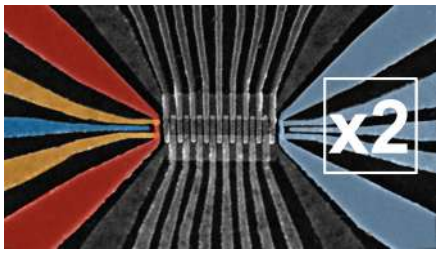

Figure 3.16: Gate scheme for SET barrier-plunger pinch-off sweeps. The gates on the operating point voltage V_{op} are indicated in red, the gates being swept in dark blue and yellow. All gates of the right SET are colored in light blue to indicate that this measurement is repeated for both sides.

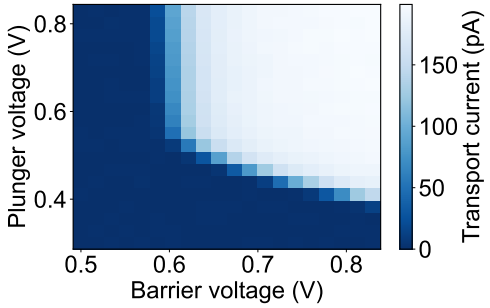

Figure 3.17: A successful SET barrier-plunger pinch-off sweep showing a well-defined conductive region in die upper right corner.

this are listed in table 3.3. For this measurement, it is a bit harder to classify distinct failure modes. This is because even for a broken or heavily damaged plunger, we can very likely form a quantum dot in the final measurement and use the SET as intended. Also,

Table 3.3: Measurement parameters for an SET barrier-plunger pinch-off sweep.

Mode	Gate	Instrument	Voltage	Steps	Break Condition
Variable	XB1 XB2	DecaDAC	0V - V_{op}	20	I(OX) > 1 nA
Variable	XP	DecaDAC	-0.5V - V_{op}	20	I(OX) > 1 nA
Constant	XT	SMU	V_{op}		
Constant	OX1 OX2	LIA	100 µV		

plots that show a faded out conductive region, which we would have classified as failure or at least as not optimal before, can be sign of a good and normal working plunger, as it behaves quite different from the barrier gates. As a result, this measurement can be generally rated as optional and a device can yield perfect results with an unsatisfactory measurement here. Still, we give two failure modes here, for which a further use of the device should be avoided. The first failure mode is that the barriers have an influence on the conductive region, but the plunger does not lead to any change in current. An exemplary plot is shown in figure 3.18a. It is evident that this failure mode directly corresponds to the barrier-barrier sweep failure mode from figure 3.15a. In the same manner, also for this measurement, it is possible that we cannot find any gate voltage configuration that yields a transport current, as shown in figure 3.18b. In addition to the

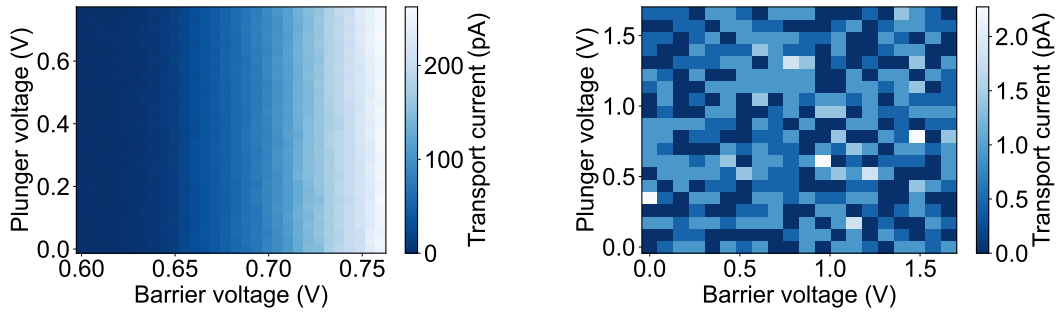

(a) **(b)**

Figure 3.18: Failure modes for a SET barrier-plunger pinch-off sweep. (a) Conductive region only one-sided, the plunger does not influence the transport current. (b) No transport current visible despite functional previous checks.

typical failure modes, this measurement step also features something that could easily be identified as a failure, but is certainly not. As shown in figure 3.19, it often happens that the conductive region is seemingly composed of two different parts. In this example, these parts switch at a barrier voltage of about $V \approx 0.77\,\mathrm{V}$. In both cases, plunger and barrier work as intended.

The split into these two regions is because different current paths can be taken. Either the entire region defined by the two barrier gates and the plunger accumulates, which would be the intended current path, or only the barriers pinch off, leading to a slightly shifted current path that does not flow through the full SET region. However, the presence of both regions more strongly suggests, rather than excludes, that the SET is functional.

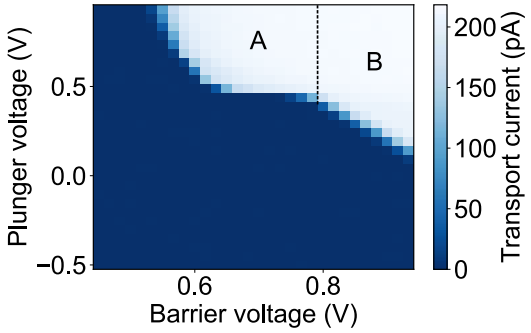

Figure 3.19: Different current regions in a SET barrier-plunger pinch-off sweep. One region (A) represents the envisaged current path, the other region (B) corresponds to a current under the barriers but not under the plunger of the SET.

3.3.5 One-dimensional SET plunger pinch-off sweeps

The next measurement serves as an additional check of the plunger gate. In comparison to the previous experiment, it is only one-dimensional, neglecting the exact behaviour of the barriers and only trying to enforce an evident reaction to applied voltages, see figure 3.21. While potentially giving additional information about the plunger behaviour and also potentially making Coulomb oscillations visible, we use this step in the measurement workflow mostly as optional measurement in case one of the previous two measurement series failed. If this happens, we can still be sure about the functionality of the plunger gate, without taking the influence of the barrier gates into consideration. A common result of such a measurement for a working plunger is shown in figure 3.21. As this sweep is only one-dimensional and only one gate is being swept here, the possible failure modes are relatively limited. As mentioned before, it is possible that the current does not change with the plunger voltage, as shown in figure 3.22. This is the only failure mode usually observed for this kind of measurements.

3.3.6 Accumulation of a current through the channel

Now that all the components for both SETs are characterized, one can proceed with testing the remaining gates, which form the channel of the SQS. To test these, we first want to see if it is possible to get a current flowing through the channel. For this, we start by biasing the ohmic contacts of one SET with a voltage of 1 V, while we do not apply a bias

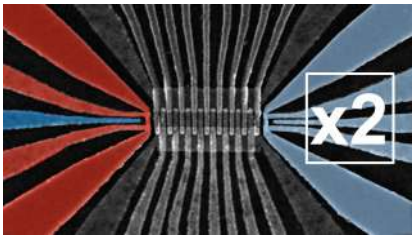

Figure 3.20: Gate scheme for a one-dimensional SET plunger sweep. The dark blue gate shows the plunger being swept, the gates marked in red are at the operating point voltage V_{op}. All gates of the right SET are colored in light blue to indicate that this measurement is repeated for both sides.

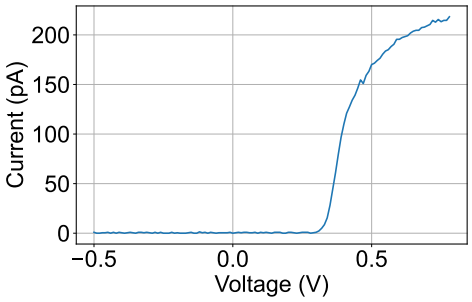

Figure 3.21: Transport current for a SET plunger 1D pinch-off sweep.

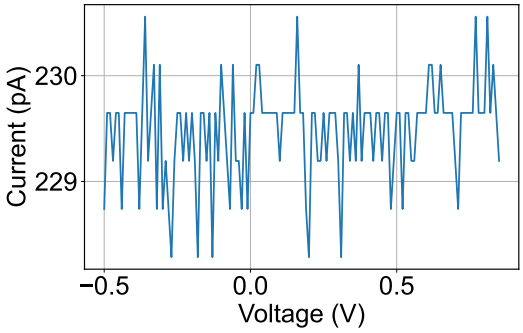

Figure 3.22: SET plunger 1D pinch-off sweep. Even for high negative voltages, we only observe a fluctuating transport current, but no pinch-off.

to the other side. Thus, the latter does not need to be fully functional in the sense that not all gates have to work as intended. Important here is only that a transport current is measurable. All gates of each SET will however be set to their respective operating points. Also, we set the frequencies of both LIAs to the same value to ensure that the current can be measured in both SETs in the same way, meaning that otherwise one LIA would filter out the current from the other LIA. Starting from 0 V, we apply a positive voltage to all gates in the channel. This is shown in figure 3.23. At a certain voltage V_{ch}, the channel is completely open, and a fraction of the current flowing through the biased SET can instead flow through the channel till it reaches the ohmic contact on the other, not-biased side. Consequently, we expect a result like figure 3.24 when plotting the transport currents measured with each LIA. The parameters of this measurement are again summed up in table 3.4. In this measurement, there are only two realistic cases. Either, our measurement works as discussed before. Or it does not, which in return is also our only failure mode. There is one easy step that can help to fix such a failure, which

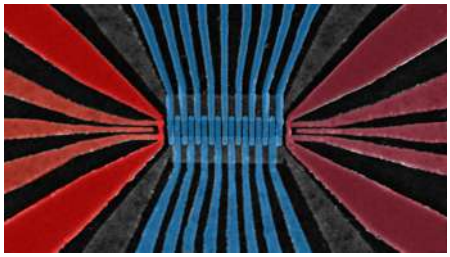

Figure 3.23: Gate scheme for accumulating a current through the channel. Each SET is set to its corresponding operating point, all the gates in the channel are swept together.

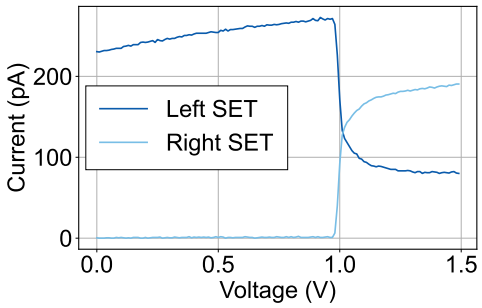

Figure 3.24: Currents through each SET for the channel measurement. At about 1 V, the current in one SET increases while the current in the other SET decreases, showing that a current flows through the channel.

will be discussed in the following section. It is worth noting that the break condition of this measurement is different to the previously described experiments. We do not want too apply high voltages that can lead to a charged device. Thus, once we see clearly that forming a current through the channel is possible (which would be at about 1 V in figure 3.24), we can stop the measurement as we do not get any additional information (but a higher risk of charging) from continuing the sweep.

Table 3.4: Measurement parameters for accumulation of a current through the channel.

Mode	Gate	Instrument	Voltage	Resolution	Break Condition
Variable	Channel	DecaDAC	0V - 1.5V	10 mV	I(OX) > 1 nA
Optional	ST SB	DecaDAC	0V - 1.5V	10 mV	I(OX) > 1 nA
Constant	LB1 LP LB2	DecaDAC	$V_{\mathrm{op},L}$		
Constant	RB1 RP RB2	DecaDAC	$V_{\mathrm{op},R}$		
Constant	LT	SMU	$V_{\mathrm{op},L}$		
Constant	LT	SMU	$V_{\mathrm{op},R}$		
Constant	OL1 OL2	LIA	100 uV		
Constant	OL1 OL2	LIA	0.4 µV		

3.3.7 Screening-gate aided channel accumulation

As an important note before this section, everything here is optional in the sense that this step in the measurement routine would be and should be skipped if the measurement previously presented was successful. However, as this is often not the case, and the mea-

surement presented here is often forgotten, we decided to dedicate it its own chapter and promote it to a step in the workflow. For the measurement itself, we repeat the procedure of the previous step, except that now in addition to all gates in the channel we also apply a voltage to both screening gates ST and SB, as shown in figure 3.25. This almost guarantees a current in the channel as it strongly enhances the tendency of electrons to also flow through the channel to the SET on the other side. An example of why this measurement

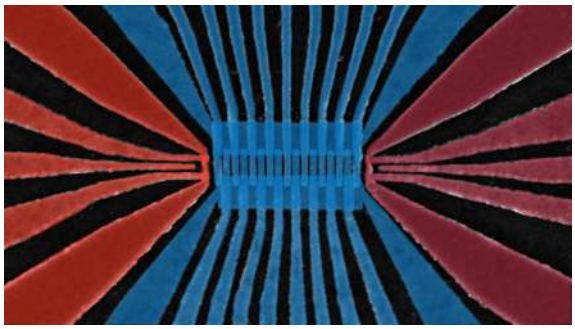

Figure 3.25: Gate scheme for screening-gate aided accumulation of a current through the channel.

is important is shown in figure 3.26. First, in figure 3.26a, you see a failed measurement of the channel current without the screening gates. Next to it, figure 3.26b, you can see that additional sweeping of screening gates leads to a functional and working channel. One

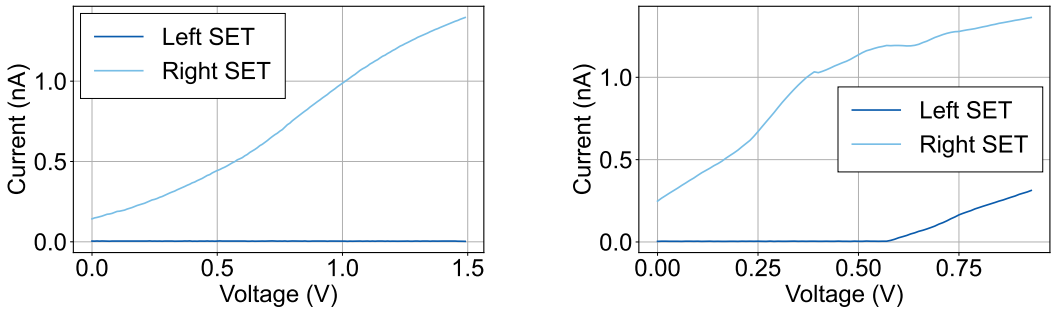

(a) **(b)**

Figure 3.26: Measurement of currents through both SETs to prove a current flowing through the channel. (a) Measurement without screening gates. No change in currents that indicate a current flowing to the channel can be seen. (b) Measurement of the same device, now with screening gates. Here, a current through the channel will be formed.

drawback of this method is however, similar to the accumulation of the SET, sweeping the screening gates together with all the other gates usually means that the voltage applied to the screening gate is higher than necessary. This could already be improved by step-wise increase of the screening gate voltages and repeating the normal channel measurement once for each step. Regardless of this, our implementation has the advantage that it is simply faster and overall allows for a higher throughput of samples.

3.3.8 Individual gate and gate-set pinch-off measurement

Lastly, knowing that a current through the channel is generally possible, we try to pinch-off this current by sweeping down each individual clavier gate or gate set until the current path is blocked, as depicted in figure 3.27. The voltages applied to each gate are summarized in table 3.5. In a perfect case, as in figure 3.28, all gates and gate sets can pinch of the current individually, proving that they all work as intended and none of them are broken or otherwise damaged.

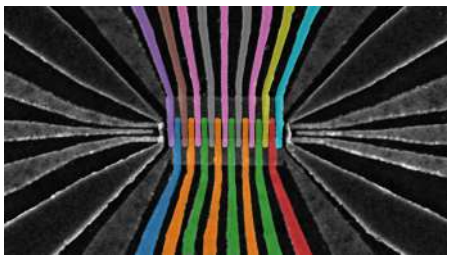

Figure 3.27: Gate scheme for pinch-off measurements of individual gates or gate sets. Each sweep is shown in a different color. For each sweep, all other gates are on the channel voltage V_{ch}.

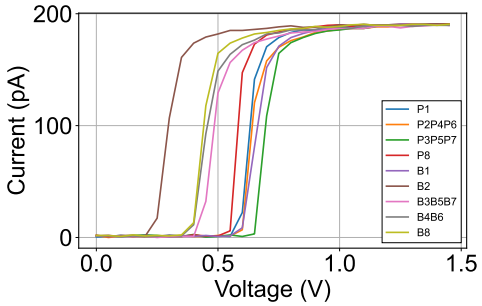

Figure 3.28: Pinch-off measurement of individual gates and gate sets.

Table 3.5: Measurement parameters for individual gate and gate-set pinch-off measurements.

Mode	Gate	Instrument	Voltage	Resolution	Break Condition
Variable	Individual gate or gate set	DecaDAC	0V - 1.5V	10 mV	I(OX) $>$ 1 nA
Constant	Other channel gates	DecaDAC	V_{ch}		
Constant	ST SB	DecaDAC	V_{scr}		
Constant	LB1 LP LB2	DecaDAC	$V_{\mathrm{op},L}$		
Constant	RB1 RP RB2	DecaDAC	$V_{\mathrm{op},R}$		
Constant	LT	SMU	$V_{\mathrm{op},L}$		
Constant	LT	SMU	$V_{\mathrm{op},R}$		
Constant	OL1 OL2	LIA	100 uV		
Constant	OL1 OL2	LIA	0.4 uV		

The voltages and voltage ranges applied to each gate are displayed in table 3.5. For this measurement, there are two common failure modes that can apply to each individual gate. Either, as for example in figure 3.29a, the transport current does not change at all when applying a voltage to the gate. This can happen when the gate is completely broken or if a bond-wire from interposer to the sample was forgotten for this gate or because the bond has peeled off. Alternatively, as shown in figure 3.29b, the gate shows some voltage dependent behaviour, but rather a linear curve instead of the typical pinch-off curve. A reason for this could be strong cross-coupling of the channel gates. In both cases, it is also possible that the pinch-off happens for negative voltages, which are often not tracked in this measurement. So one should take into account that in some cases, a failure for this measurement does not necessarily mean the device is broken. Also, with sweeping each gate up and down, hysteresis effects can be induced. Because of this, one should pay attention to the order of the measurements to see if non-working gates could possibly be explained that way. With this measurement, the workflow is complete. A sample

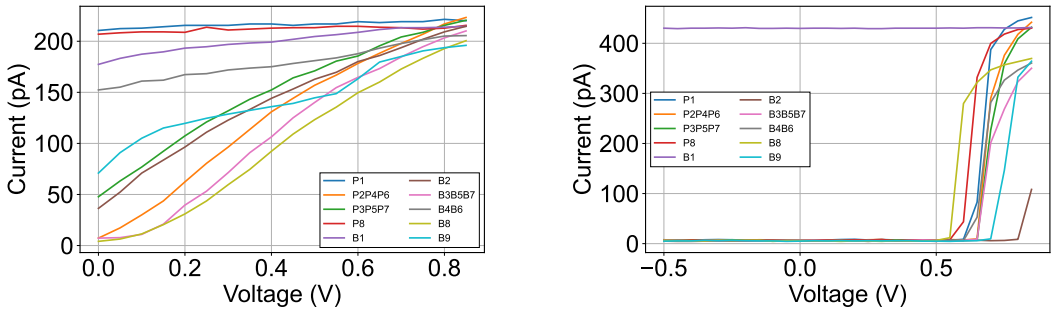

Figure 3.29: Failure modes of pinch-off measurements of individual gates and gate sets. (a) Linear current to voltage relation for which gates work, but do not show a sharp pinch-off. (b) Gate B1 is not bonded and does not respond to changes in voltage. Exemplary for how a broken gate behaves.

passing all of these tests will be classified as perfect and completely suitable for further experiments. However, one should note that the thresholds and tests mentioned here are selective in a way that false-positives are surely excluded. As a trade-off, false-negatives, meaning fully functional samples that have been sorted out in the workflow, are likely so that this possibility should be considered before destroying certain samples.

3.4 Improvements with automatic tuning

While the workflow described in the previous chapter works relatively well for a small number of samples having to be characterized, scaling up this pre-screening approach is not sustainable. This is mainly because it has three major disadvantages that can only be further optimized by a larger change of the setup and measurement protocol. Firstly,

the measurement is still fairly time consuming. Decreasing this time needed to mount, cool down and measure the samples is currently being worked on. The setup described in chapter 3.1 is about to be completely replaced with a new setup that circulates helium and allows for cooling down multiple samples at the same time. Also, the measurement framework will be migrated from QcoDeS to QuMADA [88] soon. This upgrade then allows for buffered measurements which are significantly faster. Secondly, the current workflow needs constant supervision of the measurements. We have to manually control if each measurement terminates as expected or if we run into any of the failure modes. Then, we have to adapt the next action (e.g. measuring again with new voltage ranges, different resolution, or skipping steps in the measurement workflow) according to the outcome of the previous one. As a third disadvantage, the algorithm used to pre-screen the samples is held as simple as possible. As an example, always sweeping in the same, fixed voltage ranges yields results of very different quality, depending on how centered the main feature we want to observe in the measurement is. Another example is the accumulation of charges in the QW. For this measurement, we sweep all gates with the same voltages, while it would maybe be both sufficient and more protective to find a combination of voltages that yields the wanted effect without increasing each voltage more than necessary. To overcome the second and third disadvantage, we recently made the first step by implementing parts of our workflow in the *tuning toolkit*, a library developed by and set up on our experiment by Paul Surrey [89]. We further divide this section into two parts, namely the implementation for one-dimensional and for two-dimensional sweeps. In each part, we will give a short explanation of what the *tuning toolkit framework* (ttf) does, what a typical output is and how it improves our measurement beyond the above stated intention of making constant supervision obsolete.

3.4.1 Automated tuning of one-dimensional sweeps

For one-dimensional sweeps, the main problem of the current measurement workflow is that the same voltage is applied to all SET gate. For a functional device, the voltages actually needed can be much lower than the voltage we apply, just finding the different ratio of voltages for each gate is a complicated task. For this, we use a one-dimensional tuning function. This function sweeps each gate of a SET individually and only in a very small region. It calculates the gradient of the voltage-dependent ohmic current and steps each gate according to this gradient. An example of this is shown in figure 3.30, which is put out by said function after the tuning algorithm terminates. It shows how in each step the gate voltages are individually changed so that a loss function describing the whole SET is minimized. To further quantify the effectiveness of this function, we have performed pinch-off measurements of each of the SET gates both with this new *gradient accumulation* (GA) algorithm as well as with the standard algorithm which we used before. These pinch-off measurements are plotted in figure 3.31. Two curves of the same color

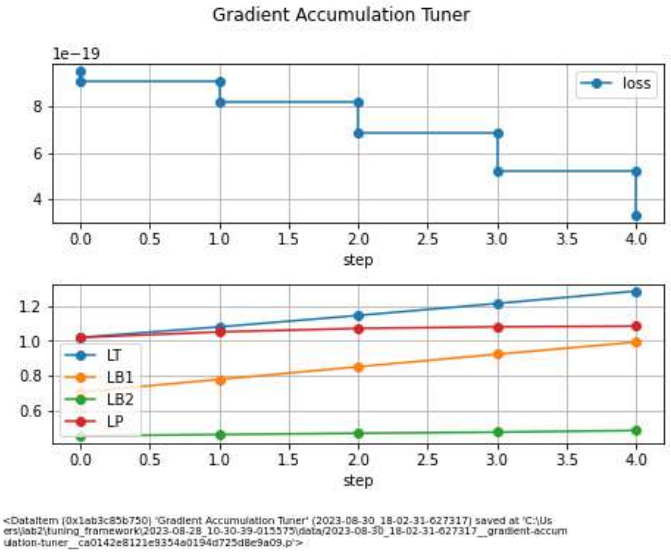

Figure 3.30: Output plot of the GA tuning function, showing a loss function being reduced in multiple step through individually adjusting the voltages of each SET gate.

correspond to the same gate, the darker shade of each color indicates the measurement with the GA algorithm. It is remarkable that this new tuning algorithm leads to an earlier pinch-off for all gates tested. However, it is yet to be determined if this is systematically valid for a large number of samples.

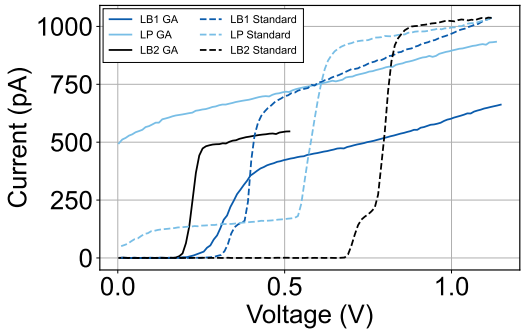

Figure 3.31: Comparison of the standard algorithm for accumulating a current through an SET and the GA algorithm. Individual pinch-off measurements for each SET gate are plotted for both methods.

3.4.2 Automated tuning of two-dimensional sweeps

The main issue with the two-dimensional sweeps is that we perform these measurements without knowing much about the properties of each SET before. Thus, the feature we want to see (e.g. the conductive region in a barrier-barrier sweep) can be barely to not visible at all due to the chosen voltage ranges. Even though having a barely visible feature can be enough to verify functionality in some cases, it is not suitable for further

analysis or derivation of device characteristics. Thus, we implemented a function that automatically finds the conductive region in a barrier-barrier sweep. This is done by performing a low-resolution measurement at an almost randomly initialized position and then calculating the gradient of these data to determine in which direction to change the voltage ranges. These steps (coarse measurement, calculating the gradient, changing voltage ranges for the next measurement) is performed N_{tune} times and terminates before if the lower left corner of the conductive region is found. This is shown in figure 3.32. After this, a full high-resolution scan as in figure 3.33 is performed. This scan has the corner of the conductive region centered and is thus suitable to read off pinch-off voltages and further device characteristics. Here we have given the barrier-barrier sweeps as an example. However, this function is directly applicable to barrier-plunger sweeps as well. Consequently, with these results, this function strongly enhances the quality of the two-dimensional sweeps without needing more resources.

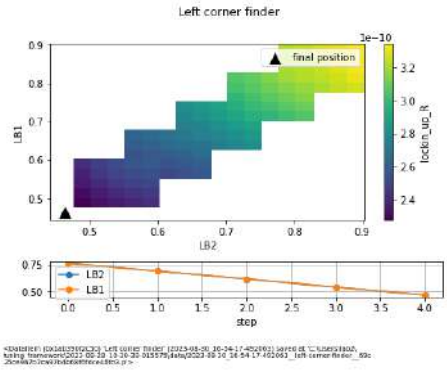

Figure 3.32: Output of the corner finder function, showing how the corner in an SET barrier-barrier sweep is approached by several low resolution scans. For each step, the voltages applied to the two barriers are adjusted.

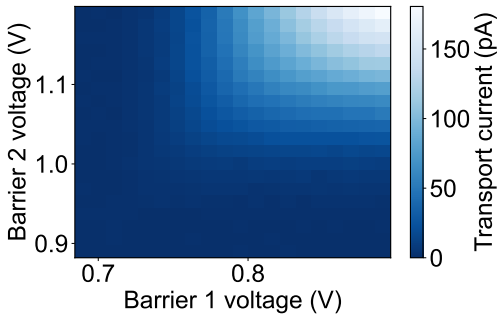

Figure 3.33: Measurement of an SET barrier-barrier sweep after finding the corner with the new algorithm. The corner of the conductive region is centered in this scan.

3.5 Sample statistics and heterostructure comparison

This section deals with a broader analysis and comparison of the samples we measured. The goal of this analysis goes beyond the initial purpose of pre-screening the devices, which is to identify good candidates for upcoming measurements. Here, we especially want to qualitatively (section 3.5.2) and quantitatively (section 3.5.3) compare different

heterostructures, draw conclusions regarding growth of the heterostructure and fabrication of the devices and judge which of the heterostructure to use in future fabrication rounds.

3.5.1 Sample overview and heterostructure information

The samples used for our measurements are always fabricated in batches, where samples of the same batch were fabricated with the same settings in the same run. We performed the aforementioned measurements on three batches, labelled batch 16, batch 17 and batch 19. Batch 16 will not be further discussed as it was only used for training purposes. Batch 19 was fabricated to test different atomic layer deposition (ALD) processes. The results of these measurements will be futher described in section 3.6. In this section, we will focus on batch 17 only. This batch includes samples fabricated on eight different heteorstructures from four different suppliers. Their specifications, mainly consisting of the thicknesses of the layers described in section 2.4.1 are listed in table 3.6. In total, 72 samples of this batch were investigated.

Table 3.6: Heterostructures used in batch 17.

Heterostructure	QT694	QT734	R2159	R2203	L13RC	L13RD	SJZ367-13	SJZ367-15
Supplier	TU Delft	TU Delft	Uni Regensburg	Uni Regensburg	Lawrence S.R.L.	Lawrence S.R.L.	IHP	IHP
Si cap	/	/	1.5 nm	1.5 nm	2nm	2nm	1 nm	1 nm
SiGe	30nm	30nm	45 nm	45 nm	30nm	30 nm	35 nm	35 nm
QW	9 nm	5.3 nm	10 nm	10 nm	10 nm	10 nm	11 nm	13 nm

3.5.2 Qualitative analysis

In a first step, we can perform a qualitative analysis of all 72 samples we measured. This means that we count how often we performed a specific measurement as well as how often it succeeded and compare this for different heterostructure (HS). This shows us both how dominant certain heterostructures were in our measurements and how well they performed. The values for this analysis were taken from the overview table that was developed and maintained during the experiments. To start, we look at the number of working SETs and the total number of measured SETs, shown in figure 3.34. Here, a working SET is defined as an SET in which we were able to successfully accumulate a transport current above 200 pA through it. The histogram illustrates that our primary measurements were from the QT- and R- heterostructures. Specifically, these structures have a QW composed of isotopically purified ^{28}Si. The QT- heterostructures contain 800 ppm of residual ^{29}Si, while the R-heterostructures have less than 60 ppm of this residual isotope. We find that for the QT734 HS, exceptionally many SETs work, while for the R2203 HS only exceptionally few do. Furthermore it is evident that both SJZ367 heterostructures have a large number of working SETs. However, one should note that for these heterostructures the sample size is very small.

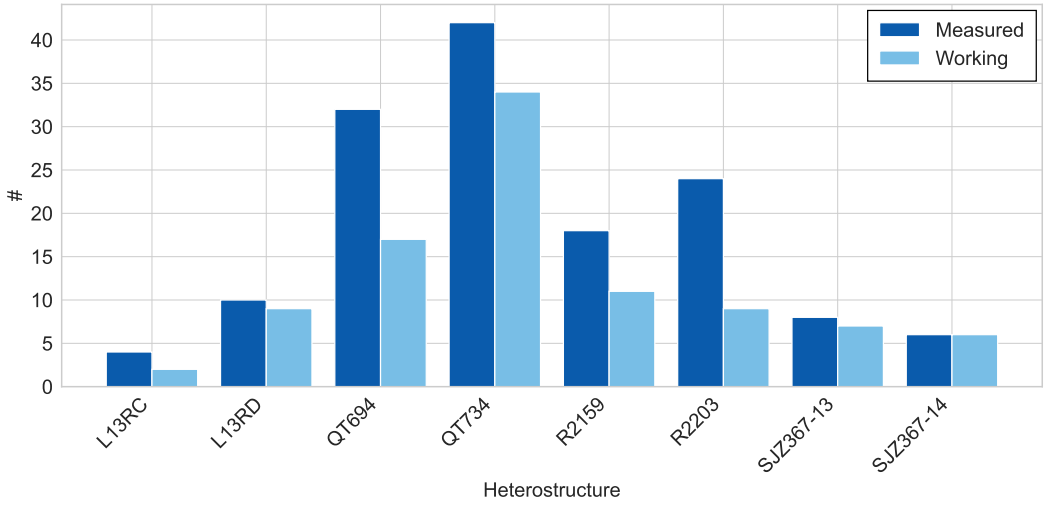

Figure 3.34: Histogram of measured and working SETs for different heterostructures. The dark blue bars show the number of measurements of this type we performed, the light blue bar shows the number of successful measurements.

For each SET that we accumulated a current through, we next tested time stability of these SETs. The SETs that are stable in time compared to the total number of working SETs is shown in figure 3.35. Generally and as expected, the numbers presented here are

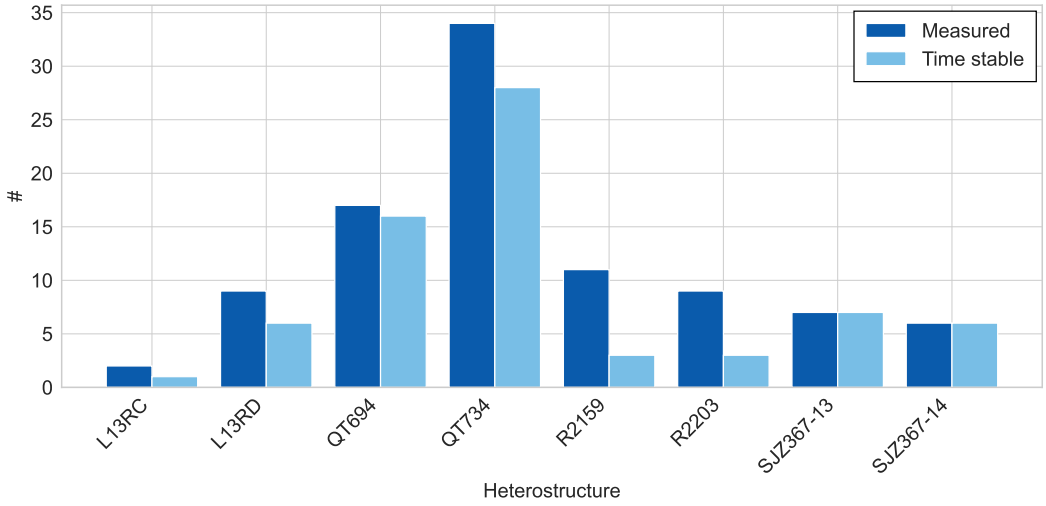

Figure 3.35: Histogram of time stability measurements for different heterostructures. The dark blue bars show the number of measurements of this type we performed, the light blue bar shows the number of successful measurements.

similar to the bars in figure3.34. However, there are a few notable deviations. We see that the QT694 HSs has in almost all cases SETs that are stable in time. This is surprising as only about half of the SETs have worked in the first measurement. On the other hand, the number of time stable SETs from the R-heterostructures is remarkably low. The next histogram, figure 3.36 shows the number of samples for which both SETs are working in dark blue. This is the prerequisite for a measurement of a current through the channel.

In the same figure, the number of times in which we could detect this current is shown in light blue. Here the QT694 HS is again outstandingly good, as all the samples that passed the previous tests work here. The last part of this qualitative analysis is the histogram

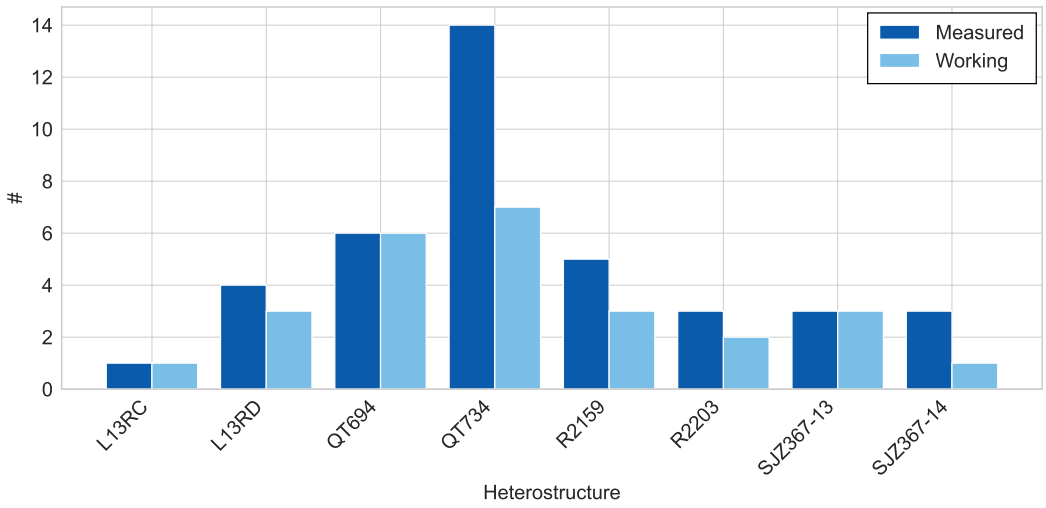

Figure 3.36: Histogram of channel current measurements for different heterostructures. The dark blue bars show the number of measurements of this type we performed, the light blue bar shows the number of successful measurements.

in figure 3.37. This shows how well the individual pinch-off measurements have worked. This measurement is possible for each successful measurement of the current through the channel. It is worth noting here that we only define this experiment as fully working, if all 10 individual pinch-off sweeps showed the desired result. Thus, rational numbers as for example 0.7 in a bar would suggest that 7 out of 10 individual pinch-off measurements have worked, making up 0.7 of one full measurement. Notable here is that especially the R2203 HS performs badly and only very few of the gates can be used to pinch-off the current through the channel.

3.5.3 Quantitative analysis

Lastly, we can perform a quantitative analysis of some of the measurements. This means that we look at specific values of certain parameters and see how they behave depending on the heterostructure of the sample. One example of such an analysis is shown in figure 3.38. This plot shows the value of the pinch-off voltage V_{po} (the voltage at which the current starts rising in the accumulation measurement) for each heterostructure. The random spread of the points in the horizontal direction is only to improve visibility and has no physical meaning here. Here, it is remarkable that especially for the QT734 HS, all of these values are very close together, being only in a voltage range from about 0.6 V to 1 V.

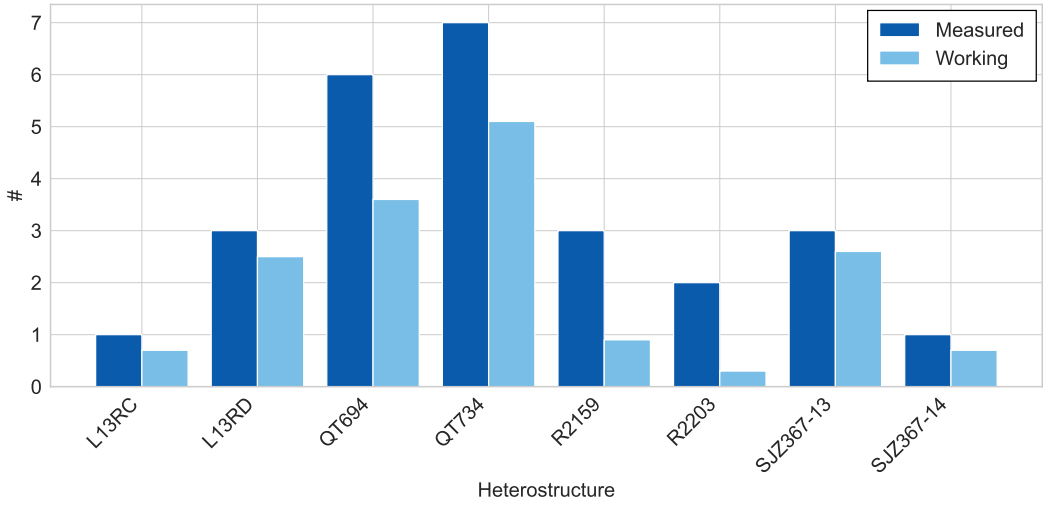

Figure 3.37: Histogram of individual pinch-off measurements for different heterostructures. The dark blue bars show the number of measurements of this type we performed, the light blue bar shows the number of successful measurements. Fractional numbers correspond here to only a fraction of the pinch-offs being possible.

It is also noticeable that the pinch-off voltages for the R2203 heterostructure are comparatively high, often even beyond our initial voltage window of 0 V to 1.5 V. As such high voltages might lead to the device being charged, it is desirable to have as low voltages as possible. The exact same trends and voltage regions can be seen in figure 3.39. This plot

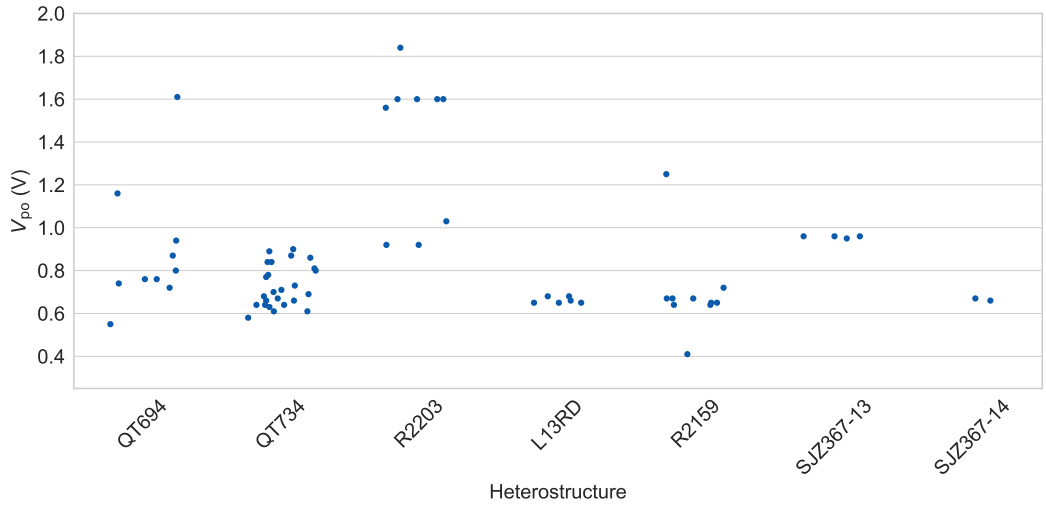

Figure 3.38: Comparison of the pinch-off voltages V_{po} for different heterostructures. The random horizontal spread ensures visibility and has no physical meaning.

shows the voltage V_{th} at which the operating point threshold of 200 pA is reached. As this often comes only shortly after the current starts rising, the strong correlation of these two plots is not surprising. Figure 3.40 makes a statement about the time stability of the samples measured. For this, the transport current at the starting position I_{start} is plotted

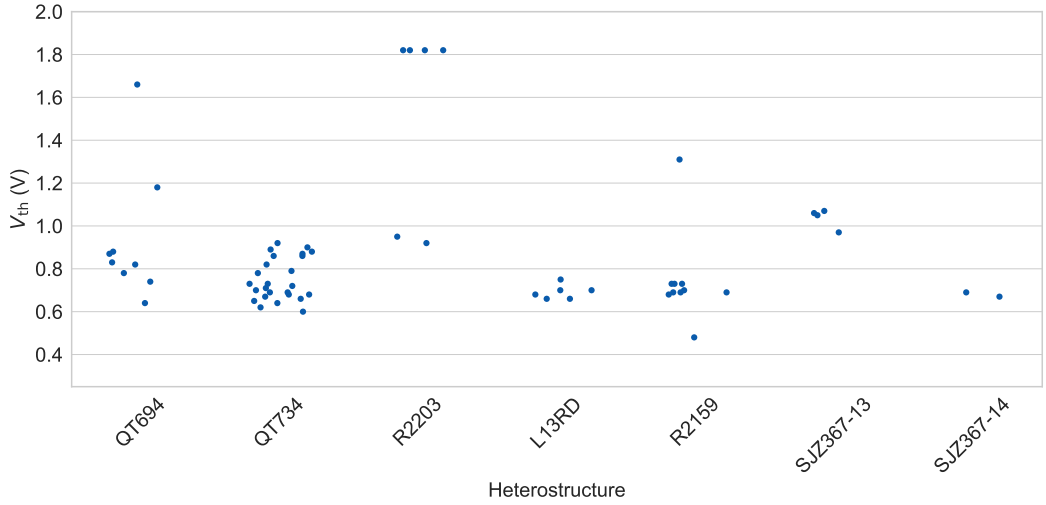

Figure 3.39: Comparison of the threshold voltages V_{th} for different heterostructures. The random horizontal spread ensures visibility and has no physical meaning.

on the y-axis. The x-axis shows the percentage of this start current value after the time of 80 s. The heterostructure is encoded in the color of the data points. The percentage of the start current was extrapolated by employing a linear fit to the current over voltage curve and taking the value of that fit function at 80 s. This way, the effects of noise are minimized. We observe that most of the points cluster in a region above a transport current

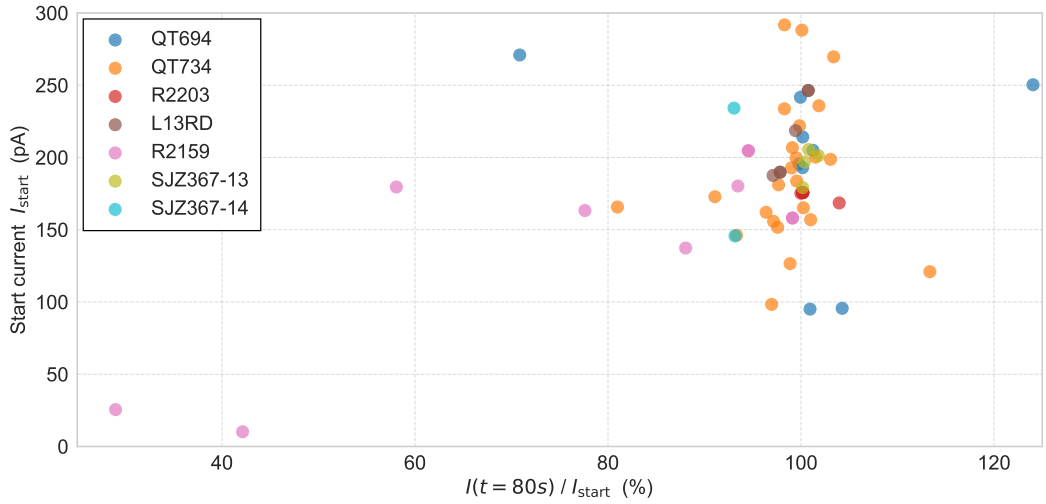

Figure 3.40: Evaluation of the time stability measurements for different heterostructures, indicated by different colours. Start current and the percentage of this current after 80 s are shown.

of 150 pA and around an x-value of 100 %, which generally proves that most samples are stable in time. However, it is worth noting that comparably many samples of the R2159 HS are not in this window, again indicating a relatively bad time stability. Also, we see many samples for which the ratio of the start current exceeds 100 %. While this sounds illogical at first, it can easily be explained by effects like charging of the device or similar.

However, this means that contrary to intuition, these values are also not to be regarded as good and desirable. In the next step of this analysis, we investigate different properties of the corner points of the SET barrier-barrier pinch-off sweeps. These corner points contain various information, as the individual pinch-off voltages of each barrier gate V_{po}^{B} and the symmetry of the SET. To start off, we plot the values for each individual barrier pinch-off voltage V_{po}^{B} for the different heterostructures we investigated. This is depicted in figure 3.41. Similar to previous measurements, we find that the QT734 heterostructure works best, as visible by all the data points being in a small voltage range and generally at low voltages. Other heterostructures, as for example QT694 or R2159 show an overall similar behaviour, but data points distributed over a wider range, making them slightly worse here. For the R2203 heterostructure, it was comparably hard for the algorithm to find the corner. This combined with a low number of working SETs accounts for the very few data points visible here. Because of similar reasons, the L13RC heterostructure is not shown at all. Another property interesting to look at is the *symmetry* S of the corner, as it

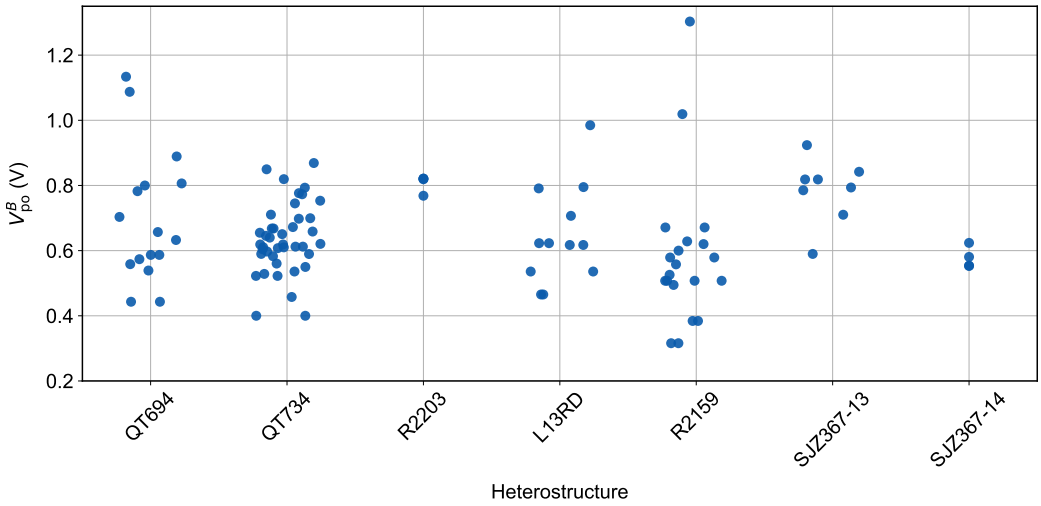

Figure 3.41: Comparison of the barrier-barrier pinch-off voltages V_{po}^{B} for different heterostructures. The random horizontal spread ensures visibility and has no physical meaning.

contains information about both barriers and the corner point instead of only evaluating one barrier at a time. It is defined by

$$S = \begin{cases} \frac{V_{\mathrm{po}}^{B1}}{V_{\mathrm{po}}^{B2}} & \text{if } V_{\mathrm{po}}^{B2} > V_{\mathrm{po}}^{B1} \\ \\ \frac{V_{\mathrm{po}}^{B2}}{V_{\mathrm{po}}^{B1}} & \text{if } V_{\mathrm{po}}^{B1} > V_{\mathrm{po}}^{B1} \end{cases} \tag{3.5.1}$$

giving a number $\leqslant 1$, with numbers closer to one meaning that the corner is more symmetric. This quantity is shown in figure 3.42 for the different heterostructures in use. We note that QT694 performs best here, with over 85 % symmetry for a large number of data points.

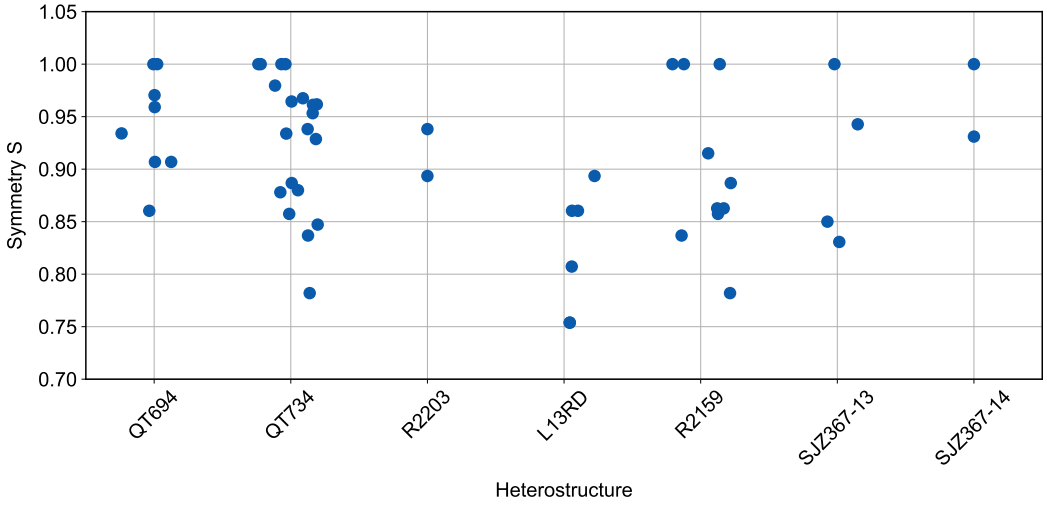

Figure 3.42: Evaluation of the barrier-barrier pinch-off sweep conductive region corner symmetry S for different heterostructures. The random horizontal spread ensures visibility and has no physical meaning.

Lastly, we evaluate a histogram of the V_{po}^{B} voltages for one heterostructure. We will use QT734 as this was the heterostructure for which we measured the most samples. The histogram including a Gaussian fit is shown in figure 3.43. Evidently from figure 3.43,

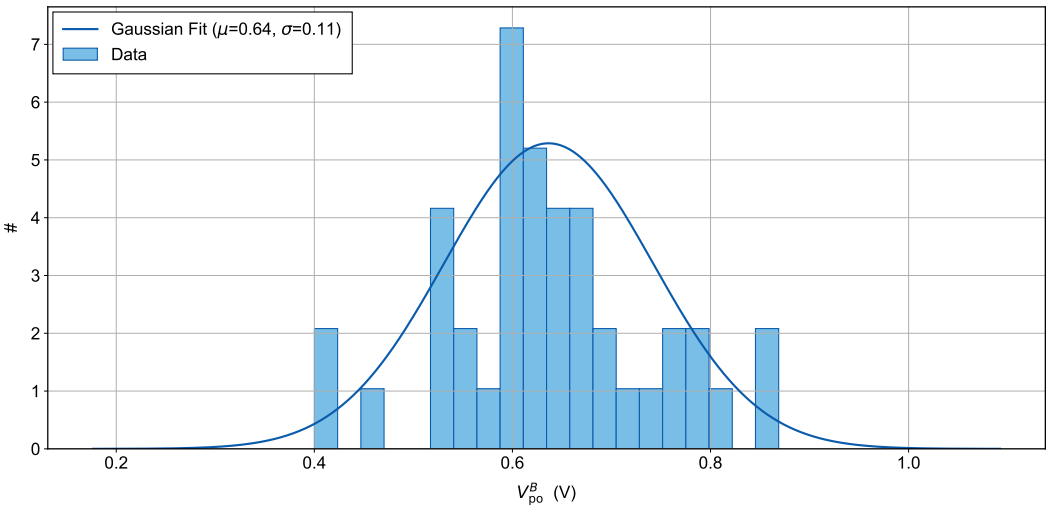

Figure 3.43: Histogram of the barrier pinch-off voltages V_{po}^{B} for the QT734 heterostructure including a Gaussian fit to the data.

fitting a normal distribution to the values of V_{po}^{B} works relatively well and describes the data sufficiently. If we would have more data points for the other heterostructures, a similar analysis could be performed for all of them to have a well-founded comparison. Similarly, due to a too low sample size, the measurements of the current through the channel and the individual pinch-offs could not be analyzed more rigorously.

3.6 Comparison of different ALD methods by testing the oxide

In the fabrication of the SQS devices, the oxide is deposited on the sample by *atomic layer deposition* (ALD), which is a method for uniform deposition films that can be as thin as a single layer of atoms [90, 91]. This method comes in two different variants. On the one hand, there is the thermal ALD process [92], in which Al_2O_3 is synthesized from trimethylaluminum (TMA) and water in a heat reactor. On the other hand, there is the plasma enhanced ALD process [93], in which an O_2 plasma is used instead of water. As recently a new ALD tool has been installed, we briefly want to compare the behaviour of two samples for which different ALD methods were used. The samples described here are long SQS samples from batch 19. We want to quantify the stability of the oxide and intentionally try to irreversibly break it. For this, we first connect the screening gates to one port of a Keithley SMU and measure the current for each possible gate or gate set connected to the other port of the same SMU. We sweep the voltage in a range from $-2\,\mathrm{V}$ to $2\,\mathrm{V}$, as we usually operate our devices in this voltage range. With this, we want to test if the oxide breaks at such an early stage that we could not use the samples. The results of these measurements are shown in figure 3.44. From this measurements it is

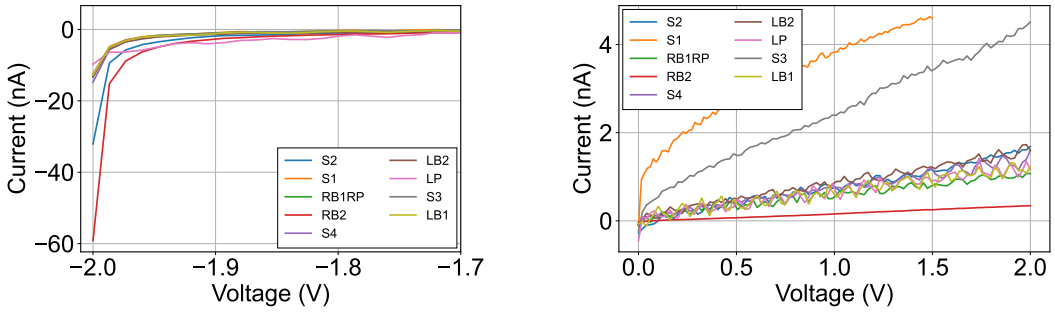

Figure 3.44: Results of the oxide test for moderate voltages and different gates. (a) Sample with the oxide deposited by a plasma enhanced ALD process. (b) Sample with the oxide deposited by a thermal ALD process.

evident that the oxide behaved normally and did not break at the usual voltage ranges, as we would expect a current that is by orders of magnitude larger if the oxide was broken. This is clear from figure 3.45. For this measurements, we increased the voltage up to a point at which we see the aforementioned high current. For the thermal ALD processed sample, this happens at about 8.8 V, while the oxide breaks down at 10.6 V for the plasma enhanced ALD processed sample. Due to the low sample size this is certainly not enough for a comparison of these two methods. But as in both cases the voltage needed to break the oxide is similar and comparably high, it can be expected that both processes work similarly well and none of them comes with greater errors.

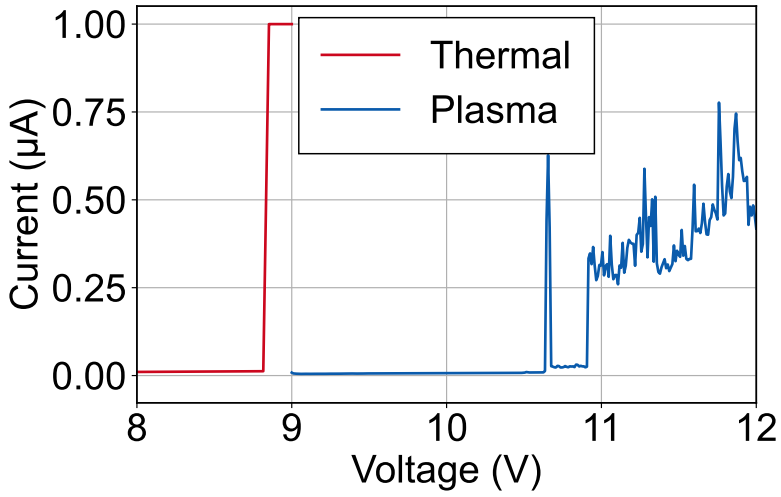

Figure 3.45: Comparison of the voltages at which the oxide irreversibly breaks. The samples compared here have the oxide deposited by a thermal or plasma enhanced ALD process, respectively.

Chapter 4

Charge shuttling and parameter optimization

Having found and characterized a fully functional sample with the previously described measurement routine, we now come to the part where we use this sample for experiments at millikelvin temperatures, as such low temperatures will be needed to operate our devices. As a first step, in this chapter we present *charge shuttling* experiments, in which we shuttle the electron and only track its position, neglecting its spin state. For this type of measurements, chapter 4.4 will explain methods for optimising shuttling parameters with respect to the shuttling fidelity, which will be defined in chapter 4.3. The preceding chapters 4.1 and 4.2 explain the experimental setup and the measurement procedure. The data presented here were measured and analyzed together with Mats Volmer.

4.1 Experimental setup

The device used to perform all experiments in this chapter as well as in chapters 5 and 6 is an 8-dot SQS device with 17 individually controllable finger gates (and thus, as shown in figure 4.1). In contrast to the measurements at 4 K, here, both screening gates are separated and bonded individually to ensure full control over the electrostatic potential perpendicular to the channel. This will become important in chapter 6.4. Most of the channel gates are bonded together according to their gate set, as described in chapter 2.4.2. However, the first plunger as well as the first two barrier gates from each side are still connected individually. This ensures the possibility to form quantum dots from any direction. After cooling, we discovered that B8 was broken, preventing us from shuttling an electron through the entire device. Also, there is a major localization at about 1.3λ shuttle distance, which can be the reason for some experiments to fail at this point. All the gates sets, that form the middle of the device, as well as one adjacent barrier and plunger each are connected to bias tees on a PCB. More precisely, this is valid for the barrier gates B2 to B8 and plunger gates P1 to P9. In figure 4.1, these gates are shown in green. Connecting them to the bias tee is crucial to enable the fast control of these gates that we want to use for shuttling. The remaining gates are connected to a DecaDAC (further explained below). For the gates shown in red, an additional voltage adder is connected

in between. The green gates are also interconnected with the voltage adder through the corresponding DC line, enabling the DC AWG to apply the DC component of the pulses, a feature particularly crucial for extended pulses such as readout or charge scans. The

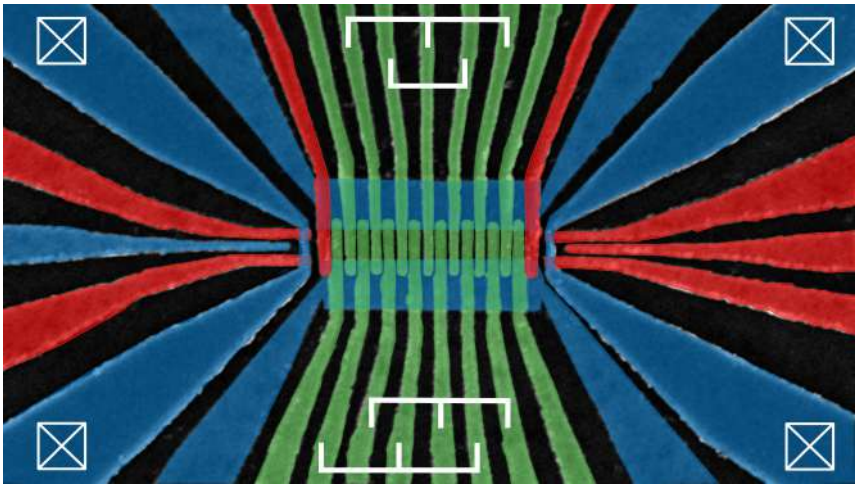

Figure 4.1: Gate layout of the device used at mK temperatures. The gates shown in green are connected to bias tees on the PCB. The gates shown in blue are directly connected from the breakout box to the DecaDAC while the gates in red are connected to an additional voltage adder. The white crosses roughly indicates the region the positions at the ohmic contacts are implanted. Gates connected within a gate set are highlighted by white lines.

full experimental setup including the electrical wiring and measurement instrumentation is shown in figure 4.2. The centerpiece of the setup is *Kurt*, an Oxford Triton 200 model dry dilution refrigerator that contains the sample discussed above. The in-build magnet can supply magnetic fields of up to $B_{\max} = 7\,\mathrm{T}$ and the base temperature of this dilution refrigerator is about 40 mK. The sample is mounted on a PCB. The PCB used here is different from the PCB used at 4 K and designed to fulfil the requirements of measurements at millikelvin temperatures. It hosts eight fast lines, numerous DC lines and a flatband connector, which connects it to two 24-line D-sub connectors via a flex PCB. The D-subs are connected to twisted pair Phosphor-Bronze loom, filtered by a cold filter with 10 kHz cutoff frequency. This cold filter sits on the mixing chamber (MC) plate. The eight fast gates or gate sets, separately depicted in figure 4.2, are each connected to a bias tee. These have a cutoff frequency of about 5.3 Hz. The bias tees have a radio frequency (RF) and a DC side, with the former being connected to coaxial cables and the latter to the flatband connector. The RF lines are then further attenuated by 3 dB on the cold plate, 6 dB on the still plate and 20 dB on the second stage (PT2) of the pulse tube cryocooler (PTC). Thus, these lines are attenuated by 29 dB in total. These eight RF lines are then directly connected to an eight-channel *arbitrary waveform generator* (AWG), more precisely a high-density AWG (HDAWG) by Zurich Instruments (ZI). Due to the attenuation on the RF lines, the ZI HDAWG can output a maximum RF amplitude of 192 mV. The remaining channels, the DC lines, lead to a 1:1 breakout box with BNC connector outputs. All gates colored red in figure 4.1 are further connected to an active gain voltage adder,

which itself is connected to two multiplexers (MUX). Each MUX connects to a 1:5 voltage divider and a subsequent voltage adder with the DAC channel and terminates at a second ZI HDAWG. The remaining gates at the voltage adder are directly connected to one of two 20-channel DecaDACs, which similar as in chapter 3.1 are to apply distinct voltages to a certain line and gate. The ohmic contacts that are needed to perform transport current measurements, indicated by the ⊠ symbol in figure 4.1, are each connected to a Basel Precision Instruments SP983-IF I to V converter. It is set to a gain of 10^8, includes a 30 kHz integrated low-pass filter and is used to guarantee a high ohmic impedance. In addition to that, a SR560 transimpedance amplifier with an integrated 10 kHz low-pass filter is used to decouple the ground. Its gain is set to 10. For the readout of the signal, we use a dedicated measurement PC with an Alazar ATS9440 digital acquisition card. [77]

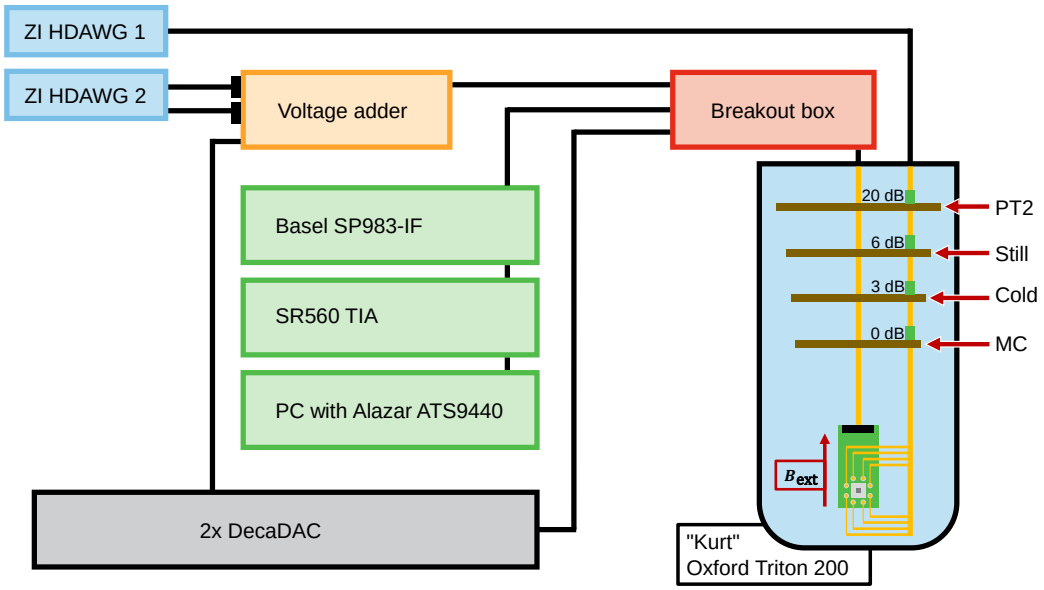

Figure 4.2: Sketch of the setup used for the experiments performed at mK temperatures. The cryostat "Kurt" is depicted with a schematic PCB inside. The direction of the magnetic field and the attenuation on each plate of the cryostat are depicted next to it. The black lines indicate cables connected to each measurement instument outside of the cryostat at room temperature.

4.2 Pulse sequence

Having the experiment fully set up, we can now discuss the first important series of experiments that need to be performed as preparation for coherent shuttling experiments, namely charge shuttling. This chapter discusses the pulses to be applied to perform such a charge shuttling experiment, which will also serve as basis for later experiments about coherent shuttling. As a typical pulse sequence consists of four pieces, we will discuss these pieces individually now. The pieces needed to perform charge shuttling experiments are:

1. *Loading* electrons into a quantum dot
2. *Initializing* a single electron by setting up an isolated system
3. Applying a sinusoidal *shuttle pulse* to the finger gates to shuttle the electron
4. *Readout* by measuring if an electron is close to the SET or not

In the end, all of those results will be combined into a single pulse, which is why the full pulse will be discussed after that. All of the processes described here refer to the left side of the SQS since this is the side that is completely usable. However, since the device is symmetric, all the processes could also be implemented from the other side by replacing B1 with B9, P1 with P8, and so on.

4.2.1 Loading electrons into a quantum dot

Before having loaded an electron into our first quantum dot, we have a potential that looks similar to the one sketched in dark blue in figure 4.3. The gray area on the left side here depicts the electron reservoir. By lowering the gate voltage on B1, we load four electrons to our QD. The potential during the loading process is shown in light blue. Notably, this process has to be compensated by also applying voltages to P1 and B2 as all of those gates have a non-negligible cross-talk. As B1 is 10 kHz lowpass-filtered, this process takes about 2 ms.

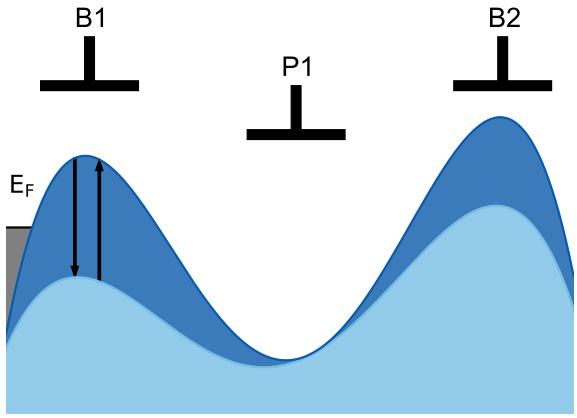

Figure 4.3: Sketch of the potentials under the first three channel gates during the loading process. We start the process in the dark blue potential, move to the light blue to load an electron and then go back to the dark blue to isolate it.

4.2.2 Initializing a single electron

After loading the electrons, we raise the barrier B1 again. This way, the system will be isolated. From this position, we can initialize a single electron into the second QD. A measurement showing these regions in charge occupation is shown in the charge scan in figure 4.4. The initialization mainly consists of two steps. First, we move the electron to

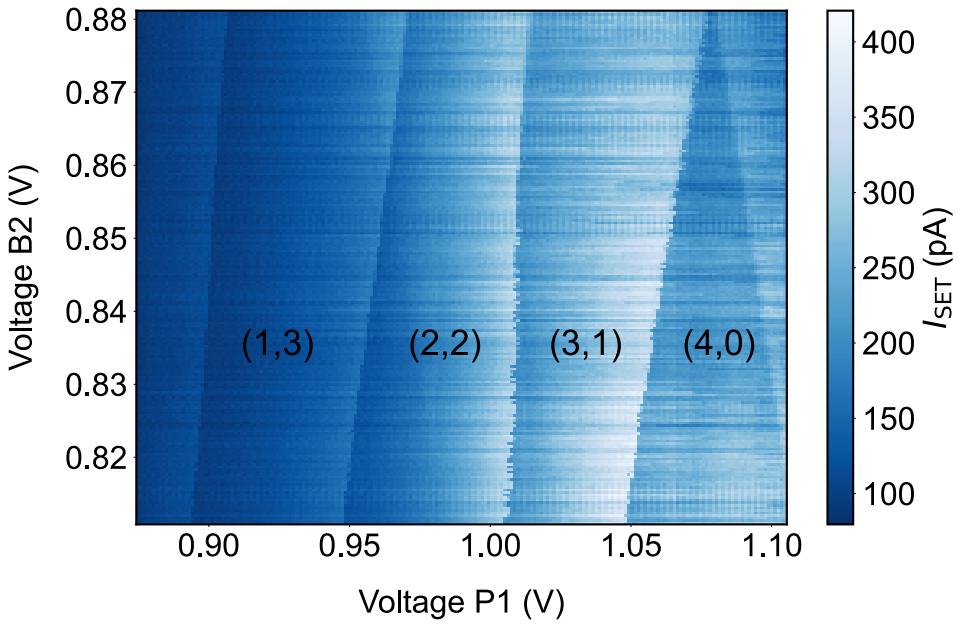

Figure 4.4: Charge scan with charge occupation regions important for the initialization of an electron.

the second QD by pulsing P1. Then we close the barrier B2 by 120 mV to isolate that single electron. At this stage, the electron is prepared for shuttling and the shuttle pulse can be applied. The potential and electron configuration after this step is shown in 4.5.

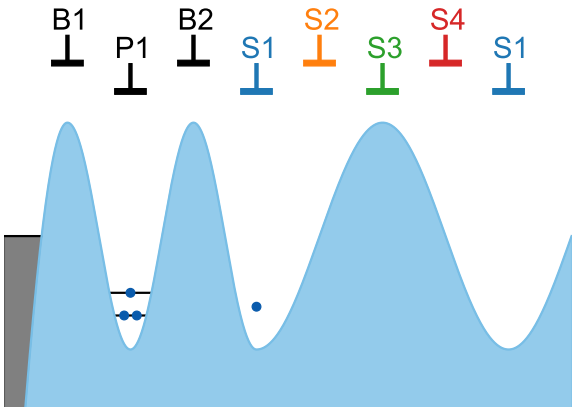

Figure 4.5: Sketch of the potential landscape under the first eight channel gates. The gray area shows the electron reservoir. Electrons are schematically depicted as blue dots. The black horizontal lines indicate the valley states. In the first dot, we load four electrons to overcome a potential uncertainty in valley state. As the electron in the second dot is completely isolated, we do not know in which valley state exactly it is, which is why the states are not shown here.

4.2.3 Shuttle pulse

To shuttle the electron, we apply a voltage

$$V_{\mathrm{S}i}(\tau_S) = U_i \sin\left(2\pi\tau_S + \varphi_i\right) + C_i \tag{4.2.1}$$

to each gate set Si with $i \in \{1, 2, 3, 4\}$. The amplitude U_i depends on the exact gate set as the gates were fabricated in different layers. The layers are offset by approximately 10 nm in the vertical direction. Due to this difference in spacing, we anticipate a reduced lever arm α for the higher gates, where α is defined by $E_i = \alpha U_i$. Thence, we define two values of the amplitudes, $U_{\mathrm{lower}} = U_1 = U_3 = 150\,\mathrm{mV}$ and $U_{\mathrm{upper}} = U_2 = U_4 = 192\,\mathrm{mV}$. Here, the index "lower" refers to the gates on the second layer, while "upper" describes gates on the third layer. We mostly express this voltage difference in terms of the amplitude scaling factor $\alpha = 1.28$ for which we get $U_{\mathrm{upper}} = \alpha U_{\mathrm{lower}}$. The compensation of the different gate layers is also important for the DC part C_i of the shuttle pulse. In a similar manner as before, we choose $C_{\mathrm{lower}} = C_1 = C_3 = 700\,\mathrm{mV}$ and $C_{\mathrm{upper}} = \alpha C_{\mathrm{lower}} = C_2 = C_4 = 896\,\mathrm{mV}$. These offsets serve to form a smooth DQD and DC potential, respectively. Lastly, the phase φ_i of the pulse is chosen such that we get a travelling wave potential through the 1DEC. More precisely, this yields

$$\varphi_i = (i-2)\frac{\pi}{2} \tag{4.2.2}$$

with $i \in \{1, 2, 3, 4\}$. A sketch of this pulse is shown in figure 4.6.

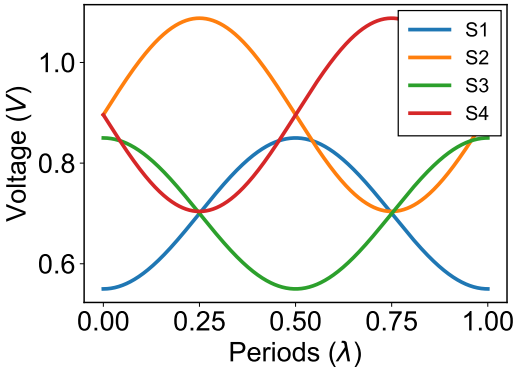

Figure 4.6: Part of the pulse that realizes shuttling of the electron. Each sine pulse corresponds to the voltage applied to one gate set.

4.2.4 Readout

For reading out if a charge is present or not, we use the SET as charge sensor. We exploit that the quantum dot formed in the SET, the *sensor dot*, is highly sensitive to local potential variations. After shuttling for one period, the electrostatic configuration of the gate voltages is exactly the same as before the shuttling process. Thus, when observing a different behaviour of the SET, we can draw conclusions to the number of electrons close to the SET. To optimally see differences in SET behaviour, we tune it to a sensitive position, such as the turning point of one of the SET peaks. Practically, this means that we can discriminate two different current levels when keeping the SET tuned at the same voltages. We identify one level with an electron being close and the other level with no electron in close proximity. These levels can be found by fitting Gaussian functions to the results of our single-shot measurements, as described in chapter 5.3, or in this case, knowing that we expect a high fidelity, roughly estimated by averaging over the currents in each measurement. A plot of the SET current with the Coulomb peaks visible is shown in figure 4.7. The point with the highest gradient on one of these peaks is the aforementioned turning point.

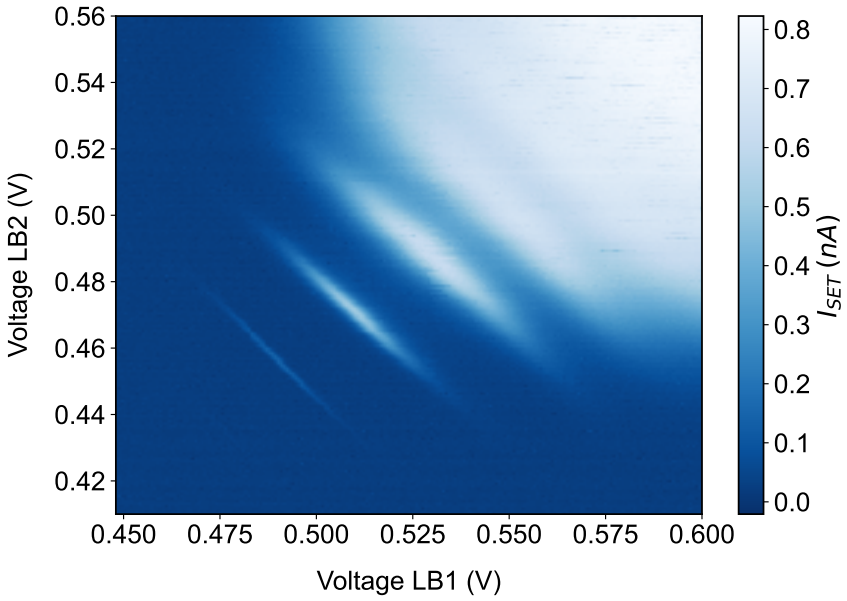

Figure 4.7: Barrier-barrier sweep of the left SET at millikelvin temperatures. The corner of the conductive region shows Coulomb oscillations.

4.2.5 Full pulse sequence

Plugging all of these parts together, a typical pulse sequence for charge shuttling experiments is shown in figure 4.8. This plot shows all the channels involved in a pulse sequence

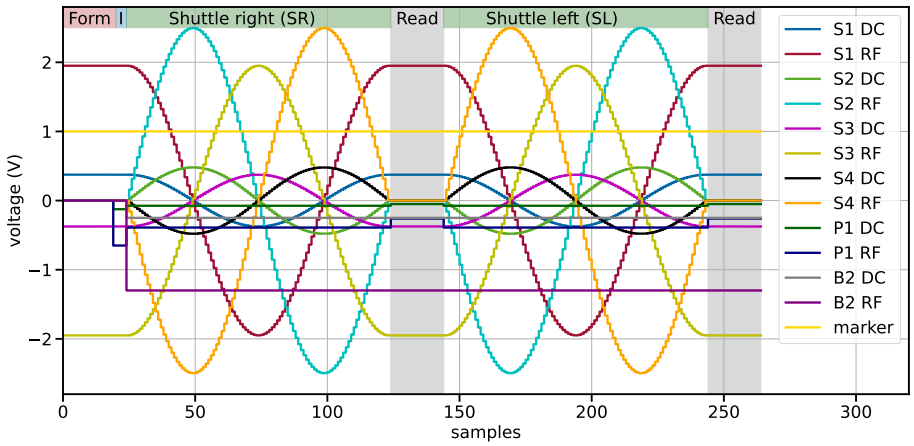

Figure 4.8: Full pulse sequence for charge shuttling experiments. The different steps (load, initialize, shuttle, measure) are labelled on top. Figure taken from [77].

and all steps from loading and initializing (I) the electron to two iterations of shuttling and measuring, here for- and backwards, for one period each. Remarkably, this full pulse sequence involves both constant voltages and sinusoidal voltages of very different values and on different timescales. This variety of voltages that has to be generated on different timescales poses a challenge to control hardware, which is often tailored for a narrow voltage range and pulses on a well-defined timescale.

4.3 Charge shuttling

With the pulse sequence mentioned in the previous chapter we can now load electrons into a quantum dot and shuttle them for- and backwards. Since the device used here does not allow for shuttling completely through the channel, we perform our experiments by shuttling the electron for a certain distance and then shuttling it back. To quantify this process, we introduce the charge shuttling fidelity $\mathcal{F}_C$. This fidelity can be computed by performing N_{total} charge shuttling experiments. In each experiment, we shuttle the electron one period ($\lambda = 280\,\text{nm}$) forward and perform a measurement. Then, we shuttle the electron one period back, and again perform a measurement. Since the SET as charge sensor only measures electrons in its close proximity, we expect to measure three electrons in the first measurement and four electrons in the second measurement of each repetition of the experiment. If we measure exactly this, we call an experiment successful, and we count the number of successful repetitions N_{success}. Now the charge shuttling fidelity can be defined as

$$\mathcal{F}_C = \frac{N_{\text{success}}}{N_{\text{total}}}. \tag{4.3.1}$$

An experiment can fail due to unforeseen tunneling events or other interactions in the shuttle device that would lead to two consecutive measurements in which we find either zero electrons or one electron. The raw data of an experiment used to determine the shuttle fidelity is shown in figure 4.9. When benchmarking the performance of a charge shuttling

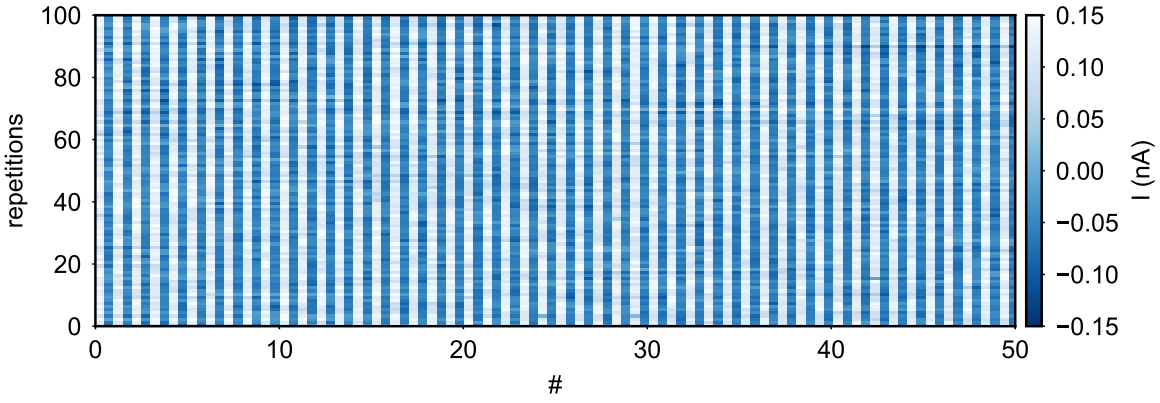

Figure 4.9: Raw data of a charge shuttling measurement. The plot shows 100 repetitions of 50 charge shuttling experiments, consisting of shuttling in, measuring, shuttling out, measuring. Each data point is one of the single shot measurements, each line is one repetition of the pulse. The data points show zero-centered currents I measured by the left SET.

experiment, there are three important parameters to consider. Firstly, we want to achieve high charge shuttling fidelities $\mathcal{F}_C$, since this quantity tells us how well our process and device actually works. Secondly, we want to increase the shuttle frequency f_S (and thus the speed of the electron) as much as possible. Even though theory suggests a velocity of about $10\,\text{m}\,\text{s}^{-1}$ to balance out nonadiabatic effects and usability, shuttling as fast as possible is desired because we want to perform as many operations as possible before our

qubit decoheres. Lastly, we want to decrease the shuttling amplitude A_S. This is because a higher amplitude corresponds to higher energies, which can easily lead to the device heating up. Also, a minimum amplitude is needed for shuttling to work. To quantify optimal parameter ranges, we can vary the shuttle amplitude and frequency and measure the charge shuttling fidelity for different values of these parameters. The corresponding plots are shown in figure 4.10 and figure 4.11. Regarding the shuttling frequency, analyzed

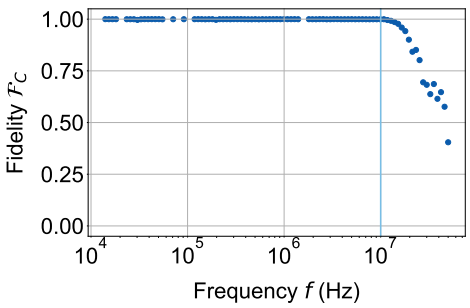

Figure 4.10: Charge shuttling fidelity $\mathcal{F}_C$ shown for different values of the shuttle pulse frequency f. The vertical line indicates the point at which the fidelity systematically starts to drop.

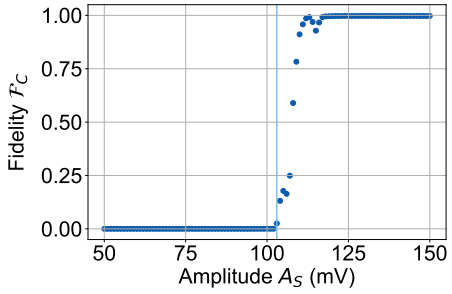

Figure 4.11: Charge shuttling fidelity $\mathcal{F}_C$ shown for different values of the shuttle pulse amplitude A_S on the lower layer gates. The vertical line indicates the point at which the fidelity systematically starts to rise.

in figure 4.10, one can clearly see that the charge shuttling fidelity is close to $\mathcal{F}_C = 1$ up to a frequency of $f_S \approx 10\,\text{MHz}$ after which we observe a continuous decline in fidelity. Translating this frequency into a velocity by calculating $v_S = \lambda f$, we reach a value of $v_{S,\text{max}} = 2.8\,\text{m}\,\text{s}^{-1}$. In a similar manner, we see a clear cut-off amplitude $A_{S,\text{min}}$, that is needed to shuttle electrons. Below $A_S = 100\,\text{mV}$, the shuttling fidelity is close to zero. For higher amplitudes, we see a steep rise in fidelity, that leads to a plateau of the fidelity close to $\mathcal{F}_C = 1$. We define the start of this plateau as our minimum amplitude, being $A_S = 125\,\text{mV}$. With these parameters, it is still possible to maintain the simple sinusoidal pulse sequence needed to perform shuttling processes. However, further decreasing the amplitude and increasing the frequency of the applied pulse is possible. Methods how to further optimize these parameters will be discussed in the following.

4.4 Parameter optimization

The decrease of charge shuttling fidelity $\mathcal{F}_C$ beyond certain threshold values of pulse amplitude and frequency is likely caused by imperfections in the device, such as broken gates, strong cross-coupling or impurities and defects in our heterostructure. The exact behaviour of an electron encountering the latter is subject of current research [94]. For now, it is only important that it results in the electron getting lost and thus a decrease of fidelity. To further investigate how to overcome these effects, we introduce the concepts

of *frequency tomography* and *amplitude tomography*. These are methods to find out how a minor modification of the pulse can lead to a significantly improved fidelity. With these tests, we want to investigate two things. Firstly, we want to find out if the reason for our electron being lost and fidelity dropping is of *local* nature. Secondly, we want to observe if the *direction* in which we shuttle has an influence on the fidelity. Consequently, we want to modify our pulse in a way that it contains local and directional differences compared to the standard pulse scheme.

4.4.1 Frequency tomography

As we found out before, there is a maximum frequency up to which charge shuttling with a high fidelity is possible. We can now test locality of the decrease in fidelity by increasing the frequency of the pulse only in a small window (here chosen to span 0.2 periods, as shown in figure 4.12. Now, the electron gets lost only if the position of this window matches the position of a defect or similar, as the rest of the pulse remained unchanged compared to the ideal, fully working case. Now, we can sweep the position of this window

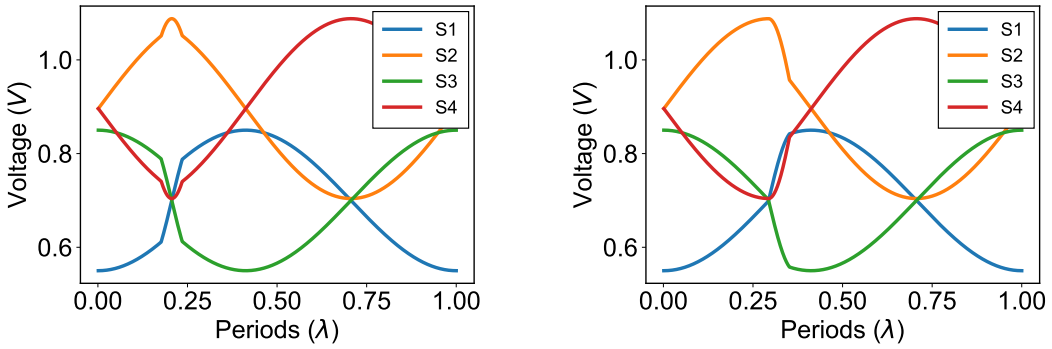

Figure 4.12: Altered shuttle pulse for frequency tomography measurements. The pulse now includes a window of higher frequency. (a) Window centered around 0.2λ. (b) Window centered around 0.3λ.

in the pulse. With this, we should get a full map of at which positions a higher frequency does not change the fidelity and at which position the fidelity drops because of the higher frequency. This map is shown in figure 4.13. Here, we see that only two points, $x_1 = 0.18$ and $x_2 = 0.68$ lead to a drop in fidelity. As these points are almost exactly half a period apart, it is likely that the fidelity drop is caused by a systematic induced by the periodic nature of the pulse and device. More importantly, this result means that, except for these two points and their surrounding area, we can apply a much higher frequency like 60 MHz and still maintain a near-perfect fidelity. We can extend this map and probe directionality by splitting it into two parts, one for shuttling forward, and one for shuttling backwards. These cases are shown in figures 4.14a and 4.14b, respectively. Interestingly, for shuttling

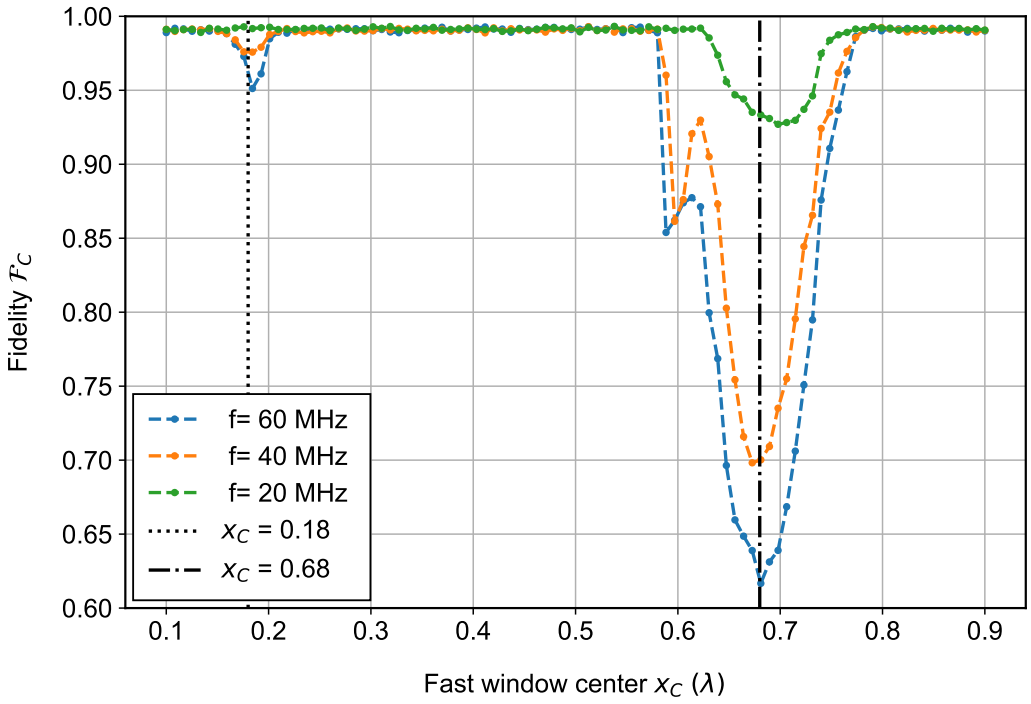

Figure 4.13: Frequency tomography results for different shuttle pulse frequencies above $10\,\mathrm{MHz}$. The charge fidelity $\mathcal{F}_C$ is shown for different central positions x_C of a small window of size 0.2λ in which the frequency is increased to one the values shown in the legend. Two dashed lines mark the center points of the two fidelity drops.

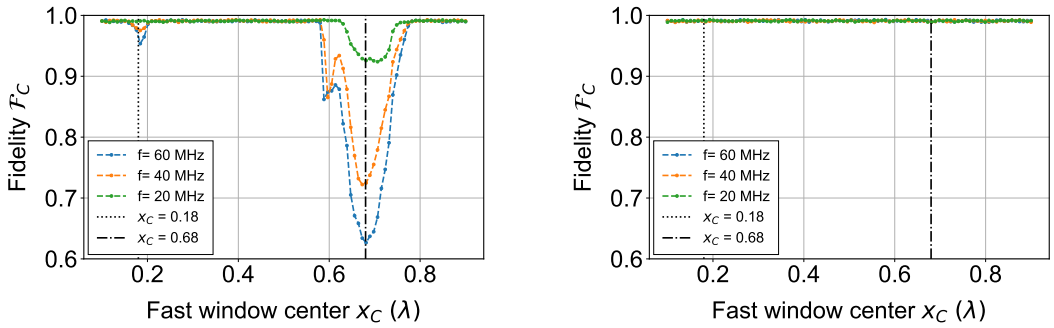

(a) **(b)**

Figure 4.14: Directional frequency tomography results for different shuttle pulse frequencies above $10\,\mathrm{MHz}$. The charge fidelity $\mathcal{F}_C$ is shown for different central positions x_C of a small window of size 0.2λ in which the frequency is increased either for shuttling in or for shuttling out as compared to one the values shown in the legend. Two dashed lines mark the center points of the two fidelity drops. (a) Frequency increased only for shuttling in. (b) Frequency increased only for shuttling out.

left, the plot looks almost exactly as the one in figure 4.13, while for the other direction, all tested shuttle frequencies show close-to-perfect behaviour. Thus we conclude that the fidelity drop is a directional effect and we have to decrease the frequency only in a small window on the way in if we want to shuttle faster than before.

4.4.2 Amplitude tomography

With the promising results obtained from the frequency tomography, it makes sense to repeat the same with varying the amplitude of our shuttle pulse instead of the frequency. For visualisation of what it looks like in this case, the changed pulse can be taken from figure 4.15. Here, we see that we decrease the amplitude in a small window. Again, we

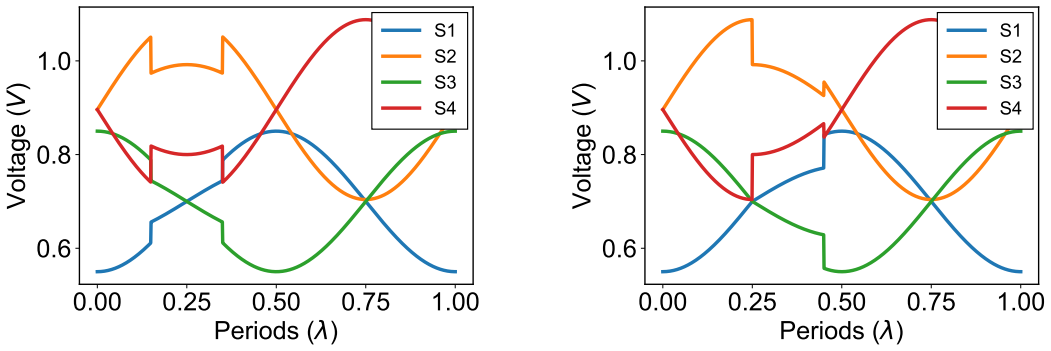

Figure 4.15: Altered shuttle pulse for amplitude tomography measurements. The pulse now includes a window of scaled amplitude. (a) Window centered around 0.25λ. (b) Window centered around 0.35λ.

can sweep the position of this window in the pulse to localize positions where potentially a higher amplitude is needed. The results of this sweep are shown in figure 4.16. It is evident that around $x_3 = 0.5$, the low amplitude is not sufficient to maintain high fidelity. Thus, we know that we can decrease the amplitude in all parts of the pulse, except for a small region around x_3, with the size of this region depending on the amplitude we want to use. Also, as shown in figures 4.17a and 4.17b, we can investigate how the direction of shuttling changes the outcome. While for half the initial amplitude, the fidelity drops at the same position for both directions, one can see that for shuttling backwards the fidelity already drops at an amplitude that corresponds to 70 % of the initial amplitude. As a result, we note that also the amplitude can be optimized by adjusting it based on direction and position in the shuttle device. As a final check of this method, we can also perform an *inverse amplitude tomography*. Instead of decreasing the amplitude in a small window, we decrease it everywhere except for a small window. The results of this measurement are plotted in figure 4.18. Here, we would expect a constantly high fidelity. However, we see that this only works down to a scaling factor of $\alpha_S = 0.8$. For an amplitude lower than that the fidelity significantly drops, for a scaling factor smaller than $\alpha_S = 0.75$ even to almost zero. It is also remarkable that when scaling down the amplitude by a factor of $\alpha_S = 0.35$, even in the region that maintains the standard, unscaled amplitude, the fidelity drops significantly. Consequently, we see that even though the general observation from the amplitude tomography is still valid, the decrease in amplitude must happen carefully as decreasing it for almost the full pulse influences the fidelity stronger than expected.

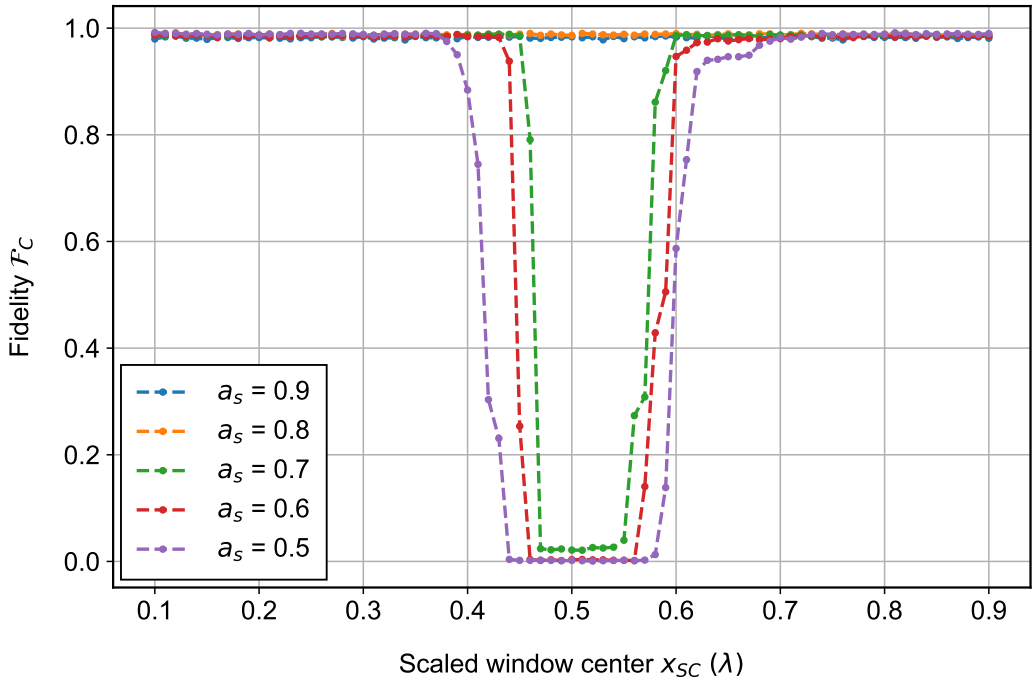

Figure 4.16: Amplitude tomography results for different shuttle pulse amplitudes. The charge fidelity $\mathcal{F}_C$ is shown for different central positions x_{SC} of a small window of size 0.2λ in which the amplitude is scaled by a factor a_S.

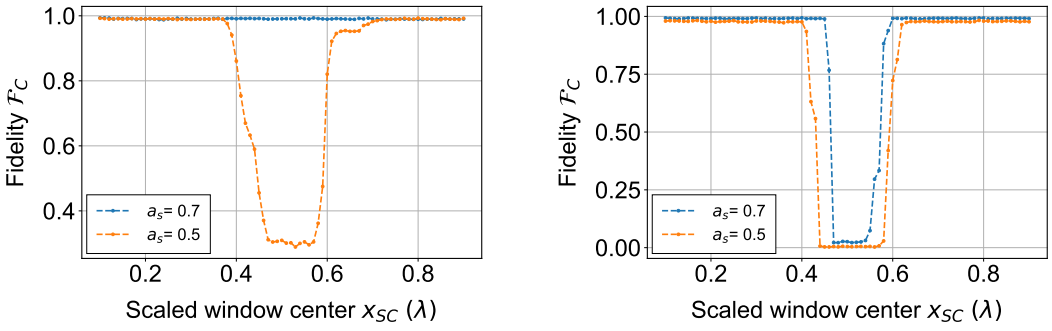

(a) **(b)**

Figure 4.17: Directional amplitude tomography results for different shuttle pulse amplitudes. The charge fidelity $\mathcal{F}_C$ is shown for different central positions x_{SC} of a small window of size 0.2λ in which the amplitude is scaled by a factor a_S, either for shuttling in or for shuttling out. (a) Amplitude scaled only for shuttling in. (b) Amplitude scaled only for shuttling out.

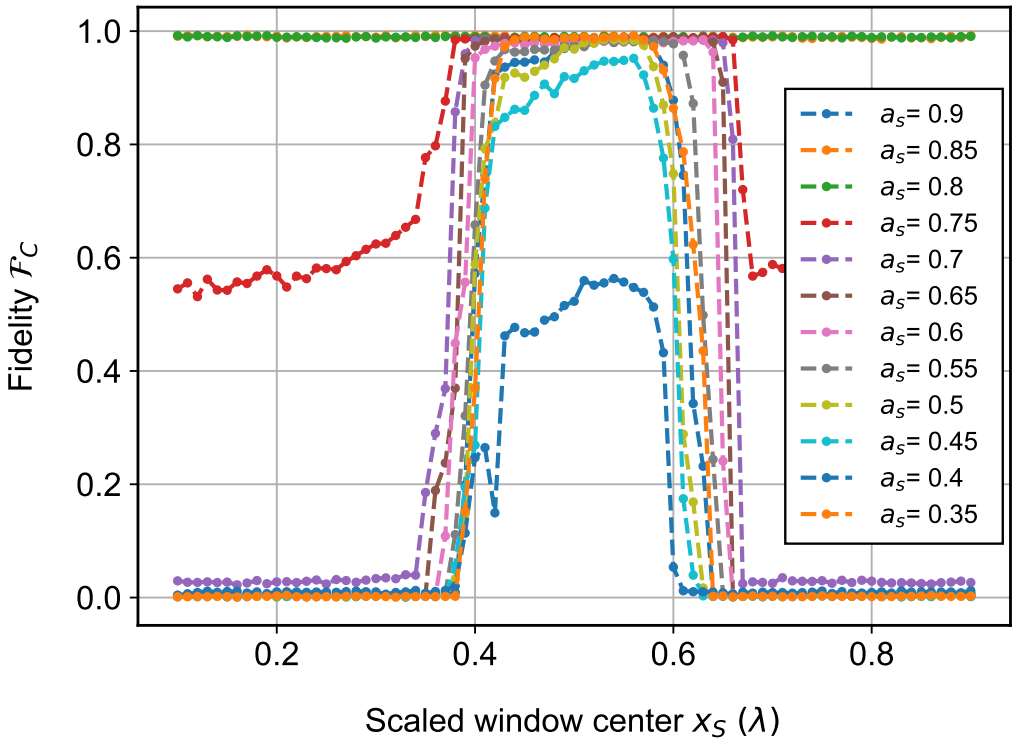

Figure 4.18: Inverse tomography results for different shuttle pulse amplitudes. The charge fidelity $\mathcal{F}_C$ is shown for different central positions x_{SC} of a small window of size 0.2λ in which the amplitude is *not* scaled by a factor a_S, meaning it is scaled by this factor everywhere else.

Chapter 5

Spin-coherent electron spin shuttling

In this chapter, the main findings regarding the spin-coherence of shuttled electrons will be discussed. For this, first, we will explain how the measurement procedure changes in comparison to the charge shuttling experiments described in chapter 4. Afterwards, we will introduce singlet-triplet (ST_0) oscillations and outline their importance as a measure of coherence. These oscillations were recorded for multiple shuttling distances, thus chapter 5.3 will deal with explaining the measurement and analysis procedure of the data. In the following, the oscillations will be further analyzed by evaluating their frequency and amplitude. Moreover, as the oscillations present are decaying, we analyze their decoherence time T_2^*. We will introduce the concept of motional narrowing (MN) and present different theories to explain the measured T_2^* times. Also, we will show an experiment that extends this recording of oscillation for far more than one period shuttle distance. That way, we derive hints on the maximum distance we can shuttle our electron and still preserve its spin state. We will finish off the chapter by showing further measurements that map the local g-factor landscape of the SQS as well as some experimental proof of entangled quantum dots.

The measurements described here were mainly conducted by Tom Struck, Lino Visser and Mats Volmer. The data analysis was mainly performed by me, with contributions from Tom Struck, Mats Volmer, Lino Visser, Łukasz Cywiński and Lars Schreiber.

Most of the measurements and results described in this chapter are summarized in the preprint of a paper titled "Spin-EPR-pair separation by conveyor-mode single electron shuttling in Si/SiGe" [67].

5.1 EPR pair initialization and Pauli spin blockade readout

Firstly, we will now describe the experimental procedure and compare it to the pulse sequence and the steps used for charge shuttling experiments. The overall structure of a shuttling experiment will stay the same. We load and initialize an electron, shuttle it forward, then backwards, and then measure. To probe the coherence of the electron, we want to initialize and separate an EPR pair. As a two-electron-system, we can operate it in the $\{|\uparrow\uparrow\rangle, |\uparrow\downarrow\rangle, |\downarrow\uparrow\rangle, |\downarrow\downarrow\rangle\}$-basis. Equivalently, we can also express the quantum mechanical

state of the EPR pair in the singlet-triplet basis $\{|S\rangle, |T_+\rangle, |T_0\rangle, |T_-\rangle\}$. Operating the SQS with an EPR pair instead of a normal electron unlocks the possibility to use Pauli spin blockade (PSB) readout, a method that maps a spin state to a charge configuration and thus making it measurable with the charge detection scheme explained in 4.2.4. Also, as we work with a two-electron-system now, we will always use the DQD notation (n_1, n_2) to express occupation numbers. That being clarified, in the following, the exact pulse sequence and readout techniques will be explained.

5.1.1 EPR pair initialization

We want to initialize the EPR pair in the $S(4,0)$ state, a singlet state with four electrons trapped in the first QD and no electrons in the second QD. We utilize four electrons to ensure that the lower valley state is occupied by a singlet comprising two electrons. While this can be disregarded during our experiments, it guarantees that, at least within the static dot, valley splitting doesn't lead to undesirable effects from a lone electron hopping between states. This initialization is achieved by first pulsing to the (4,0)-region, as indicated in figure 5.1. We wait at this stage for a time $\tau_I = 2\,\text{ms}$ to ensure that enough time has passed for the electrons to become entangled due to their exchange interaction as well as to relax to the $|S(4,0)\rangle$ state, which happens to be the ground state in this voltage configuration. Next, we want to separate the EPR pair and this way prepare a single electron in the second QD. Thus, we apply an additional voltage of $V_{P1} = 20\,\text{mV}$ to the first plunger gate P1. This way, we allow for one electron to adiabatically tunnel from the first to the second QD, moving to the (3,1)-region in figure 5.1. This way, the exchange interaction J is reduced while a g-factor difference Δg of the two electrons arises as the result of their lateral separation. This will become important for the dynamics of the system, as to be further described in chapter 5.2. The initialization is regarded as complete now, and all shuttling experiments explained in the following start from this point.

5.1.2 Pauli spin blockade

After having performed a shuttling experiment with the EPR pair, in the following step, we want to read out the spin state of our electron system. This is put into practice by employing *Pauli spin blockade* (PSB) based readout, a method of spin state to charge configuration conversion that will be described in the following. For this, first, we introduce the energy level diagram of a singlet-triplet-system in dependence of the detuning of the DQD, which is shown in figure 5.2. The detuning is defined as the difference in electrochemical potential of the two QDs, $\varepsilon = \mu_1 - \mu_2$. It is sketched in figure 5.3.

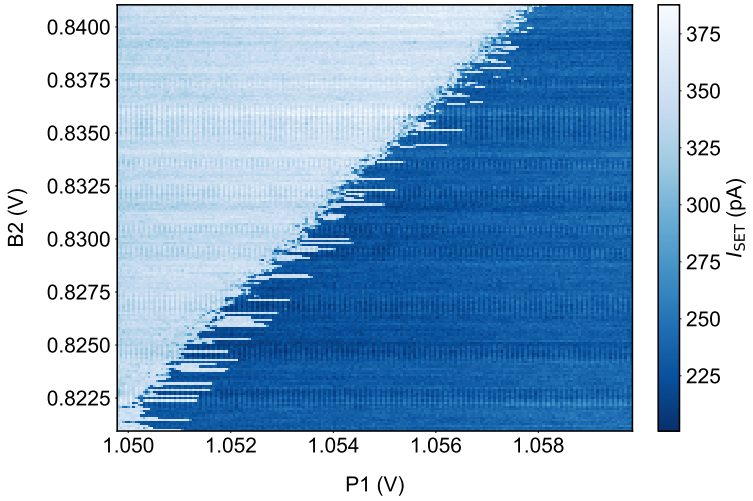

Figure 5.1: Charge scan of the PSB region in the closed system. It is obtained by measuring the SET current for a sweep of P1 against B2. The diagonal region in the middle is due to the PSB.

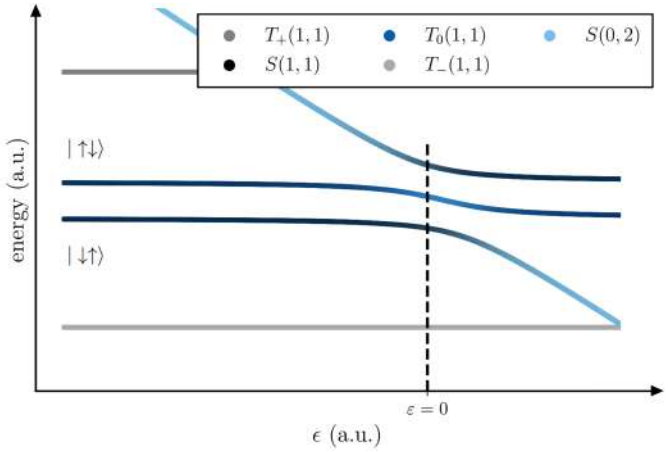

Figure 5.2: Energy levels of a singlet-triplet system in arbitrary units. The change in energy levels with the DQD detuning ε is shown. Plotting code (yet again angrily) provided by Max Oberländer.

In figure 5.2, we observe that the energy levels are strongly dependent on the detuning ε of the DQD. More specifically, it is important to note that the ground state occupation of our system can either be (4,0) or (3,1) depending on the detuning, which is why we want to change the detuning in the first place. For a distinct detuning, it can now happen that the (4,0) singlet state is energetically most favorable, but a transition from (3,1) state to (4,0) state is forbidden due to the Pauli exclusion principle. More precisely, a transition to the (4,0) state would mean that we have a spatial symmetry. This would require an asymmetric spin state to fulfill the Pauli exclusion principle. In the case our system is in a triplet state (3,1) with $|T_0\rangle \propto (|\uparrow\downarrow\rangle + |\downarrow\uparrow\rangle)$, it is also spin-symmetric. Thus, the single electron in the second QD cannot tunnel to the first quantum dot. This effect is what we call *Pauli spin blockade*. It is schematically shown in 5.3. As our SET that is used as a charge detector is sensitive to the difference between a (4,0) and a (3,1) state, measuring the charge close to the SET maps the spin-state of our EPR pair to a charge state. When

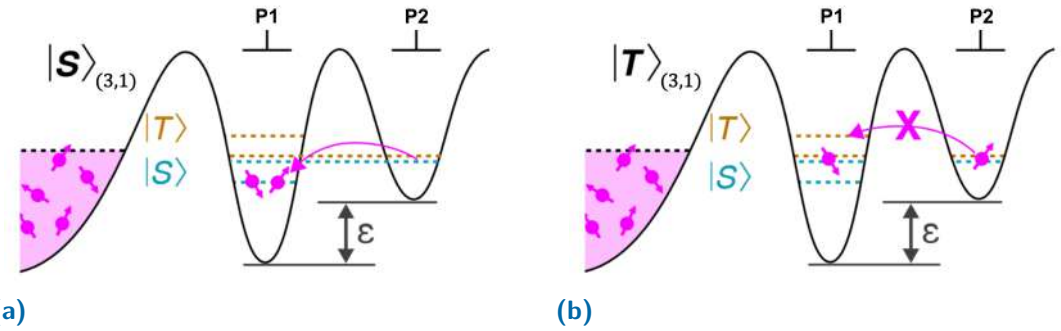

Figure 5.3: Sketch of the PSB based readout mechanism. (a) The EPR pair is in a singlet state, tunneling back to the first QD is possible. (b) The EPR pair is in a triplet state, tunneling back to the first QD is not possible. Figure adapted from [37].

wanting to practically measure PSB, we bring out system to the so-called *PSB region*. In a CSD sweep of the two gate voltages of a DQD, this is a trapezoidal region inside the (4,0) region at which the detuning has a value for which the PSB works. This region is indicated in figure 5.4. In this region, usually, the system would already be in the (4,0)

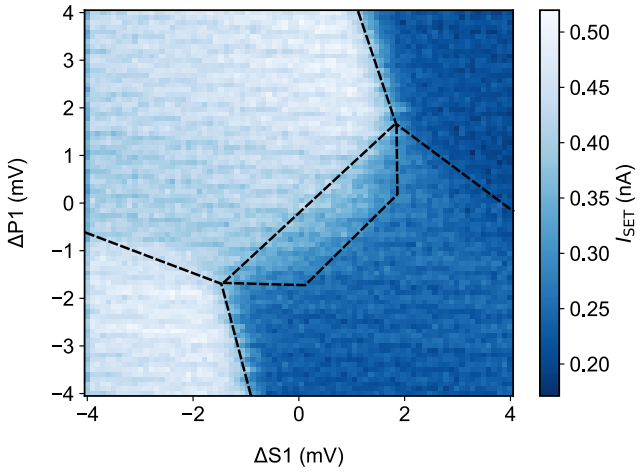

Figure 5.4: Charge scan showing the trapezoidal PSB region in an open system, indicated by dashed lines. The characteristic shape emerges due to the ground state changing with larger detuning. The region has an approximate width of 1 mV.

state, but as the transition to this state is blocked due to PSB, we see a higher current I_{SET} corresponding to the system still being in (3,1) state. Theoretically speaking, from figure 5.2, we would assume a triangular instead of a trapezoidal region here, because the detuning is changed by changes on both axes. But as for larger detunings ε the energy levels undergo a second anticrossing-like behaviour, the blockade only works for a limited range in ε. Thus, a small triangle is "cut off" from the expected triangular region, leaving a trapezoidal PSB region behind. In figure 5.4, this region has an approximate width of 1 mV. The trapezoidal shape comes from the energy states for higher detunings ε, which are not shown in figure 5.2. Due a generally similar behavior as for $\varepsilon = 0$, the ground state

changes, which leads to the tip of the triangular region being cut off. Having completed a shuttling experiment, we pulse to this region for approximately 500 ns, which is the time needed for the spin-to-charge conversion. After this, the interdot barrier is raised so that the charge state is "frozen" [95], regardless of PSB. That way, we have enough time to perform the actual measurement for readout.

5.2 Singlet-triplet oscillations

Next, we describe coherent singlet-triplet oscillations. These are oscillations on the Bloch sphere between spin-singlet state $|S\rangle$ and the unpolarized triplet state $|T_0\rangle$ which we use to quantify coherence, similar to the the oscillations sketched in figure 5.5.

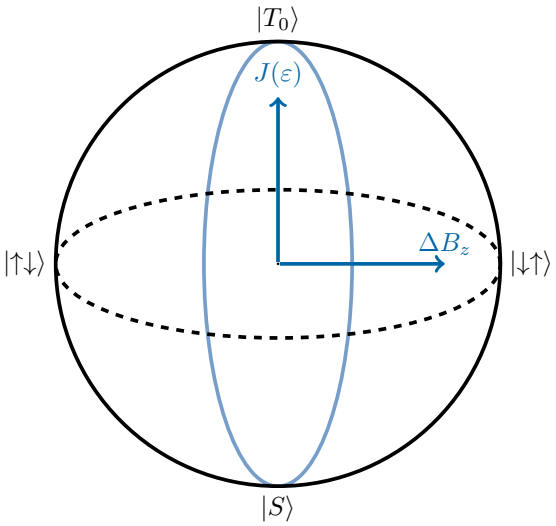

Figure 5.5: Sketch of a Bloch sphere of an EPR pair. The singlet-triplet oscillations are schematically shown in light blue. The dark blue arrows indicate the external magnetic field ΔB_z and the exchange interaction $J(\varepsilon)$ (which is zero for the oscillations depicted).

Mathematically, the EPR pair can be described by the Hamiltonian

$$H = \begin{pmatrix} -J(\varepsilon) & \frac{1}{2}(\Delta g \mu_B B + E_{\mathrm{hf}}) \\ \frac{1}{2}(\Delta g \mu_B B + E_{\mathrm{hf}}) & 0 \end{pmatrix} \tag{5.2.1}$$

expressed in the $\{|S\rangle, |T_0\rangle\}$-basis. Evidently, we ignore all effects of polarized triplet states $|T_\pm\rangle$ here, assuming the system can be controlled well enough to restrict only to these two states. The off-diagonal terms of this Hamiltonian drive oscillations between the two states. These terms contain the g-factor difference Δg, which is a result of lateral separation of the electrons as well as the external magnetic field B. Additionally, hyperfine interactions (hf) are expressed by the Overhauser energy difference E_{hf}. As said before, by applying the voltage $V_{P1} = 20\,\mathrm{mV}$ (which roughly corresponds to ε here) to the first plunger gate, we decrease $J(\varepsilon)$ and increase $\Delta g \mu_B B$. Thus, this detuning of the QDs

finally leads to a superposition of $|S\rangle$ and $|T_0\rangle$ states. With the nonzero magnetic field present and $\Delta g \neq 0$, the electrons also have different Zeeman energies. When now letting the system evolve freely, we observe oscillations between singlet and triplet state. An experimental realization of these oscillations can be seen in figure 5.6. These oscillations were measured in the DQD system without any shuttling involved.

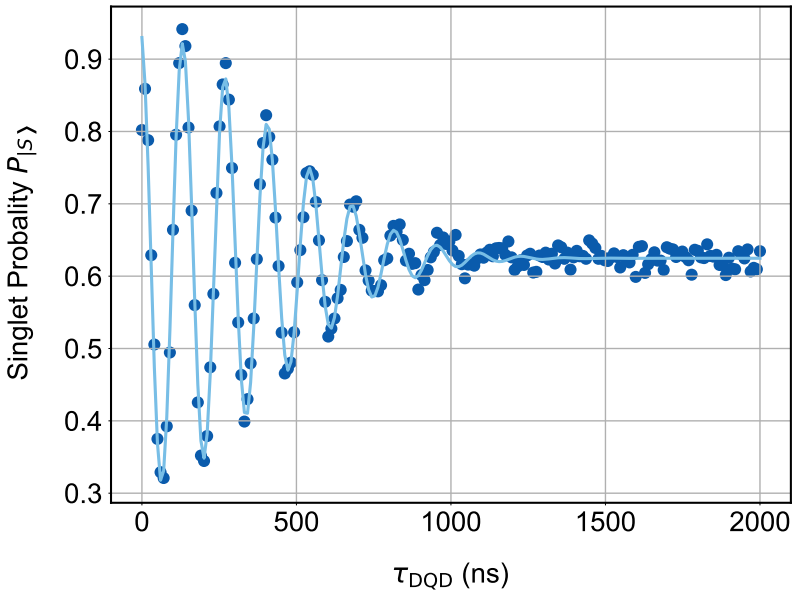

Figure 5.6: Singlet-triplet oscillations in a DQD system. A sinusoidal fit with a Gaussian decay is shown in light blue.

To further analyze these oscillations and extract parameters like the oscillation frequency ν, the amplitude A or the dephasing time T_2^*, we fit the function

$$P_{|S\rangle} = A\cos\left(2\pi\nu t + \varphi\right)\exp\left\{-\left(\frac{t}{T_2^*}\right)^2\right\} + P_0 \tag{5.2.2}$$

to the singlet probability $P_{|S\rangle}$, where φ is the phase of the oscillations, t the evolution time of the system, and P_0 an offset factor that centers the oscillations, in a perfect scenario, around $P_0 = 0.5$. As fit parameters, for this oscillation, the values described in table 5.1 were obtained. In the following experiments, we will continue using this formula or

Table 5.1: Fit values for the decaying sine describing ST_0 oscillations in a DQD system.

Parameter	Value
ν	(7.29 ± 0.01) MHz
T_2^*	(565 ± 10) ns
A	(31.4 ± 0.4) %

slight variations of it to quantify the parameters of the singlet-triplet-oscillations, as well as compare values for different shuttle distances with the values for zero distance (which is the DQD configuration) in table 5.1.

5.3 Spin-coherent shuttling

Having introduced how to initialize and readout the EPR pair as well as why ST_0-oscillations occur and how they are our main benchmark for coherence, we can now show measurement data and describe how to convert single-shot SET current measurements to parameters of ST_0-oscillations. All the data shown in this chapter were obtained by first loading and initializing an EPR pair. Then, after separating the EPR pair, one electron is shuttled in for a certain distance and immediately shuttled back out again. After this, a single-shot measurement using the PSB is performed. The dwell time of the electron in the SQS will be denoted as *shuttle time* τ_S. When recording the oscillations, as only single-shot measurements are possible, recording data points for a certain shuttle distance d for different time points is only possible by varying the shuttle velocity v_S depending on the time point to be taken. A typical data set for such a measurement is shown in figure 5.7. This data set features in total $200 \times 2000 = 400000$ single-shot measurements

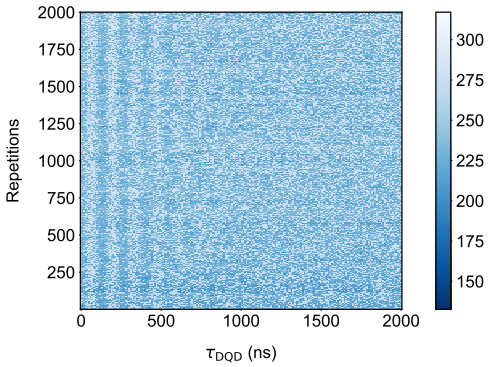

Figure 5.7: Raw data of a singlet-triplet oscillations measurement. The plot shows 200 time points. The pulse is repeated 2000 times.

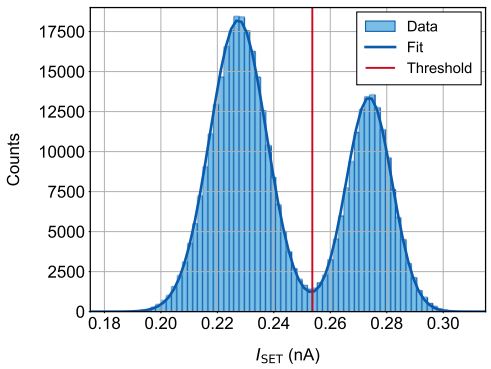

Figure 5.8: Histogram of all raw current data obtained in one measurement of singlet-triplet oscillations. Fitting a double Gaussian function (dark blue) to the histogram allows to find the readout threshold (red line).

in which the expected oscillations are faintly visible. To get these in a better resolution, we first need to find the *readout threshold*. This is a current threshold needed to classify our measurement results, which come in the form of SET current I_{SET} values, as the state of the EPR pair having been either $|S\rangle$ or $|T_0\rangle$. To find this threshold, we plot all the values from one data set in a histogram, as depicted in figure 5.8. We then fit a double Gaussian function

$$C(I_{\mathrm{SET}}) = A_1 \exp\left\{-\frac{(I_{\mathrm{SET}}-\mu_1)^2}{2\sigma_1^2}\right\} + A_2 \exp\left\{-\frac{(I_{\mathrm{SET}}-\mu_2)^2}{2\sigma_2^2}\right\}, \tag{5.3.1}$$

to this histogram, where C is the number of counts for each bin. For this fit, we first estimate the fit parameters by choosing A_i as maximum count number in the first $(i = 1)$

or second ($i = 2$) half of the data. Also, we estimate μ_i as the current corresponding to each of these aforementioned maximum count numbers. The standard deviation is estimated by

$$\sigma_i^2 = \frac{1}{N_{\mathrm{tot}}} \sum_{j=1}^{N_{\mathrm{tot}}} \left(I_{\mathrm{SET},j} - \frac{1}{N} \sum_{k=1}^{N} I_{\mathrm{SET},k} C_k \right)^2 , \tag{5.3.2}$$

with N_{tot} being the total number of counts and N the number of counts in each half of the data set.

Using these values as initial estimate for the fit function in equation 5.3.1, we can reliably fit a double Gaussian to the histogram. The readout threshold I_{th} will than be defined as the current corresponding to the minimal count number in the interval $[\mu_1, \mu_2]$. For all currents below this threshold, we have a comparably small sensor response, meaning that we measured more electrons close to the sensor. Thus, any current measured below I_{th} will be assigned to a $|S\rangle$ state. Vice versa, any current above I_{th} will be assigned to a $|T_0\rangle$ state. After converting all single-shot measurements from current values to quantum mechanical states, we also have to reshape each data set according to the number of repetitions of the whole oscillation measurement. Averaging over all these traces will then yield the actual singlet probability $P_{|S\rangle}$ for each point in time. This process is repeated each discrete shuttle distance d at which we performed the experiment. As a result, we get a map of ST_0 oscillations for different shuttle distances. Two examples of such a map for different external magnetic fields applied are shown in figure 5.9. Notable, to further

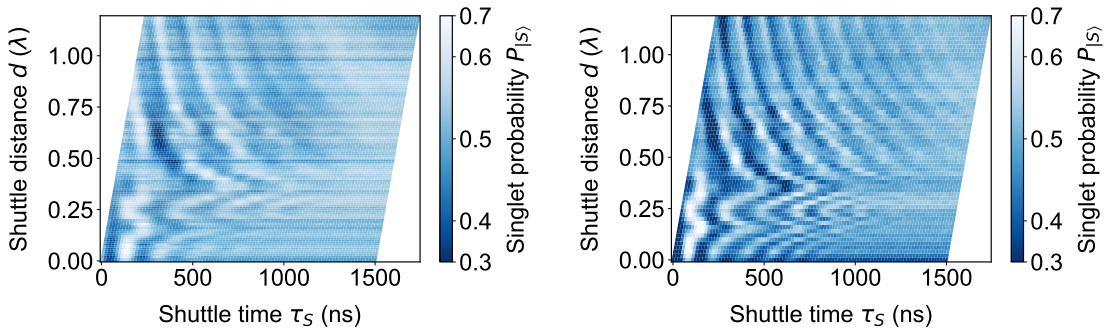

Figure 5.9: Maps of the singlet-triplet oscillations for different shuttle distances d. The white triangles emerge due to the limited shuttling speed. All other data points are obtained by varying the speed to get a certain nominal distance and time spend in the shuttle device. The colorbar shows the singlet probability. (a) Map for $B = 600\,\mathrm{mT}$. (b) Map for $B = 800\,\mathrm{mT}$.

increase resolution of these maps, several oscillation traces were recorded and averaged for each shuttle distance. Not visible here are the uncertainties for each data point, which will become important in a part of the analysis in chapter 5.5. These were estimated with the *standard error* (SE) for each individual trace.

When averaging multiple traces corresponding to the same shuttle distance, the uncertainties were combined by

$$\sigma_{\overline{\text{traces}}} = \sqrt{\frac{1}{\sum_{i=1}^{N_{\text{traces}}} \sigma_{\text{trace}}^2}}, \tag{5.3.3}$$

which is the *standard error of the weighted mean with inverse-variance weights.*
Coming back to the data presented in figure 5.9, we notice several things. Firstly, we see that even for shuttle distances of up to $d = 1.2\lambda$, where λ denotes that the distance is measured in units of the device periodicity, ST_0 oscillations are clearly visible and thus show that the shuttling process is coherent up to this distance. Increasing the distance further rapidly leads to the oscillations breaking down due to the already aforementioned localization. Secondly, these plots hint at the fact that these oscillations are caused and heavily influenced by the external magnetic field B_{ext}. This further means that the effect we observe here is indeed caused by a spin-dependent behaviour. Lastly, when trying to fit the function 5.2.2 describing the time-dependent probability of the ST_0-oscillations, we observed that most of the fits did not provide a satisfactory description of the measurement data, some fits even failed completely. Thus, the shuttling process seems to introduce additional effects influencing the exact shape of the oscillations. This is important for the next step, in which we try to fit a modified function to the raw data to extract parameters needed for a further investigation of the oscillations. In the first step, this modification consists of extending the fit function to a double cosine function

$$\begin{aligned} P_{|S\rangle} = (&A_< \cos\left(2\pi\nu_< \tau_S + \varphi_<\right) \\ &+ A_> \cos\left(2\pi\nu_> \tau_S + \varphi_>\right)) \exp\left\{-\left(\frac{t}{T_2^*}\right)^2\right\} + P_0 \end{aligned} \tag{5.3.4}$$

that keeps only one free parameter for the dephasing time while introducing a second amplitude A, frequency ν and phase φ. The indices $i \in \{<, >\}$ are chosen because we can always identify an upper ($i =>$) and lower ($i =<$) frequency. The amplitude and phase are classified by the frequency index in their corresponding cosine term and not by their value. With this fitting function, a sensible description of the measured data is possible. Two examples of such fits to the data in figure 5.9 are shown in figure 5.10. The analysis of how the fitting parameters change with other parameters such as the shuttle distance d will be conducted in the following chapters. For the remainder of this chapter, it is worth to note some practical considerations of these fits. Firstly, as again initial parameters for fitting need to be given to improve the convergence of the fit, these parameters must be somehow estimated. This estimation can be done by either extracting parameters from the Fourier transformation of the data or from first fitting a single sine function to the data and then again fitting a single sine function to the residuals of the first fit. While both methods generally work, the former has proven itself to be a bit more reliable. Also, the choice of the fitting function plays a role in how well the fit converges. While the commonly known `scipy.optimize.curve_fit` fitting function works in most

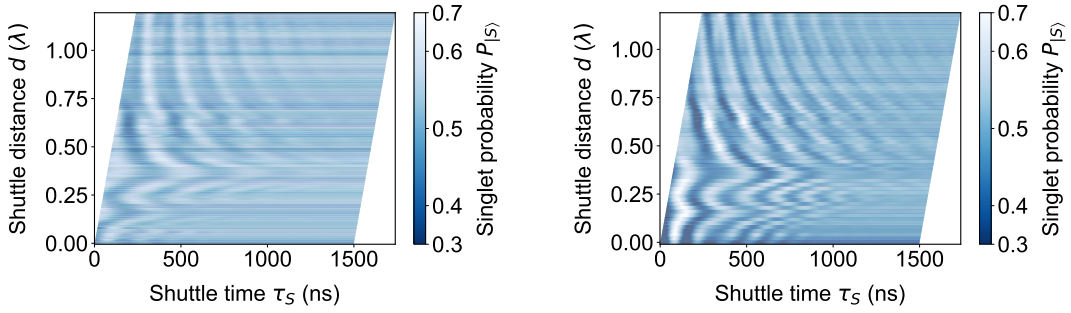

Figure 5.10: Fitted maps of the singlet-triplet oscillations. The data shown in figure 5.9 are fitted with a double sinusoidal function including a Gaussian decay. The fits are performed line wise. (a) Fit for $B = 600\,\mathrm{mT}$. (b) Fits for $B = 800\,\mathrm{mT}$.

cases, the `scipy.optimize.differential_evolution` function has often yielded better results. However, one should keep in mind that the latter function has some drawbacks. For example, it is not possible to propagate uncertainties of data points to those of fit parameters with this function.

5.4 Frequency and amplitude analysis

To continue the analysis of the experiments probing the spin-coherence of the electron, in this chapter, the frequency and amplitude of the ST_0-oscillations will be further investigated. To start off, we investigate how the two frequencies $\nu_<$ and $\nu_>$ change with the shuttle distance d. This relation is shown in figure 5.11. First, it is clearly evident that two frequency *branches*, an upper branch (index $>$) and a lower branch (index $<$) best describe the structure of the frequency points. Both branches have a similar shape, developing a peak and two valleys for small shuttle distances before continuously rising after. These features can also be found in the maps in the previous chapter, as in figure 5.9. With this clear distinction of two branches and working fits, the data present seem to be a good starting point for further comparing the frequencies in different branches and for different magnetic fields. However, some of the data points seem to be oddly shifted or out of place. As the approach of using two frequency components is of purely phenomenological nature, we can easily extend it to even more components and thus try to achieve a better understanding of the system. Before that, for the sake of completeness, the two-component analysis of the amplitude over shuttle distance is shown in figure 5.12. In contrast to the behaviour of the frequencies, it is remarkable that the amplitudes seem to be almost randomly distributed and not dependent on the shuttle distance d. Because of this, in the following, they will not be explicitly included in our analysis.

A reason for the differences and deviations in amplitude could be the sensitivity of the sensor during the measurement or other imperfections during the shuttling process. Thus, the frequency remains as the best parameter to analyze and to connect to the shuttle distance. Mathematically, the frequency can be expressed as

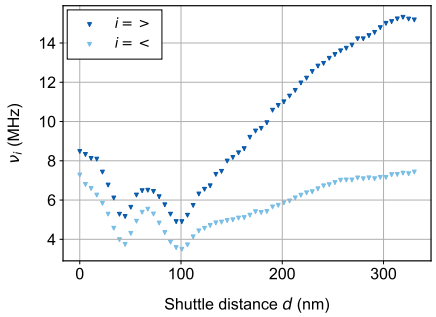

Figure 5.11: Frequencies extracted from the fit in figure 5.10 plotted for different shuttle distances d. Two distinct frequency branches are visible.

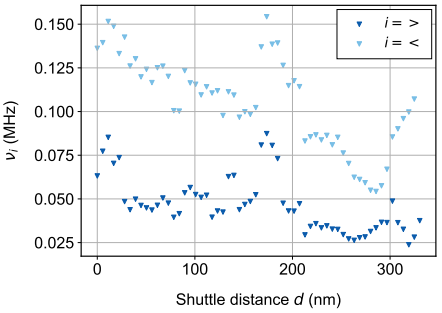

Figure 5.12: Amplitudes extracted from the fit in figure 5.10 plotted for different shuttle distances d. While the amplitudes are clearly separated, they do not show a smooth systematic behaviour.

$$\nu_i(d) = \frac{1}{hd}\int_0^d dx[\Delta g(x)\mu_B B + \Delta E_{\mathrm{hf}}(x)] \tag{5.4.1}$$

with h being the *Planck constant*. Further, this formula approximates $\partial_t \Delta E_{\mathrm{hf}} = \partial_t \Delta g = 0$, and thus neglects the time-dependence of these two parameters. Also, it assumes a deterministic and reproducible electron trajectory $x(t)$ in the SQS. As this formula generally describes the frequency as the result of a distance dependent integration, we would expect the course frequency to smooth out over distance. This is something we do indeed observe, for example in figure 5.11. Notably, as the physical origin of the arising of different branches is still subject of current research, this formula does not depend on the frequency branch i. Presumably the branches originate from initializing the system to a random spin-valley configuration. All of that being clarified, as a next step in the analysis, the frequency branches for one or different magnetic fields can be compared to gather more information about their origin and the behaviour of the oscillations. For this, in the following, we will first compare different branches to make a statement about the underlying mechanism leading to these oscillations. After this, we will conclude by showing *frequency correlation plots*, which again visualize the relation of different frequency branches in a different manner. Firstly, a straightforward comparison of branches by taking the ratio of two points for each shuttle distance is shown in figure 5.13. Both branches for both magnetic fields that were used are shown in figure 5.15.

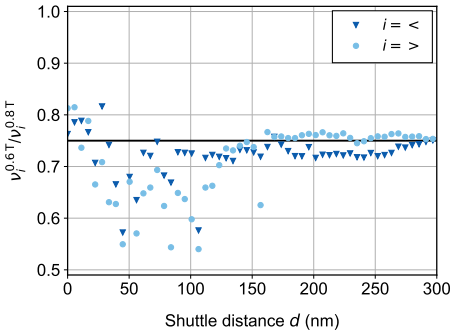

Figure 5.13: Ratio of frequency branches for different magnetic fields. For each ratio, upper (>) and lower (<) frequency branches have been evaluated separately. The horizontal line at a ratio of 3/4 shows the expected value for the magnetic fields in use.

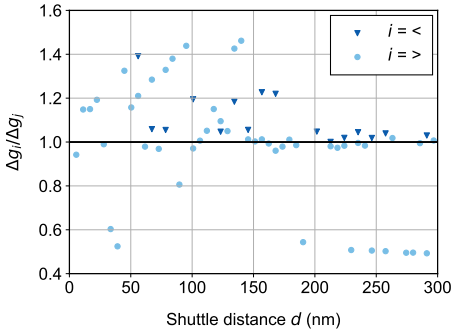

Figure 5.14: Ratio of g-factor differences for different magnetic fields. The black horizontal line at one indicates the expected value. For each ratio, upper (>) and lower (<) frequency branches have been evaluated separately.

For the comparison of different frequency branches of measurements with an external magnetic field of $B = 800\,\mathrm{mT}$ and $B = 600\,\mathrm{mT}$ show that the frequency ratio is remarkably close to $R_\nu = 600\,\mathrm{mT}/600\,\mathrm{mT} = 0.75$, which is the ratio of the external magnetic fields. This finding is reinforced by figure 5.14. Essentially, this figure shows the same data as figure 5.13, but converted the frequency to g-factor differences by calculating

$$\Delta g = \frac{h\nu}{\mu_B B}\,. \tag{5.4.2}$$

This representation also serves as normalization to the applied magnetic field, thus always expecting a ratio of $R_{\Delta g} = 1$. This way, it is even easier to see that the oscillations must originate from spin-dynamics of the system, as the linear dependence on the external magnetic field applied is strongly evident. Also, we conclude that the effect of the hyperfine interactions as described by ΔE_{hf} must be negligibly small.

Next, we want to investigate how different frequency branches relate to each other, both for different magnetic fields as well as for different frequency branches of the same magnetic field measured. This can be studied by plotting the *frequency correlation plot* (FCP), two examples of which are shown in figure 5.16. These plots always feature one of the frequency branches as each axis. Each data point corresponds to one value for the shuttle distance d. The color coding of the data points resembles the value of the shuttle distance, as indicated in the colorbar. This way, the correlation of two branches with rising shuttle distance can be investigated. Many interesting features are established by plotting the frequencies this way. Firstly, the plot is always divided by the angle bisecting line, indicated in black. All of the data points for two frequencies of the same magnetic field should be either above or below this line for each FCP as the branches were identified by sorting the frequencies according to their size. If the data points would cross this line, this would mean that the assignment of frequencies to branches has failed. However, data points sitting exactly

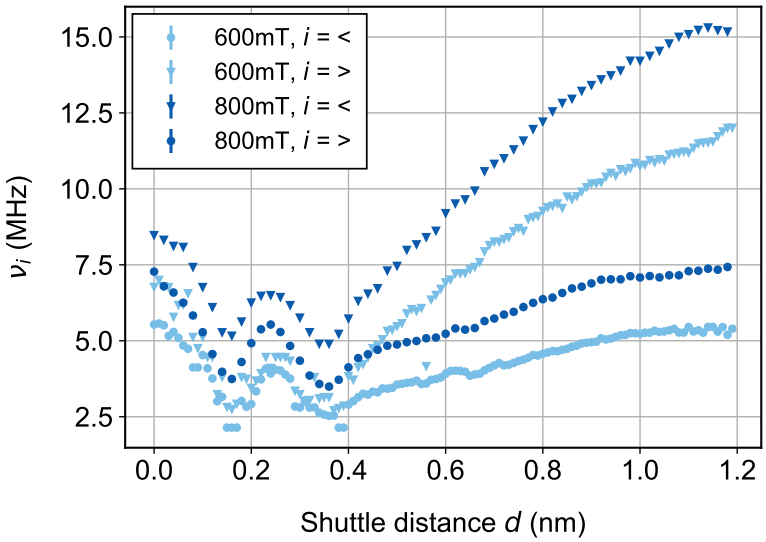

Figure 5.15: Both frequency branches for both magnetic fields in use plotted together.

on the angle bisecting line are allowed and not uncommon. For these points, the two compared frequencies are the same, meaning the two branches are degenerate. If the data points are aligned on a line parallel to the angle bisection line, the behaviour of the two frequency branches is the same and the frequencies are just offset by a frequency ν_o. If in addition to that, the frequencies are aligned on a line that is tilted in comparison to the angle bisection line, a scaling factor α_ν must be added. This means that the two frequency branches are either getting closer or diverge, depending on the value of α_ν. With these observations, we find that in figure 5.16, in both cases, the frequencies are both scaled and offset. For small distances, they tend to run together, while at some distance a turning point occurs, at which they diverge. This divergence is especially evident from the frequency over distance plots, as in figure 5.11. The occurrence of this turning point is a remarkable observation with no trivial interpretation. However, it strengthens the observation that for smaller shuttle distances, quite a lot of different effects and dynamics influence the system, while at some point, for larger distances, frequencies smooth out and the changes are very little.

5.5 Decoherence time T_2^* and motional narrowing

Now that frequency and amplitude of the ST_0 oscillations were sufficiently discussed, we come back to the observation that these oscillations are decaying. In equation 5.3.4, which was fitted to each trace of the oscillations, this decay is represented by the factor $\exp(-(t/T_2^*)^2)$. With the exponent being quadratic in time, we here have a so-called *Gaussian decay*, which will become important later. Similar as for the frequencies and amplitudes, the dephasing time T_2^* quantifying the strength of the decay can be presented

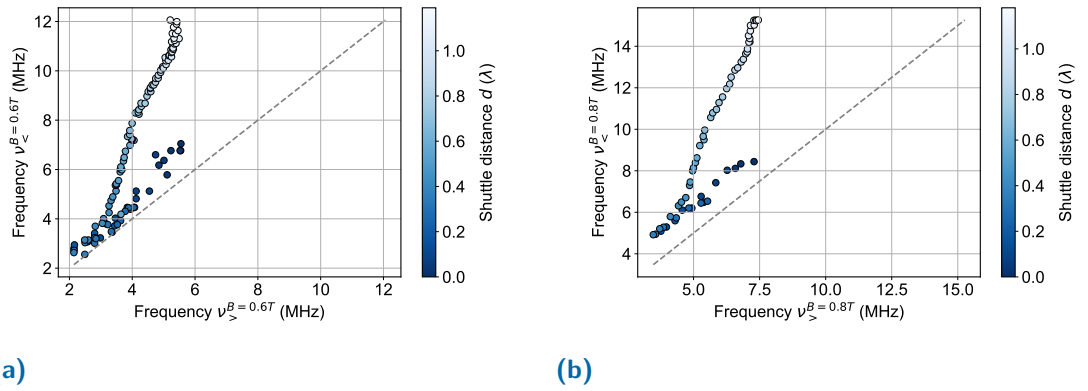

(a) **(b)**

Figure 5.16: Two examples of frequency correlation plots. One frequency branch from figure 5.15 each is plotted on the axes. The color of the dots indicates at which distance the two frequencies where measured. (a) FCP for $600\,\mathrm{mT}$, comparing lower and upper frequency branch. (b) FCP for $800\,\mathrm{mT}$, comparing lower and upper frequency branch.

in dependence of the shuttle distance d, as shown in figure 5.17. In addition to the T_2^* times for each distance, two different fits to the data are shown here. These will be further explained in a later part of these chapter and can be ignored for now. As mentioned in section 5.2, fitting equation 5.3.4 to the oscillations was practically performed using the `scipy.optimize.differential_evolution` function. As this does not return uncertainties of the fitted parameters due to its probabilistic nature, the uncertainties shown here had to be estimated otherwise. Thus, even though yielding worse results for the pure fits, the oscillations were additionally fit with the `scipy.optimize.curve_fit` function and the uncertainties were taken from the latter. As the fit is generally less precise, the uncertainties are a bit too large, and thus being sure not underestimate the uncertainties.

This is also why this method of extracting errors is valid in the first place. We observe that especially for small shuttle distances, the dephasing time seems to rise rapidly with the distance. As electron shuttling is known to open up new dephasing mechanisms [35], this strong improvement of dephasing time might seem surprising at first. The physical effect leading to this unintuitive results is called *motional narrowing* (MN) [35, 96]. This effect arises from the fact that for an electron in motion, the electronic environment is constantly changing. Thus, the dephasing induced by nearby nuclear spins does not always come from the same spin or same direction, but rather from different nuclear spins and other influences throughout the shuttle device. As a consequence, any additional phase or other types of dephasing picked up by the electron averages out the further the electron moves and the more different configurations of dephasing-inducing objects as nuclear spins or similar it sees. In a simple picture, one could for example imagine a free nuclear spin that is fixed in a certain distance to the electron. Due to this nuclear spin, the electron picks up an additional, unwanted phase factor. For a static electron, this would be a problem. Now that we can move the electron further, due to the assumed to be random nature of the distribution of such free nuclear spins, it is likely that the electron passes another free

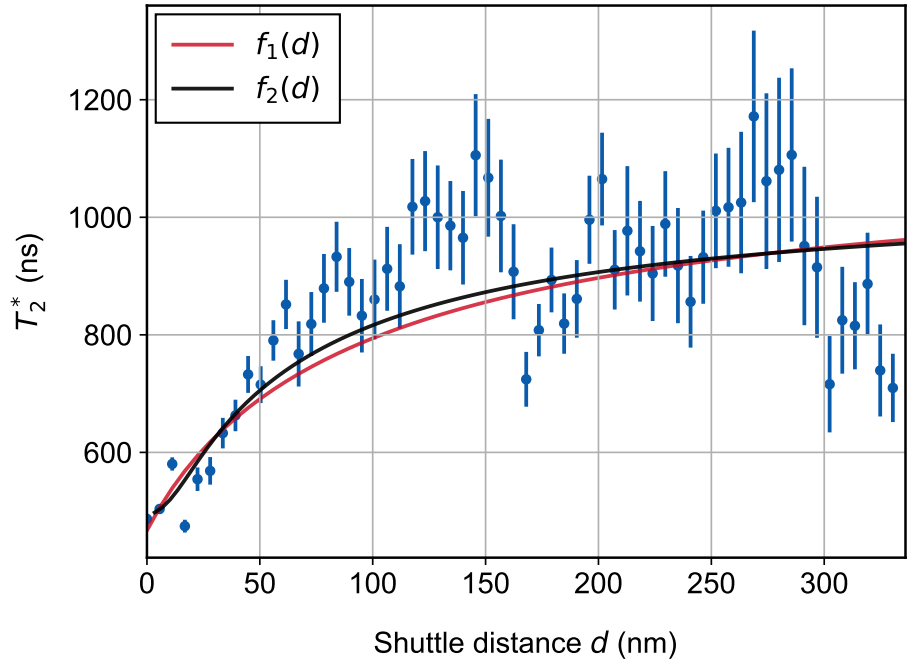

Figure 5.17: Dephasing time T_2^* (dark blue) plotted for different shuttle distances d. This exemplary data set was measured at a magnetic field of $800\,\mathrm{mT}$. Two different fitting functions (further explanations in the text) theoretically describing the motional narrowing effect are shown in red and black, respectively.

nuclear spin. This might be at the same distance as the first nuclear spin we imagined, just being in the opposite direction. Thus, it would lead to the same, unwanted phase factor being put up, but with the opposite sign. This means that both of these unwanted contributions cancel out each other and the state of the electron is exactly as we want it to be, with less decoherence introduced because of the electron motion. Scaling up this imagination to plenty of free nuclear spins at contrasting differences, orientations and positions, this averaging effect always takes place and is only dependent on the number of configurations the electron sees, which can be directly translated to the distance it is shuttled. After the region where the dephasing time undergoes this strong rise due to motional narrowing, it does only fluctuate strongly and does not change systematically anymore. Despite this being also predicted by different models for motional narrowing (see below), additional reasons not considered in the fit could be new decoherence channels opening up through the electron shuttling. This needs to be further investigated. Also, as this effect heavily relies on the electron passing through different spatial configurations of free nuclear magnetic spins, we expect it to be heavily suppressed for a device with a QW made of purified silicon and not natural silicon. The latter usually comes in a mix of several isotopes. In this mix, ^{28}Si is the most abundant isotope making up $92.23\,\%$ of natural silicon. Besides that, it is composed of $4.67\,\%\,^{29}$Si and $3.10\,\%\,^{30}$Si [45, 97]. All other isotopes of silicon are radioactive and not naturally occurring. From the previously listed

isotopes, only ^{29}Si has unpaired nuclear spins that can contribute to this mechanism. This means that for purified ^{28}Si, motional narrowing will not work as described here. However, since the nuclear spins induce most of the decoherence in the first place, it is still desirable to use devices fabricated with a ^{28}Si QW as the dephasing times will be significantly higher and thus making a mechanism such as MN unnecessary. Now that these details concerning the raw data points of the T_2^* time have been discussed, in a next step, we will come back to the fit functions used to describe motional narrowing. The first function, $f_1(d)$, is the result of a semi-phenomenological approach to motional narrowing, in which we modified a given theory for one moving electron in a quantum dot to our system of an EPR pair. For clarity, this formula can be rewritten as

$$\left(\frac{1}{f_1(d)}\right)^2 = \left(\frac{1}{T_2^*(d)}\right)^2 = \left(\frac{1}{T_{2,L}^*}\right)^2 + \left(\frac{1}{T_{2,R}^*}\right)^2 \frac{l_C}{d+l_C}, \tag{5.5.1}$$

where $T_{2,L}^*$ is the ensemble spin dephasing time of the left (and therefore static) QD, while $T_{2,R}^*$ resembles the same static dephasing time for the right QD. However, as this QD is shuttled, the contribution of this dephasing term is modified by a distance-dependant shuttling factor $l_C/(d+l_C)$, where l_C is the correlation length of the quasi-static noise of the shuttled dot due to its Zeeman energy. With this, we can identify

$$T_{2,S}^*(d) = T_{2,R}^* \sqrt{1+\frac{d}{l_C}} \tag{5.5.2}$$

as total dephasing time of moving QD. The general form of the two contributions from each QD being inverse squared added to get the inverse square of the total dephasing time is due to the Gaussian (and thus quadratic) nature of this decoherence mechanism. A more detailed motivation of the origin of this formula can be found in appendix C.1. A drawback of this formula is that it might not account for deformations of the QDs for very small shuttle distances, that can lead to further changes in spin dephasing time. Thus, we chose to also fit a second, more rigorously theoretically derived function to the data. This function is given by

$$\left(\frac{1}{f_2(d)}\right)^2 = \left(\frac{1}{T_2^*(d)}\right)^2 = \left(\frac{1}{T_{2,L}^*}\right)^2 + \left(\frac{1}{T_{2,S}^*(d)}\right)^2 \tag{5.5.3}$$

with

$$\left(\frac{1}{T_{2,S}^*(d)}\right)^2 = \left(\frac{1}{T_{2,R}^*}\right)^2 \left[\frac{2l_C^2}{d^2}(e^{-d^2/2l_C^2}-1) + \frac{\sqrt{2\pi}l_C}{d}\mathrm{Erf}\left(\frac{d}{\sqrt{2}l_C}\right)\right] \tag{5.5.4}$$

and it assumes constant shuttle velocity and no deformations in the shape of the right, moving QD. Further, only motional narrowing of E_{hf} is presumed. As before, a longer motivation of this formula is attached in the appendix C.2.

Notably, it is exceptional that both fitting functions yield very similar results despite of their fundamentally different derivation and approach to describe the system. As both also fit quite well to the data, each function can be seen as a cross-check that reinforces the validity of the other. For both fitting functions, we can now also try to estimate the shuttle fidelity for a coherent shuttling experiment. We define the fidelity $\mathcal{F}$ via the phase-infidelity of a Gaussian decay, which is given by

$$1 - \mathcal{F} = 1 - \exp\left\{-\left(\frac{\tau_S}{T^*_{2,S}}\right)^2\right\}. \tag{5.5.5}$$

We replace $\tau_S = 2d/v_{\max}$, as we shuttle in *and* out (leading to the factor two) with maximum velocity. Now that we can evaluate the fidelity at a certain distance d, a reasonable choice here is a distance of 1λ, thus evaluating the fidelity similar to the charge shuttling fidelity $\mathcal{F}_C$. As for this distance $2d \ll v_{\max} T^*_{2,S}$ approximately holds, we can Taylor expand the exponential ($e^x \approx 1 + x$) leading to

$$\mathcal{F} = 1 - \left(\frac{2d}{v_{\max} T^*_{2,S}}\right)^2 \tag{5.5.6}$$

as easy and fast approximation for the coherent shuttling fidelity. As we use the value of the fitting functions $f_i(d = 1\lambda)$ to find $T^*_{2,S}$, we get two different fidelity estimations depending on which function we use. With a distance of $2d = 2\hat{\text{I}}\check{} = 560\,\text{nm}$, we obtain a coherent shuttling fidelity of $\mathcal{F}_1 = 99.34\% \pm 0.17\%$ for the first fitting function $f_1(d)$ while we get $\mathcal{F}_2 = 99.12\% \pm 0.18\%$ fidelity for the second fitting function $f_2(d)$. These values match within their 1σ error ranges, making both values compatible with each other as well as more reliable.

5.6 Accumulated distance measurements

Knowing that we can shuttle electrons coherently can be seen as important proof-of-principle, however this is the first step towards a truly scalable architecture as described in chapter 2.3. For such an architecture, we need to be able to shuttle electrons coherently for distances of about 10 µm, and not just for $\mathcal{O}(100\,\text{nm})$. Consequently, we want to try shuttle experiments with a longer total nominal distance shuttled to evaluate how close we are to shuttling over these distances. As our device is limited in length as well as by the broken gate and defect-like localization, the only way left to shuttle over a distance as large as possible is to shuttle back and forth multiple times and only performing a measurement after all these shuttle steps. The total distance shuttled in this process is called *accumulated shuttle distance* D. The ST_0-oscillations for various values of D are shown in figure 5.18. Contrary to the previous section, we only evaluated this measurement for distinct values of D. Thus, it is more convenient to show the data in form of a waterfall

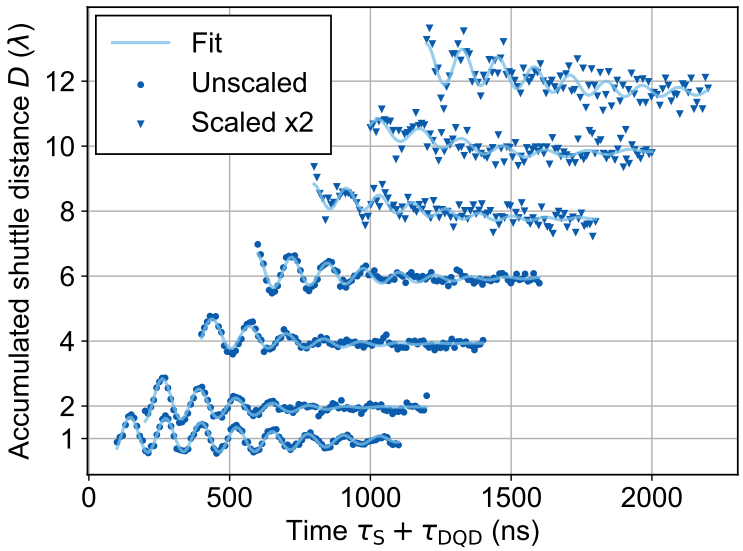

Figure 5.18: Waterfall plot of singlet-triplet oscillations for different accumulated shuttle distances D. The data for $D = 8$, $D = 10$ and $D = 12$ is scaled by a factor of two for better visibility. All other amplitudes are comparable in scale. The offset in x-direction is due to the limit in maximum shuttle velocity.

plot. This means that although the y-axis shows the value of D in the first place, the singlet probability is still encoded in the distance of each data point from the gray line. Also, the scaling of all oscillations is the same, unless otherwise indicated. This makes the oscillations still comparable. One thing to note is that for $D = 1$ we shuttled half a period in and half a period out again. Otherwise, also for similar experiments, values for $D < 2$ or $D \notin 2\mathbb{N}$ would not be sensible. The time scale in this figure is the time needed to shuttle back and forth multiple times, τ_S, added to the time we spend in the DQD configuration, τ_{DQD}, so in total $\tau_{S,DQD} = \tau_S + \tau_{DQD}$. It is evident that ST_0-oscillations are visible up to an accumulated distance of 3.36 µm, which underlines that generally, we are able to coherently shuttle for up to that distance. We again fitted these data points with the function using two frequency parameters, equation 5.3.4. As we do not plan to further investigate these parameters, this fitting formula is sufficient to describe the general trend of the data. The plot shows that even though we can observe ST_0 oscillations for increasing values of D, both amplitude A and decoherence time T_2^* strongly decrease with a much larger distance, making the coherence overall worse than for small distances. However, in a fully working device and with some optimization of the employed pulse sequence, it is likely that these values can be further optimized and full coherence can be established.

5.7 Wait time measurements

With only a small change to the measurement procedure, a very similar experiment as the ones described in the previous chapters can yield completely different results and open up a new way of understanding properties of the heterostructure. One such kind of an experiment will be explained in this chapter. In contrary to the previous experiments, we now do not want to quantify coherence, but rather map local variations of ν. These variations are directly related to local variations of the g-factor, so that we can use the now to be presented method to create a map of features throughout the channel of the SQS. We change mainly two things as compared to the coherent shuttling experiments in chapter 5.3:

1. We always shuttle with the maximum velocity for which coherent shuttling has worked, $v_{\mathrm{max}} = 2.8\,\mathrm{m\,s^{-1}}$.

2. In between of shuttling in and out, we wait at a certain position in the SQS for a time τ_W.

Thus, we make use of exactly the same mechanisms we can overcome by MN. As we wait at only one position in the SQS for a comparably long time and try to pass by all other possible positions as quickly as possible, the phase and decoherence being picked up during the experiment will be strongly dependent on the local environment of that one position we shuttle to. Consequently, repeating this process for various positions and again recording ST_0-oscillations for all of them, we gather information about each individual point in the device. Another way to phrase it is that by waiting at one point instead of continuously shuttling through the device, we get rid of the smoothing effect due to the integration over distance as described by equation 5.4.1. Besides that, the general methodology of initialization and readout as well as the overall measurement procedure stays the same, so that the data we get are in a similar format as in figure 5.9. The raw data of such an experiment for two different external magnetic fields applied are presented in figure 5.19. When comparing these maps with the conventional coherent shuttling experiments as in figure 5.9, it is evident on the first sight that the maps shown here seem to be way more chaotic. More irregularities in the oscillations as well as jumps to other frequencies happen at various positions. As we do not have a smoothing effect due to evenly distributed shuttling over different configurations of the environment, this does not come unexpected. A further analysis of these data can also be conducted similar to the analysis in chapter 5.4. First, in figures 5.20, we again show a double-sinusoidal function with a Gaussian decay (as in eq. 5.3.4) fitted to each individual trace. Even though the procedure here is the same as presented in figure 5.10, these plots are worth showing as they underline that a large variety of ST_0-oscillations can be fitted with this kind of function, underlining its general validity. Again in the same manner as before, we can extract the frequencies plotted against the shuttle distance d. These are depicted

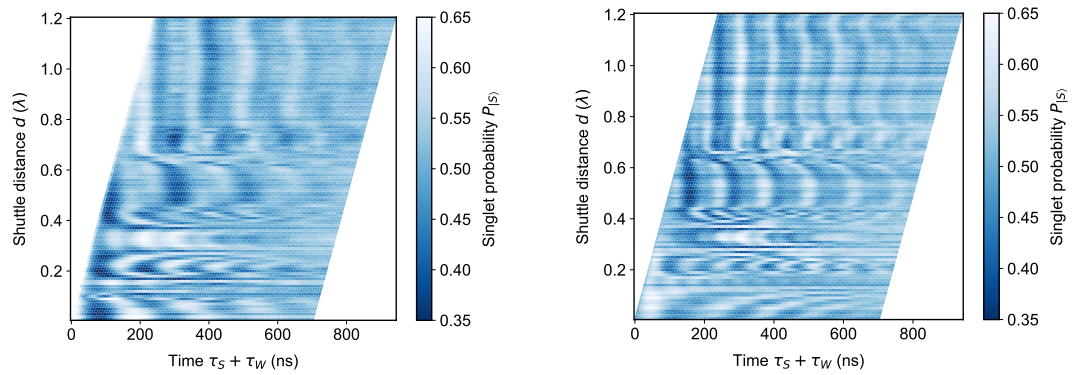

Figure 5.19: Singlet-triplet oscillation maps for g-factor landscape mapping. The electron rests at a distinct point in the SQS for a wait time τ_W. (a) Map for $B = 500\,\mathrm{mT}$. (b) Map for $B = 800\,\mathrm{mT}$.

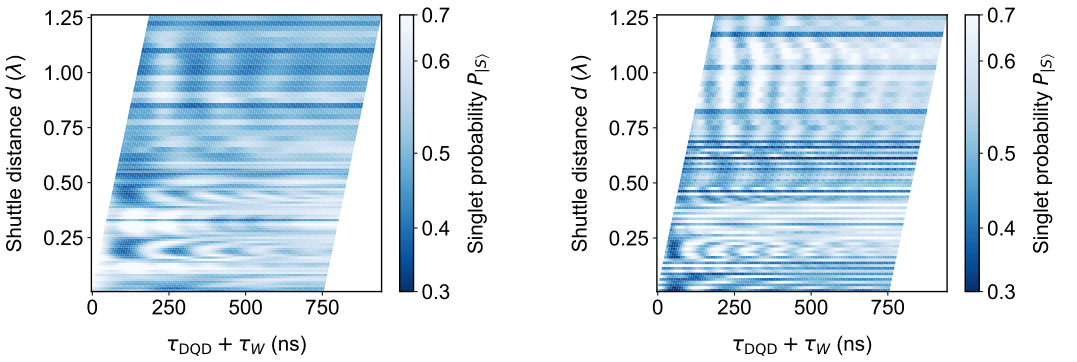

Figure 5.20: Fits to the singlet-triplet oscillation maps for the mapping of the g-factor landscape. The plots result from line wise fitting of a double sine function with Gaussian decay to the data shown in figure 5.19. (a) Fits for $B = 600\,\mathrm{mT}$. (b) Fits for $B = 800\,\mathrm{mT}$.

in figure 5.21, whereas the exctracted amplitude values are shown in figure 5.22. Most importantly, we again note that the pattern and the course of the frequencies shown here is way more chaotic as in figure 5.11. This is also why we do not extend this analysis to a quadruple sine fit, as already frequencies quite often reach values close to zero or behave in an otherwise unpredictable manner. However, it is remarkable that we still observe some continuous features as arcs or similar in this frequency structure, hinting at some larger-scale characteristics in certain regions of the SQS. These characteristics can be brought in to explain results of other experiments. An example for this is the more chaotic behaviour at the beginning of the shuttle device, which is also resembled by the results of these measurements. From these measurements, we can conclude that they are result of strong local g-factor variations and not physical effects of the EPR pair.

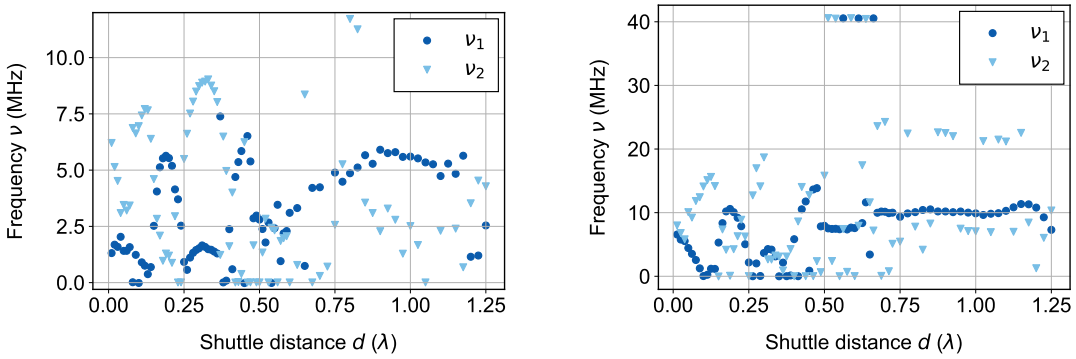

Figure 5.21: Frequency analysis of the previously fit data. The frequency ν_i is here the first or second fitted frequency, and not sorted by size.

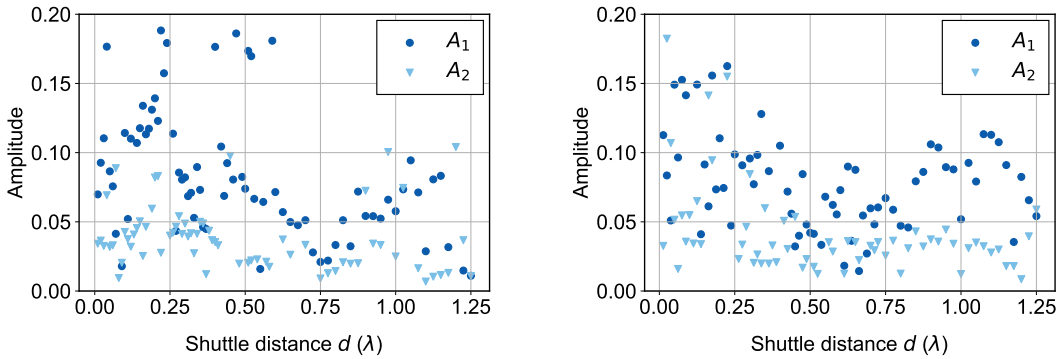

Figure 5.22: Amplitude analysis of the previously fit data. The amplitude A_i is here the first or second fitted amplitude, and not anyhow related to the frequency.

5.8 Squeezing the dot

As an important last part of this chapter about coherent shuttling experiments, we have to perform one last experiment that is crucial to validate previous experiments. This is because it is a realistic possibility that the EPR pair becomes disentangled when the right, shuttled dot is far enough away from the left, static dot. In the same manner, when shuttling back the dots could become entangled again due to the exchange interaction being present. The final result of the experiment could thus look exactly the same even if the two dots were not entangled (as they should be) for a majority of the time. As we cannot shuttle through the whole device and therefore always have to shuttle back to read out the state of the shuttled electron, we must find another way to prove that the two electrons are entangled for the whole course of the experiment. To prove this, we essentially repeat the aforementioned experiment in which we shuttle in, wait for some

time in the device, shuttle out again and probe coherence. However, during that time in which we wait and the right dot rests at some position in the device, we manipulate the left, static dot. This dot will be squeezed, meaning that we apply an additional voltage $B2^{\text{squeeze}}$ on the second barrier gate B2, slightly modifying the shape of this dot. Shortly after, we bring B2 back to the voltage where it was before. In a case of disentangled electrons, this should not do anything to the electron in the second, moving QD. On the other hand, in case of the two electrons still being entangled, we expect to measure a slight difference in the oscillation frequency ν when squeezing the dot. Moreover, we expect this difference to scale with the voltage applied during squeezing. Consequently, it is logical to plot the oscillation for a distinct, fixed shuttle distance and with varying *squeezing voltage* $B2^{\text{squeeze}}$ on one axis. This plot is presented as figure 5.23. Evident from this data is

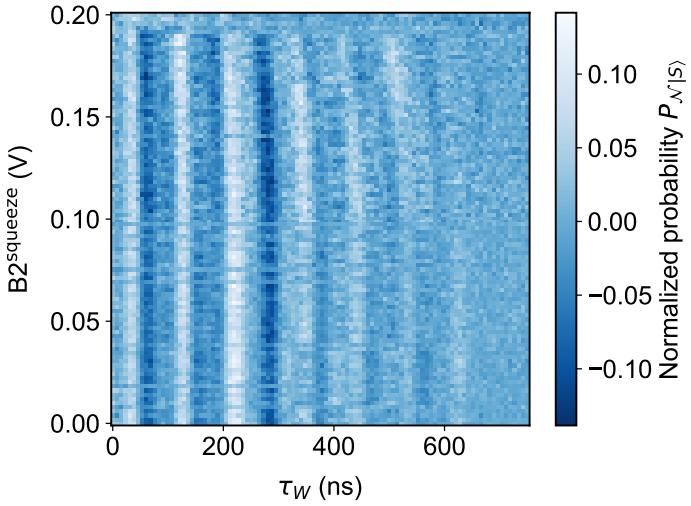

Figure 5.23: Measurement of singlet-triplet oscillations for different squeezing voltages of the second barrier gate $B2^{\text{squeeze}}$.

that, even though the difference in frequency is barely noticeable as it is so small, there is a clear difference in frequency at higher squeezing voltages $B2^{\text{squeeze}}$. This trend is also visible for all values of $B2^{\text{squeeze}}$ in between. An evaluation of the frequencies can be found in figure 5.24. In this analysis, the singlet probability is fitted by

$$\begin{aligned} P_{|S\rangle} = \Big(& A_1 \cos\left(2\pi\nu_1\tau_S + \varphi_1\right) \\ & + A_2 \cos\left(2\pi\nu_2\tau_S + \varphi_2\right) \\ & + A_3 \cos\left(2\pi\nu_3\tau_S + \varphi_3\right) \\ & + A_4 \cos\left(2\pi\nu_4\tau_S + \varphi_4\right)\Big) \exp\left\{-\left(\frac{t}{T_2^*}\right)^2\right\} + P_0, \end{aligned} \tag{5.8.1}$$

meaning that four frequencies ν_i were fitted to the oscillations. As there are four possibilities of spin-valley configurations $(|\uparrow,+\rangle, |\uparrow,-\rangle, |\downarrow,+\rangle, |\downarrow,-\rangle)$, it is likely that this is the reason giving rise to the four frequencies observed here. This is further supported by the

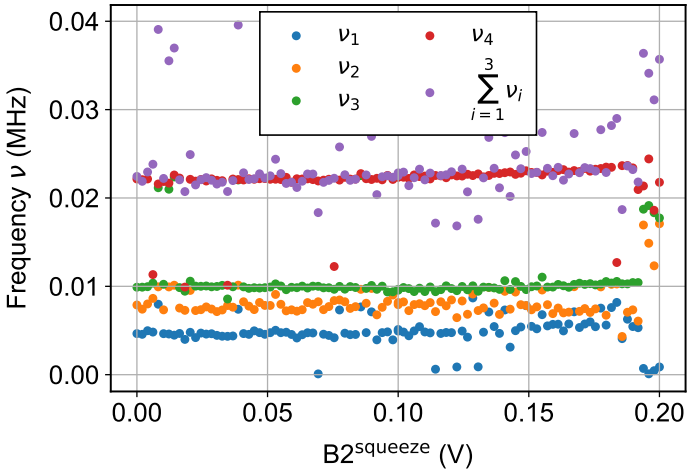

Figure 5.24: Analysis of the frequencies for different squeezing voltages $B2^{\text{squeeze}}$. The first three frequencies added up match the fourth frequency, hinting at a four-level spin-valley system describing these oscillations.

observation that any fitting of more than four branches leads to overfitting of the data present and does not produce new information. Remarkably, the three lowest frequencies added up turn out to be very close to the fourth frequency. This strongly supports the model of two valley states times two spin states leading to exactly four distinct states. Also, in this analysis, a tiny trend of larger frequencies for larger squeezing voltages $B2^{\text{squeeze}}$ is visible.

Chapter 6

Measuring and mapping the valley splitting

In this penultimate chapter, we will explore different methods of measuring and mapping the valley splitting throughout the SQS device. The significance of large valley splitting was discussed in section 2.5. Consequently, we seek straightforward and accurate methods to measure the valley splitting in a given heterostructure and identify its hotspots.In the initial section, we will provide a concise overview of the *magnetospectroscopy* method. This well-established technique offers the advantage of measuring valley splitting with minimal requirements and a straightforward measurement scheme. Nonetheless, certain results suggest that this method can occasionally be susceptible to inaccuracies. In the pursuit of a more reliable approach to measure valley splitting, chapters 6.2 and 6.3 will demonstrate how the coherent shuttling measurements discussed in preceding chapters can be adapted to yield an accurate estimation of the valley splitting. Lastly, chapter 6.4 will employ this method for different voltage configurations of the screening gates in the hope to find configurations allowing the electron to circumvent certain valley splitting hot spots or other unwanted localizations as for example defects.

The measurements presented in this chapter were prepared and performed by Mats Volmer, Tom Struck and I. The presentation and analysis of data in chapters 6.1 and 6.4 was mainly conducted by Mats Volmer.

Overall, this chapter is not meant as an in-depth discussion of the different experiment types, but rather as a very brief outlook on current research which I was able to help shape at an early stage and on the margins as part of my work on this experiment.

6.1 Magnetospectroscopy

Firstly, we will discuss the method of magnetospectroscopy, which is very simple to set up and has only few requirements, as it for example only makes use of ground state physics. Magnetospectroscopy exploits the magnetic field dependence of the charge transitions (cf. figure 4.4), that arises when two or more electrons are involved. The goal is to track the

position of this transitions while changing the magnetic field. When the ground state changes, we expect to see a clear kink in the curve of charge transitions. A more detailed explanation on the physics in a single QD leading to this behaviour can be found in appendix D. In the following, exemplary data of this measurement that yielded good results will be discussed. These measurements were performed in a DQD system and thus show a slightly different behaviour than the single QD measurements described in the appendix. However, the underlying physical mechanisms are the same, just that interdot transitions are investigated here. The first transition is shown in figure 6.1. This is the transition from the (2,0) to the (1,1) state. Here, we see a kink at about 100 µeV. For low magnetic fields, the ground state of the system is the $S(2,0)$ state. The transition into the $T_-(1,1)$ state here changes position linear to the magnetic field, as it is expected from course of the energy of the $T_-(1,1)$. At about 100 µeV, the $T_-(2,0)$ state replaces $S(2,0)$ as the ground state of the system. At this point, the Zeeman splitting matches the valley splitting, so that this energy is the valley splitting of the left dot. From this magnetic field onward, the transition does not change its position anymore. Figure 6.2 shows a similar behaviour for the transition from (1,1) to (0,2). The change of ground state here occurs in the other direction, being the replacement of $S(0,2)$ by $T_-(0,2)$. The general behaviour of this transition is the same as before, just reversed in direction. A kink is visible at about 170 µeV, which is the valley splitting of the right dot.

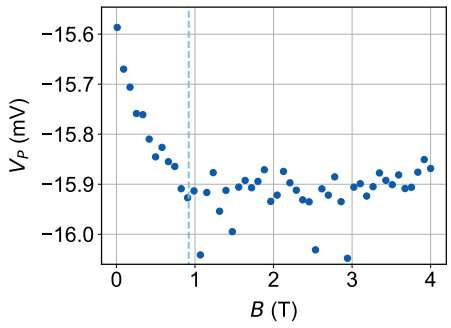

Figure 6.1: Magnetospectroscopy measurement for the left QD. The position of the kink indicating the valley splitting is shown in light blue.

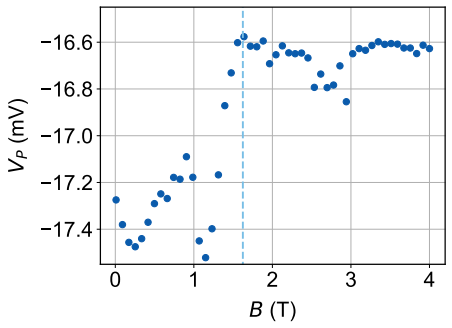

Figure 6.2: Magnetospectroscopy measurement for the right QD. The position of the kink indicating the valley splitting is shown in light blue.

6.2 Valley splitting evaluation in a DQD

As mentioned in the introduction of this chapter, next, we would like to utilize the ST_0-oscillations to measure valley splitting. For this, we modify the experimental procedure of the coherent shuttling experiments in a way where we change which parameters are swept and which are kept constant. So far, we always kept the external magnetic field B constant while sweeping the parameters *evolution time* t and *shuttle distance* d. Now, in

this experiment, we swap the roles of B and d. We measure ST_0-oscillations at a constant distance. Basically any distance up to our maximally reachable distances of about 1.2λ is possible here, but we choose to start with zero distance, meaning the EPR pair is in the DQD configuration. This distance suggests itself as without any shuttling happened before the oscillations are stable and their properties are well-known. Exactly as in the coherent shuttling experiments (figure 5.9), we can now record oscillations for each point in magnetic field. The result of such a measurement is shown in figure 6.3. Again similar as for the coherent shuttling measurements, we fit a single sine function with Gaussian decay to the data. This is shown in figure 6.4.

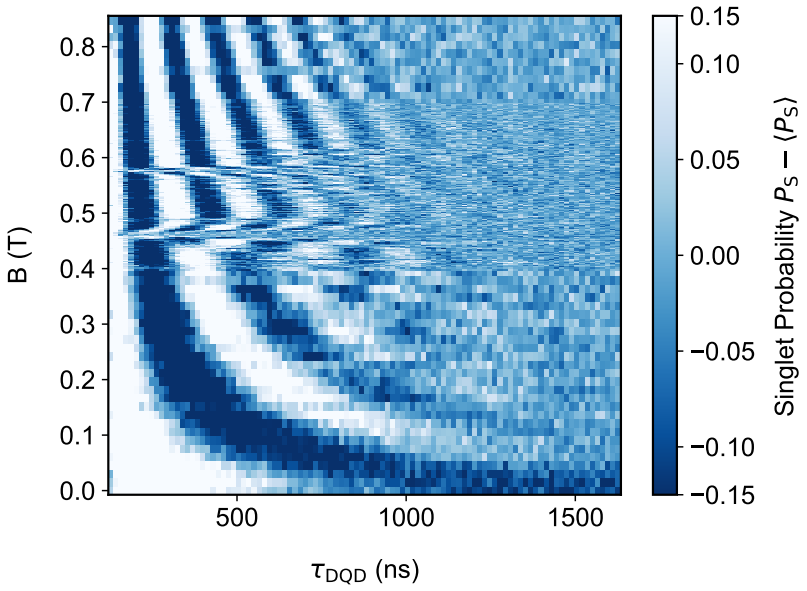

Figure 6.3: Singlet-triplet oscillations in a DQD system for a variable magnetic field. A finer sweep was applied from $0.4\,\mathrm{T}$ to $0.7\,\mathrm{T}$, which is the region around the valley splitting cones.

It is apparent that the oscillations mostly look relatively homogeneous, except for the expected linear scaling of frequency with the magnetic field. However, around $B = 0.46\,\mathrm{T}$ and $B = 0.59\,\mathrm{T}$, two cone-like features are visible. These show a continuously shifted phase for small cones in a magnetic field and no oscillation at all in the center of these features. The magnetic fields of the two cone positions can be directly translated into the valley splitting of each dot by using

$$E_{\mathrm{VS}} = g\mu_B B_{\mathrm{cone}}\,. \tag{6.2.1}$$

A further evaluation of these features can be conducted by extracting the oscillation frequency ν for each trace. This analysis is shown in figure 6.5. We see that two anticrossings in frequency corresponding to the cones are clearly visible. A close-up view of these anticrossings is provided in figure 6.6. It allows to precisely read of the cone positions.

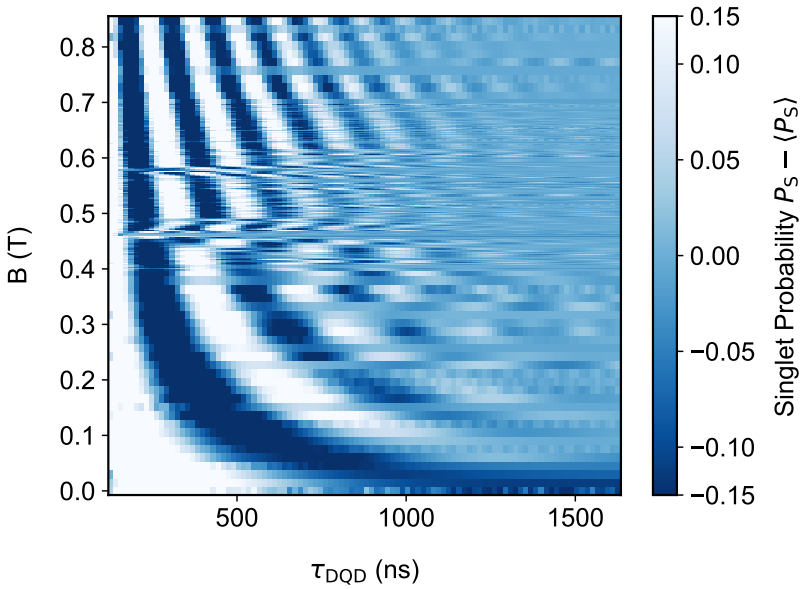

Figure 6.4: Fit to oscillations in a DQD system for a variable magnetic field. Each trace in figure 6.3 was fitted by a sine function with a Gaussian decay.

By repeating this experiment in plenty of different distance points allows us to map the valley splitting throughout the whole device. However, there is an even faster method of doing exactly this, which will be described in the following chapter. Remarkably, this experiment shows that for some of the values of the external magnetic field used in the previous chapter, we might have hit exactly such a valley splitting cone during the measurement. This would explain uncommon or unexpected behaviour of the oscillations. As a result, it is advisable to always perform experiments at very different external magnetic fields before drawing conclusions on the functionality of a device or on physics leading to certain phenomena. Both the measurements shown in figure 5.9a and 5.19a were initially performed at 400 mT, and again recorded at a higher magnetic field for exactly this reason.

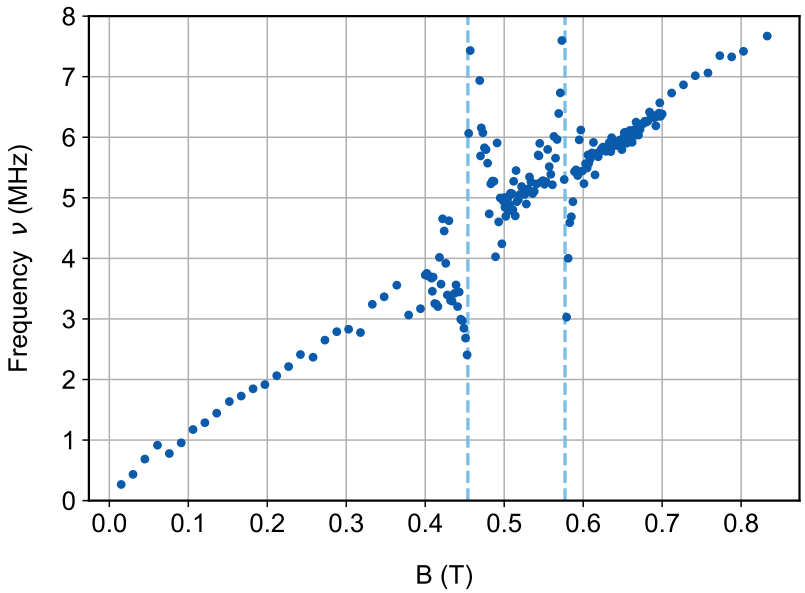

Figure 6.5: Frequency of the oscillations in a DQD system for a magnetic field sweep. The dashed line shows the points at which an anti-crossing occurs.

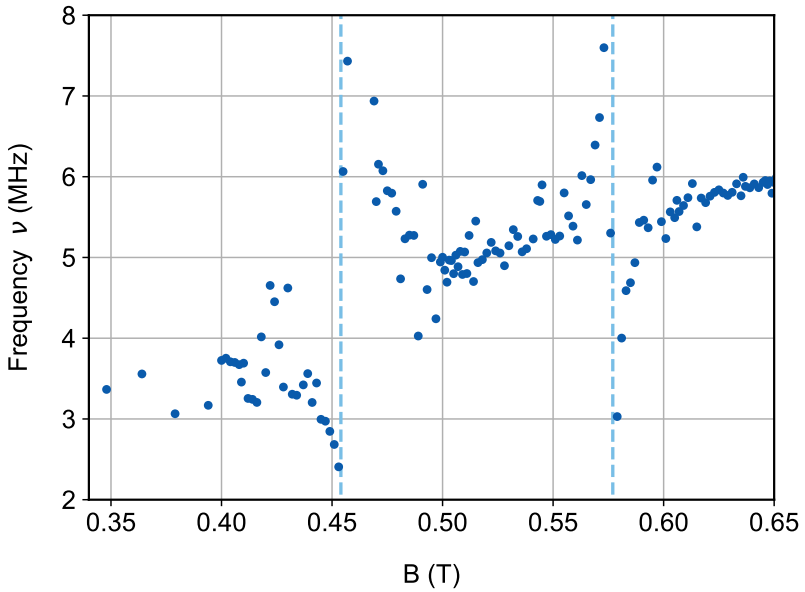

Figure 6.6: Close-up view of the frequency of the oscillations in a DQD system for a magnetic field sweep. The dashed line shows the points at which an anti-crossing occurs.

6.3 Valley splitting mapping by ST_0 oscillation measurement

Whole maps accurately describing the valley splitting throughout the whole SQS device can be recorded using the aforementioned technique. Faster than just recording one map for each different point is here to again change which parameters are kept fixed and which

we sweep over. As we only look for the features at which the oscillations break down, we do not always need to record the full oscillations. It is indeed sufficient to choose a fixed time for which all single shot measurements will be performed ($\tau_{VS} = 300\,\text{ns}$ in our case). This time mostly allows to exactly find these features even though no full oscillations were recorded.

Now, we can continue to sweep the external magnetic field B on the y-axis and sweep the shuttle distance d instead of the time on the x-axis. This way, we get a map that clearly shows the features we were looking for to identify valley splitting. A map of these features throughout the SQS device is shown in figure 6.7. To evaluate the valley splitting, we can

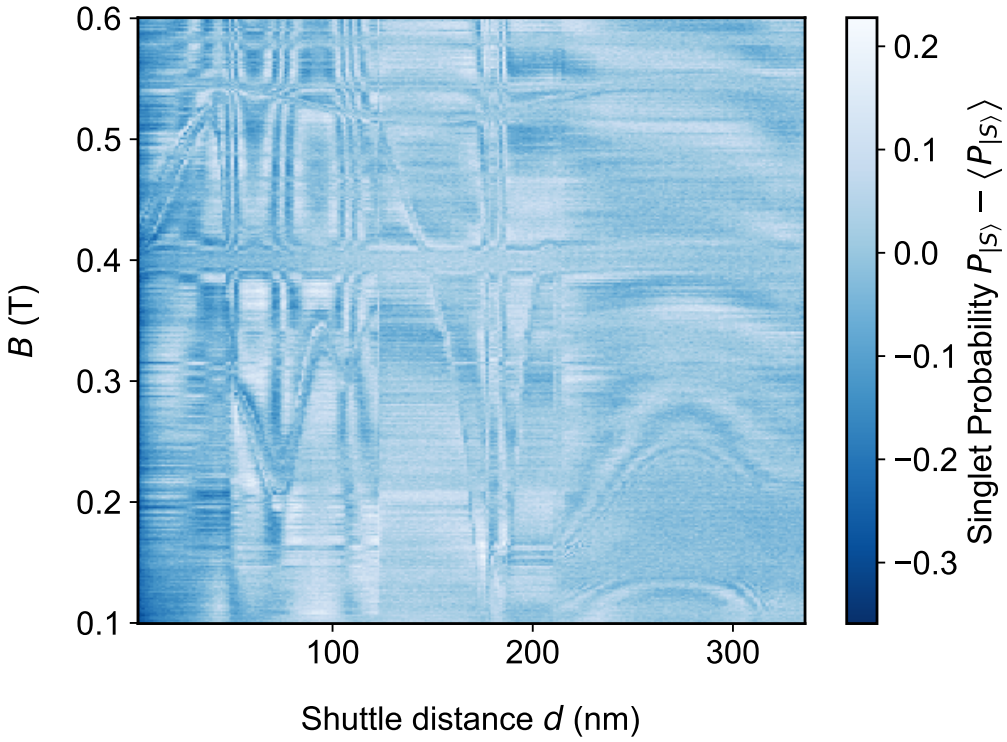

Figure 6.7: Valley splitting map for a fixed oscillation time. Each line corresponds to a vertical cut of figure 6.3 at $\tau_{VS} = 300\,\text{ns}$ and a certain shuttle distance d instead of a DQD configuration.

conduct a *cubic spline fit* of the data. This is a method for fitting a curve to a given set of data points using a special type of curve called *splines*. Splines are smooth, piecewise-defined curves that typically consist of multiple polynomial, here cubic, segments. These segments are connected in such a way that the curve best fits the given data points, while maintaining smoothness and continuity along the curve. This spline fit shows the valley splitting of the shuttled quantum dot along the channel. Evaluating and comparing these fits for different devices, heterostructures or parameter sets yield all the knowledge needed to choose one of those traits based on how well shuttling experiments are expected to work with the valley splitting given. This is especially important as this map can easily capture valley splitting jumps or hot spots, which are still a significant bottleneck of

electron shuttling experiments. Further indicated in the figure are two horizontal dashed lines. These lines correspond to the valley splitting in the DQD system as explained in section 6.2. The dotted, sinusoidal line additionally shows a wiggling of the static QD. A further interpretation of these maps is subject of current research [68].

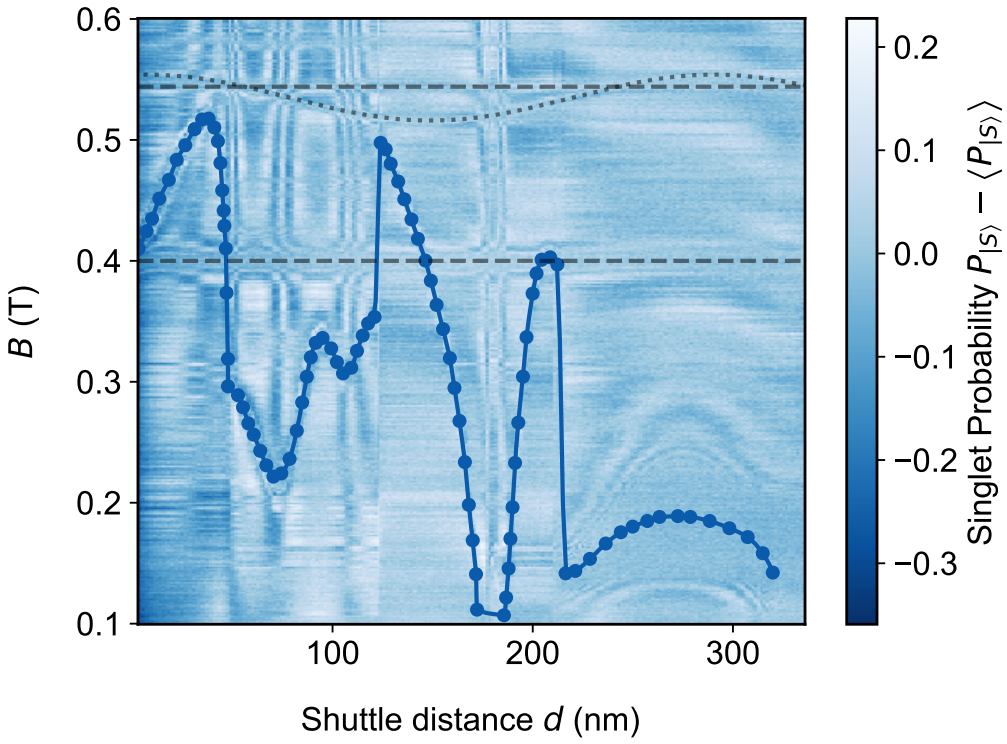

Figure 6.8: Valley splitting map with features highlighted. The blue points show the input for the spline fit, which is shown in dark blue. The grey dashed lines show the valley splitting anti-crossings in the DQD. The oscillating dashed line shows the response of the static QD.

6.4 Valley splitting mapping for different screening gate voltages

One practical example of choosing parameters based on the results of the valley splitting maps is the choice of the screening gate voltages. In normal operation of the shuttle device, both screening gates ST and SB are usually on the same voltage of 100 mV, confining the one-dimensional electron channel (1DEC) exactly in the middle of the SQS device. However, varying the voltages on both screening gate can allow for the 1DEC being formed not in the middle of the device, but shifted to one of the sides. This can have the advantage that the moving dot can easier pass by a defect that is more located on the other side of the SQS device. On the other hand, it can have the drawback that higher voltages need to be applied to one of the screening gates, potentially leading to charging of the silicon cap or the spacer.

For these measurements, we tried a few different screening gate configurations, which are listed in table 6.1. A triangulation measurement on a similar device yielded the conversion rate of 100 mV in screening gate voltage difference corresponding to 6 nm displacement of the 1DEC perpendicular to the shuttle direction. The results of the spline fits to these maps

Table 6.1: Different screening gate configurations used for valley splitting mappings. For each change in configuration, the voltage difference of both gates was changed by 100 mV, corresponding to a displacement of the 1DEC by 6 nm.

Configuration	ST	SB	displ.
1	0 mV	200 mV	12nm
2	50 mV	150 mV	6nm
3	100 mV	100 mV	0 nm
4	150 mV	50 mV	-6 nm

for four different screening gate configurations are shown in figure 6.9. Unfortunately, a scaffold unexpectedly appeared on our experimental setup. As a consequence, the sample could not be used any further, so that it was not possible to measure more configurations.

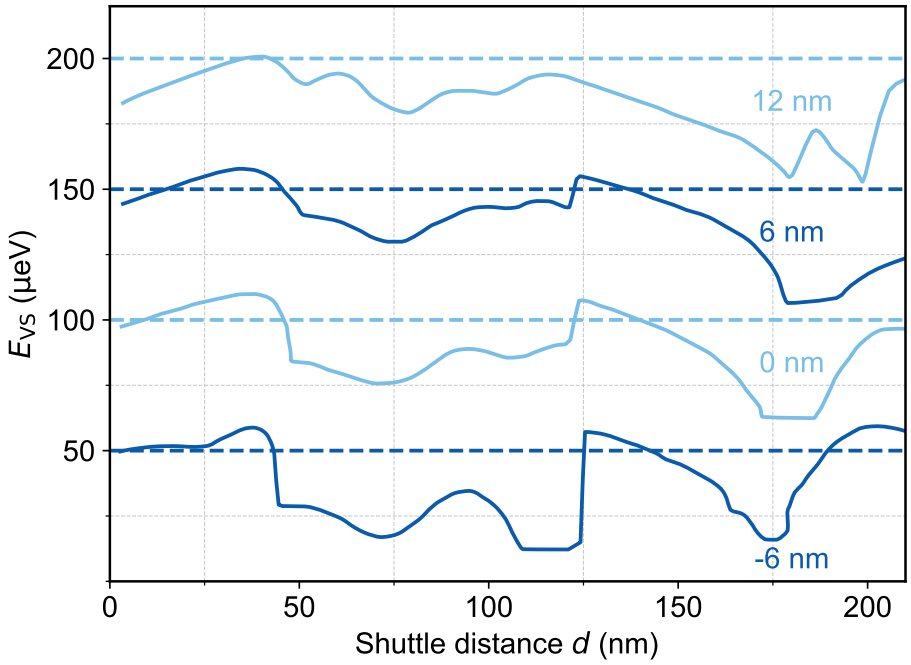

Figure 6.9: Spline fit results for different screening gate configurations. Annotated are the distances by which the 1DEC is displaced due to the different screening gate voltages. The traces are offset by 50 µeV, as indicated by the dashed lines.

Chapter 7

Conclusions and Outlook

This closing chapter will provide a short summary of all the experiments and their results mentioned within this thesis. In addition to that, an outlook how to continue or improve these experiments will be given.

In chapter 3 of this thesis, we explained the measurement workflow and results for mass-characterization of in-house fabricated devices at 4 K. Besides the selection of samples that are appropriate for continuing the experiments described in the chapters after that, the goal of identifying different behaviours for different heterostructures was also successful. In summary, we found out that the QT694 and QT734 heterostructures show excellent behaviour and are further promising because of the purified silicon they contain. On the other hand, we could see that especially the R2203 heterostructure shows a lot of unusual behaviour and has very few working SETs. Consequently, even though it also contains purified silicon, we could identify this heterostructure as unsuitable for our experiments. These results will have a strong influence on future fabrication rounds. Even though the measurement of batches 16, 17 and 19 have been completed, there is a lot to improve for further iterations of pre-characterizing new samples. Quite a lot of processes can still be optimized.
A next reasonable step would be to use newer libraries with more functionalities like QuMADA [88], which would allow for buffered measurements. Since the tuning toolkit described in section 3.4 is open to every measurement framework, a further integration and testing of this would lead to a possibly fully automatized measurement that can be run without constant supervision. This would not necessarily decrease the overall measurement time, but surely free other capacities. Lastly, a new setup replacing the dipstick could significantly improve handling of the experiment and allow for easier sample exchange, faster cooldown and measuring multiple samples at a time.

In chapters 4 to 6, the experiments performed at millikelvin temperature were described. Most of these experiments were performed with the same sample. Also, they mostly build upon each other. First, in chapter 4, charge shuttling and parameter optimization were described. While charge shuttling itself was already achieved before [66], we were able to significantly improve shuttling amplitude and frequency, while also using a longer device than previous works. By defining a fidelity for charge shuttling experiments, we were able

to optimize both parameters. We could identify local hotspots where shuttling fidelity breaks down. These hotspots allow for a sample-specific pulse sequence that adjusts shuttling amplitude and frequency depending on the direction of shuttling and possible defects in the channel. With this, we could maximise the shuttling speed reaching values of up to $28\,\mathrm{m\,s^{-1}}$ for almost all points in the channel. Also for further research, charge shuttling and optimization techniques will have a large impact. While charge shuttling over distances of $10\,\mu\mathrm{m}$ has already been shown [75], this distance still requires operation with a higher speed and optimized parameters. Also, charge shuttling will be the first experiment to be done in the recently fabricated T-junctions, underlining the need for well-developed experimental methods to fit all together to a larger chip.

The most important part of this thesis is the proof of coherent singlet-triplet oscillations after separating an EPR-pair and shuttling a part of it. This was described in chapter 5. We explain how the experimental procedure, more specifically initialization and readout, changes compared to charge shuttling experiments. We showed how to measure hints for coherent shuttling and how to analyze the data with respect to oscillation frequency ν, oscillation amplitude A, and decoherence time T_2^*. We highlighted different analysis and fitting strategies, both for the oscillations itself, as well as for the extracted parameters. For the decoherence time T_2^*, we further described how to see hints of motional narrowing and discuss the agreement with different theoretical models.
To conclude, we present additional measurements on g-factor mapping and entanglement detection. All of this gives a good picture on the coherence of electron shuttling.
As an outlook, similar to previous chapters, these experiments need to be performed with other device types. We were able to detect coherence for a long nominal distance by shuttling back and forth, so the logical next step is to also show this coherence in a longer device. Also, since defects and broken gates prevented us from shuttling through the device, it would be interesting to separate the EPR-pair, shuttle both electrons individually, and bring it back together at the other side of the device. This can hopefully be achieved soon with one of the devices identified in chapter 3.

In the last part of this thesis, chapter 6, we came back to the important property of valley splitting. Given its significance in determining the ease of coherently operating our qubit, we explored various techniques to measure and quantify this valley splitting. We present data of magnetospectroscopy as well as singlet-triplet-oscillation based measurements. Lastly, we showed valley splitting maps for different configurations of the screening gates, which could also help improve the experiments described in chapter 5. Mapping the valley splitting and especially finding valley splitting hotspots will be important as a performance metric for future generations of SQS devices.

In a nutshell, this thesis convincingly shows that coherent electron shuttling is possible. This is an important foundation for using electrons as qubits and scaling up to have a large-scale fault-tolerant quantum computer.

References

[1] G. E. Moore, "Cramming more components onto integrated circuits," *Electronics*, vol. 38, Apr 1965.

[2] R. Schaller, "Moore's law: past, present and future," *IEEE Spectrum*, vol. 34, no. 6, pp. 52–59, 1997.

[3] R. S. Williams, "What's next? [the end of moore's law]," *Computing in Science Engineering*, vol. 19, no. 2, pp. 7–13, 2017.

[4] P. Chen, T. L. Atallah, Z. Lin, P. Wang, S.-J. Lee, J. Xu, Z. Huang, X. Duan, Y. Ping, Y. Huang, J. R. Caram, and X. Duan, "Approaching the intrinsic exciton physics limit in two-dimensional semiconductor diodes," *Nature*, vol. 599, no. 7885, pp. 404–410, Nov 2021. [Online]. Available: https://doi.org/10.1038/s41586-021-03949-7

[5] P. Ball, "Semiconductor technology looks up," *Nature Materials*, vol. 21, no. 2, pp. 132–132, Feb 2022. [Online]. Available: https://doi.org/10.1038/s41563-021-01192-z

[6] R. W. Keyes, "Physical limits in semiconductor electronics," *Science*, vol. 195, no. 4283, pp. 1230–1235, 1977. [Online]. Available: https://www.science.org/doi/abs/10.1126/science.195.4283.1230

[7] Y. Kim, A. Eddins, S. Anand, K. Wei, E. Berg, S. Rosenblatt, H. Nayfeh, Y. Wu, M. Zaletel, K. Temme, and A. Kandala, "Evidence for the utility of quantum computing before fault tolerance," *Nature*, vol. 618, pp. 500–505, 06 2023.

[8] F. Arute, K. Arya, R. Babbush, D. Bacon, J. Bardin, R. Barends, R. Biswas, S. Boixo, F. Brandao, D. Buell, B. Burkett, Y. Chen, J. Chen, B. Chiaro, R. Collins, W. Courtney, A. Dunsworth, E. Farhi, B. Foxen, A. Fowler, C. M. Gidney, M. Giustina, R. Graff, K. Guerin, S. Habegger, M. Harrigan, M. Hartmann, A. Ho, M. R. Hoffmann, T. Huang, T. Humble, S. Isakov, E. Jeffrey, Z. Jiang, D. Kafri, K. Kechedzhi, J. Kelly, P. Klimov, S. Knysh, A. Korotkov, F. Kostritsa, D. Landhuis, M. Lindmark, E. Lucero, D. Lyakh, S. Mandra, J. R. McClean, M. McEwen, A. Megrant, X. Mi, K. Michielsen, M. Mohseni, J. Mutus, O. Naaman, M. Neeley, C. Neill, M. Y. Niu, E. Ostby, A. Petukhov, J. Platt, C. Quintana, E. G. Rieffel, P. Roushan, N. Rubin, D. Sank, K. J. Satzinger, V. Smelyanskiy, K. J. Sung, M. Trevithick, A. Vainsencher, B. Villalonga, T. White, Z. J. Yao, P. Yeh, A. Zalcman, H. Neven, and J. Martinis, "Quantum supremacy using a

programmable superconducting processor," *Nature*, vol. 574, p. 505â€“510, 2019. [Online]. Available: https://www.nature.com/articles/s41586-019-1666-5

[9] B. Yan, Z. Tan, S. Wei, H. Jiang, W. Wang, H. Wang, L. Luo, Q. Duan, Y. Liu, W. Shi, Y. Fei, X. Meng, Y. Han, Z. Shan, J. Chen, X. Zhu, C. Zhang, F. Jin, H. Li, C. Song, Z. Wang, Z. Ma, H. Wang, and G.-L. Long, "Factoring integers with sublinear resources on a superconducting quantum processor," 2022.

[10] A. Steane, "Quantum computing," *Reports on Progress in Physics*, vol. 61, no. 2, pp. 117–173, 1998.

[11] D. Kielpinski, C. Monroe, and D. J. Wineland, "Architecture for a large-scale ion-trap quantum computer," *Nature*, vol. 417, no. 6890, pp. 709–711, Jun 2002. [Online]. Available: https://doi.org/10.1038/nature00784

[12] K. N. Smith, G. S. Ravi, J. M. Baker, and F. T. Chong, "Scaling superconducting quantum computers with chiplet architectures," in *2022 55th IEEE/ACM International Symposium on Microarchitecture (MICRO)*, 2022, pp. 1092–1109.

[13] C. N. Hugh Collins. Ibm unveils 400 qubit-plus quantum processor and next-generation ibm quantum system two. [Online]. Available: https://newsroom.ibm.com/2022-11-09-IBM-Unveils-400-Qubit-Plus-Quantum-Processor-and-Next-Generation-IBM-Quantum-System-Two

[14] L. C. L. Hollenberg, A. D. Greentree, A. G. Fowler, and C. J. Wellard, "Two-dimensional architectures for donor-based quantum computing," *Phys. Rev. B*, vol. 74, no. 4, p. 045311, Jul. 2006.

[15] W. I. L. Lawrie, H. G. J. Eenink, N. W. Hendrickx, J. M. Boter, L. Petit, S. V. Amitonov, M. Lodari, B. Paquelet Wuetz, C. Volk, S. G. J. Philips, G. Droulers, N. Kalhor, F. van Riggelen, D. Brousse, A. Sammak, L. M. K. Vandersypen, G. Scappucci, and M. Veldhorst, "Quantum dot arrays in silicon and germanium," *Appl. Phys. Lett.*, vol. 116, no. 8, 02 2020, 080501.

[16] L. M. K. Vandersypen, H. Bluhm, J. Clarke, A. Dzurak, R. Ishihara, A. Morello, D. Reilly, L. Schreiber, and M. Veldhorst, "Interfacing spin qubits in quantum dots and donors-hot, dense, and coherent," *npj Quantum Inf.*, vol. 3, p. 34, 2017.

[17] D. Loss and D. P. DiVincenzo, "Quantum computation with quantum dots," *Phys. Rev. A*, vol. 57, pp. 120–126, Jan 1998. [Online]. Available: https://link.aps.org/doi/10.1103/PhysRevA.57.120

[18] The Nobel Committee for Chemistry. Scientific background to the nobel prize in chemistry 2023: Quantum dots - seeds of nanoscience. [Online]. Available: https://www.nobelprize.org/uploads/2023/10/advanced-chemistryprize2023.pdf

[19] D. M. Zajac, A. J. Sigillito, M. Russ, F. Borjans, J. M. Taylor, G. Burkard, and J. R. Petta, "Resonantly driven cnot gate for electron spins," *Science*, vol. 359, no. 6374, pp. 439–442, Jan. 2018.

[20] X. Xue, T. F. Watson, J. Helsen, D. R. Ward, D. E. Savage, M. G. Lagally, S. N. Coppersmith, M. A. Eriksson, S. Wehner, and L. M. K. Vandersypen, "Benchmarking gate fidelities in a Si/SiGe two-qubit device," *Phys. Rev. X*, vol. 9, p. 021011, Apr 2019.

[21] X. Xue, M. Russ, N. Samkharadze, B. Undseth, A. Sammak, G. Scappucci, and L. M. K. Vandersypen, "Quantum logic with spin qubits crossing the surface code threshold," *Nature*, vol. 601, no. 7893, pp. 343–347, Jan 2022.

[22] J. Yoneda, K. Takeda, T. Otsuka, T. Nakajima, M. R. Delbecq, G. Allison, T. Honda, T. Kodera, S. Oda, Y. Hoshi, N. Usami, K. M. Itoh, and S. Tarucha, "A quantum-dot spin qubit with coherence limited by charge noise and fidelity higher than 99.9%," *Nat. Nanotechnol.*, vol. 13, no. 2, pp. 102–106, Feb. 2018.

[23] A. R. Mills, C. R. Guinn, M. J. Gullans, A. J. Sigillito, M. M. Feldman, E. Nielsen, and J. R. Petta, "Two-qubit silicon quantum processor with operation fidelity exceeding 99%," *Sci. Adv.*, vol. 8, no. 14, p. eabn5130, 2022.

[24] T. F. Watson, S. G. J. Philips, E. Kawakami, D. R. Ward, P. Scarlino, M. Veldhorst, D. E. Savage, M. G. Lagally, M. Friesen, S. N. Coppersmith, M. A. Eriksson, and L. M. K. Vandersypen, "A programmable two-qubit quantum processor in silicon," *Nature*, vol. 555, no. 7698, pp. 633–637, Mar. 2018.

[25] A. Noiri, K. Takeda, T. Nakajima, T. Kobayashi, A. Sammak, G. Scappucci, and S. Tarucha, "Fast universal quantum gate above the fault-tolerance threshold in silicon," *Nature*, vol. 601, no. 7893, pp. 338–342, Jan. 2022.

[26] E. Kammerloher, A. Schmidbauer, L. Diebel, I. Seidler, M. Neul, M. Künne, A. Ludwig, J. Ritzmann, A. Wieck, D. Bougeard, L. R. Schreiber, and H. Bluhm, "Sensing dot with high output swing for scalable baseband readout of spin qubits. Preprint at https://arxiv.org/abs/2107.13598," 2021.

[27] T. Struck, J. Lindner, A. Hollmann, F. Schauer, A. Schmidbauer, D. Bougeard, and L. R. Schreiber, "Robust and fast post-processing of single-shot spin qubit detection events with a neural network," *Sci. Rep.*, vol. 11, no. 1, p. 16203, Aug 2021.

[28] A. Noiri, K. Takeda, J. Yoneda, T. Nakajima, T. Kodera, and S. Tarucha, "Radio-frequency-detected fast charge sensing in undoped silicon quantum dots," *Nano Lett.*, vol. 20, no. 2, pp. 947–952, 2020.

[29] E. J. Connors, J. Nelson, and J. M. Nichol, "Rapid high-fidelity spin-state readout in Si/SiGe quantum dots via rf reflectometry," *Phys. Rev. Appl.*, vol. 13, p. 024019, Feb 2020.

[30] S. G. J. Philips, M. T. Mądzik, S. V. Amitonov, S. L. de Snoo, M. Russ, N. Kalhor, C. Volk, W. I. L. Lawrie, D. Brousse, L. Tryputen, B. P. Wuetz, A. Sammak, M. Veldhorst, G. Scappucci, and L. M. K. Vandersypen, "Universal control of a six-qubit quantum processor in silicon," *Nature*, vol. 609, no. 7929, pp. 919–924, Sep 2022.

[31] J. M. Boter, J. P. Dehollain, J. P. van Dijk, Y. Xu, T. Hensgens, R. Versluis, H. W. Naus, J. S. Clarke, M. Veldhorst, F. Sebastiano, and L. M. Vandersypen, "Spiderweb array: A sparse spin-qubit array," *Phys. Rev. Appl.*, vol. 18, p. 024053, Aug 2022.

[32] P.-A. Mortemousque, E. Chanrion, B. Jadot, H. Flentje, A. Ludwig, A. D. Wieck, M. Urdampilleta, C. Bäuerle, and T. Meunier, "Coherent control of individual electron spins in a two-dimensional quantum dot array," *Nat. Nanotechnol.*, vol. 16, no. 3, pp. 296–301, Mar 2021.

[33] R. Maurand, X. Jehl, D. Kotekar-Patil, A. Corna, H. Bohuslavskyi, R. Laviéville, L. Hutin, S. Barraud, M. Vinet, M. Sanquer, and S. De Franceschi, "A cmos silicon spin qubit," *Nature Communications*, vol. 7, no. 1, p. 13575, Nov 2016. [Online]. Available: https://doi.org/10.1038/ncomms13575

[34] M. De Michielis, E. Ferraro, E. Prati, L. Hutin, B. Bertrand, E. Charbon, D. J. Ibberson, and M. Fernando Gonzalez-Zalba, "Silicon spin qubits from laboratory to industry," *Journal of Physics D: Applied Physics*, vol. 56, no. 36, p. 363001, 2023.

[35] V. Langrock, J. A. Krzywda, N. Focke, I. Seidler, L. R. Schreiber, and Ł. Cywiński, "Blueprint of a scalable spin qubit shuttle device for coherent mid-range qubit transfer in disordered si/sige/sio$_2$," *PRX Quantum*, vol. 4, p. 020305, 2023.

[36] P. Krantz, M. Kjaergaard, F. Yan, T. P. Orlando, S. Gustavsson, and W. D. Oliver, "A quantum engineer's guide to superconducting qubits," *Applied Physics Reviews*, vol. 6, no. 2, p. 021318, 06 2019. [Online]. Available: https://doi.org/10.1063/1.5089550

[37] G. Burkard, T. D. Ladd, A. Pan, J. M. Nichol, and J. R. Petta, "Semiconductor spin qubits," *Rev. Mod. Phys.*, vol. 95, p. 025003, Jun 2023. [Online]. Available: https://link.aps.org/doi/10.1103/RevModPhys.95.025003

[38] J. Wang, X.-J. Liu, and H. Hu, "Time evolution of quantum entanglement of an EPR pair in a localized environment," *New Journal of Physics*, vol. 20, no. 5, p. 053015, May 2018. [Online]. Available: https://iopscience.iop.org/article/10.1088/1367-2630/aabe3d

[39] H. Zheng, J. Zhang, and R. Berndt, "A minimal double quantum dot," *Scientific Reports*, vol. 7, no. 1, p. 10764, Sep 2017. [Online]. Available: https://doi.org/10.1038/s41598-017-10814-z

[40] X. Wang, S. Yang, and S. Das Sarma, "Quantum theory of the charge-stability diagram of semiconductor double-quantum-dot systems," *Phys. Rev. B*, vol. 84, p. 115301, Sep 2011. [Online]. Available: https://link.aps.org/doi/10.1103/PhysRevB.84.115301

[41] W. G. van der Wiel, T. Fujisawa, S. Tarucha, and L. P. Kouwenhoven, "A double quantum dot as an artificial two-level system," *Japanese Journal of Applied Physics*, vol. 40, no. 3S, p. 2100, mar 2001. [Online]. Available: https://dx.doi.org/10.1143/JJAP.40.2100

[42] M. Veldhorst, C. H. Yang, J. C. C. Hwang, W. Huang, J. P. Dehollain, J. T. Muhonen, S. Simmons, A. Laucht, F. E. Hudson, K. M. Itoh, A. Morello, and A. S. Dzurak, "A two-qubit logic gate in silicon," *Nature*, vol. 526, pp. 410–414, 2014. [Online]. Available: https://api.semanticscholar.org/CorpusID:4470145

[43] M. Ni, R.-L. Ma, Z.-Z. Kong, X. Xue, S.-K. Zhu, C. Wang, A.-R. Li, N. Chu, W.-Z. Liao, G. Cao, G.-L. Wang, G.-C. Guo, X. Hu, H.-W. Jiang, H.-O. Li, and G.-P. Guo, "A swap gate for spin qubits in silicon," 2023.

[44] F. A. Zwanenburg, A. S. Dzurak, A. Morello, M. Y. Simmons, L. C. L. Hollenberg, G. Klimeck, S. Rogge, S. N. Coppersmith, and M. A. Eriksson, "Silicon quantum electronics," *Rev. Mod. Phys.*, vol. 85, pp. 961–1019, Jul 2013. [Online]. Available: https://link.aps.org/doi/10.1103/RevModPhys.85.961

[45] L. R. Schreiber and H. Bluhm, "Silicon comes back," *Nature Nanotechnology*, vol. 9, no. 12, pp. 966–968, Dec. 2014. [Online]. Available: https://doi.org/10.1038/nnano.2014.249

[46] P. Stano and D. Loss, "Review of performance metrics of spin qubits in gated semiconducting nanostructures," *Nature Reviews Physics*, vol. 4, no. 10, pp. 672–688, Oct. 2022. [Online]. Available: https://doi.org/10.1038/s42254-022-00484-w

[47] E. Kawakami, P. Scarlino, D. R. Ward, F. R. Braakman, D. E. Savage, M. G. Lagally, M. Friesen, S. N. Coppersmith, M. A. Eriksson, and L. M. K. Vandersypen, "Electrical control of a long-lived spin qubit in a Si/SiGe quantum dot," *Nature Nanotechnology*, vol. 9, no. 9, pp. 666–670, Sep. 2014, number: 9 Publisher: Nature Publishing Group. [Online]. Available: https://www.nature.com/articles/nnano.2014.153

[48] E. Kawakami, T. Jullien, P. Scarlino, D. R. Ward, D. E. Savage, M. G. Lagally, V. V. Dobrovitski, M. Friesen, S. N. Coppersmith, M. A. Eriksson, and L. M. K. Vandersypen, "Gate fidelity and coherence of an electron spin in an Si/SiGe quantum dot with micromagnet," *Proceedings of the National Academy of Sciences*, vol. 113, no. 42, pp. 11 738–11 743, Oct. 2016, publisher: Proceedings of the National Academy of Sciences. [Online]. Available: https://www.pnas.org/doi/abs/10.1073/pnas.1603251113

[49] S. Shankar, A. M. Tyryshkin, J. He, and S. A. Lyon, "Spin relaxation and coherence times for electrons at the Si/sio$_2$ interface," *Phys. Rev. B*, vol. 82, p. 195323, Nov 2010. [Online]. Available: https://link.aps.org/doi/10.1103/PhysRevB.82.195323

[50] E. Ferraro and E. Prati, "Is all-electrical silicon quantum computing feasible in the long term?" *Physics Letters A*, vol. 384, no. 17, p. 126352, Jun. 2020. [Online]. Available: https://www.sciencedirect.com/science/article/pii/S0375960120301626

[51] A. M. J. Zwerver, T. Krähenmann, T. F. Watson, L. Lampert, H. C. George, R. Pillarisetty, S. A. Bojarski, P. Amin, S. V. Amitonov, J. M. Boter, R. Caudillo, D. Correas-Serrano, J. P. Dehollain, G. Droulers, E. M. Henry, R. Kotlyar, M. Lodari, F. Lüthi, D. J. Michalak, B. K. Mueller, S. Neyens, J. Roberts, N. Samkharadze, G. Zheng, O. K. Zietz, G. Scappucci, M. Veldhorst, L. M. K. Vandersypen, and J. S. Clarke, "Qubits made by advanced semiconductor manufacturing," *Nat. Electron.*, vol. 5, no. 3, pp. 184–190, Mar. 2022.

[52] X. Mi, M. Benito, S. Putz, D. M. Zajac, J. M. Taylor, G. Burkard, and J. R. Petta, "A coherent spinâ€"photon interface in silicon," *Nature*, vol. 555, no. 7698, pp. 599–603, Mar. 2018.

[53] N. Samkharadze, G. Zheng, N. Kalhor, D. Brousse, A. Sammak, U. C. Mendes, A. Blais, G. Scappucci, and L. M. K. Vandersypen, "Strong spin-photon coupling in silicon," *Science*, vol. 359, no. 6380, pp. 1123–1127, 2018.

[54] A. J. Landig, J. V. Koski, P. Scarlino, U. C. Mendes, A. Blais, C. Reichl, W. Wegscheider, A. Wallraff, K. Ensslin, and T. Ihn, "Coherent spinâ€"photon coupling using a resonant exchange qubit," *Nature*, vol. 560, no. 7717, pp. 179–184, Aug. 2018.

[55] F. Borjans, X. Croot, X. Mi, M. Gullans, and J. Petta, "Resonant microwave-mediated interactions between distant electron spins," *Nature*, vol. 577, pp. 195–198, 2020.

[56] F. Borjans, X. Croot, S. Putz, X. Mi, S. M. Quinn, A. Pan, J. Kerckhoff, E. J. Pritchett, C. A. Jackson, L. F. Edge, R. S. Ross, T. D. Ladd, M. G. Borselli, M. F. Gyure, and J. R. Petta, "Split-gate cavity coupler for silicon circuit quantum electrodynamics," *Appl. Phys. Lett.*, vol. 116, no. 23, p. 234001, 2020.

[57] S. Hermelin, S. Takada, M. Yamamoto, S. Tarucha, A. D. Wieck, L. Saminadayar, C. Bäuerle, and T. Meunier, "Electrons surfing on a sound wave as a platform for quantum optics with flying electrons," *Nature*, vol. 477, no. 7365, pp. 435–438, Sep. 2011.

[58] R. P. G. McNeil, M. Kataoka, C. J. B. Ford, C. H. W. Barnes, D. Anderson, G. A. C. Jones, I. Farrer, and D. A. Ritchie, "On-demand single-electron transfer between distant quantum dots," *Nature*, vol. 477, no. 7365, pp. 439–442, Sep. 2011.

[59] S. Takada, H. Edlbauer, H. V. Lepage, J. Wang, P.-A. Mortemousque, G. Georgiou, C. H. W. Barnes, C. J. B. Ford, M. Yuan, P. V. Santos, X. Waintal, A. Ludwig, A. D. Wieck, M. Urdampilleta, T. Meunier, and C. Bäuerle, "Sound-driven single-electron transfer in a circuit of coupled quantum rails," *Nat. Commun.*, vol. 10, no. 1, p. 4557, Oct. 2019.

[60] B. Jadot, P. Mortemousque, E. Chanrion, V. Thiney, A. Ludwig, A. Wieck, M. Urdampilleta, C. Bäuerle, and T. Meunier, "Distant spin entanglement via fast and coherent electron shuttling," *Nat. Nanotechnol.*, vol. 16, pp. 570–575, 2021.

[61] T. A. Baart, M. Shafiei, T. Fujita, C. Reichl, W. Wegscheider, and L. M. K. Vandersypen, "Single-spin ccd," *Nat. Nanotechnol.*, vol. 11, no. 4, pp. 330–334, Apr. 2016.

[62] H. Flentje, P.-A. Mortemousque, R. Thalineau, A. Ludwig, A. D. Wieck, C. Bäuerle, and T. Meunier, "Coherent long-distance displacement of individual electron spins," *Nat. Commun.*, vol. 8, no. 1, p. 501, Sep. 2017.

[63] A. R. Mills, D. M. Zajac, M. J. Gullans, F. J. Schupp, T. M. Hazard, and J. R. Petta, "Shuttling a single charge across a one-dimensional array of silicon quantum dots," *Nat Commun.*, vol. 10, p. 1063, 2019.

[64] J. Yoneda, W. Huang, M. Feng, C. H. Yang, K. W. Chan, T. Tanttu, W. Gilbert, R. C. C. Leon, F. E. Hudson, K. M. Itoh, A. Morello, S. D. Bartlett, A. Laucht, A. Saraiva, and A. S. Dzurak, "Coherent spin qubit transport in silicon," *Nat. Commun.*, vol. 12, no. 1, p. 4114, Jul. 2021.

[65] A. Zwerver, S. Amitonov, S. de Snoo, M. Mądzik, M. Rimbach-Russ, A. Sammak, G. Scappucci, and L. Vandersypen, "Shuttling an electron spin through a silicon quantum dot array," *PRX Quantum*, vol. 4, p. 030303, Jul 2023. [Online]. Available: https://link.aps.org/doi/10.1103/PRXQuantum.4.030303

[66] I. Seidler, T. Struck, R. Xue, N. Focke, S. Trellenkamp, H. Bluhm, and L. R. Schreiber, "Conveyor-mode single-electron shuttling in Si/SiGe for a scalable quantum computing architecture," *npj Quantum Inf.*, vol. 8, no. 1, p. 100, Aug 2022.

[67] T. Struck, M. Volmer, L. Visser, T. Offermann, R. Xue, J.-S. Tu, S. Trellenkamp, Ł. Cywiński, H. Bluhm, and L. R. Schreiber, "Spin-epr-pair separation by conveyor-mode single electron shuttling in si/sige," 2023.

[68] T. Struck, M. Volmer, L. Visser, A. Sala, M. Oberländer, B. Chen, T. Offermann, R. Xue, J.-S. Tu, S. Trellenkamp, Ł. Cywiński, H. Bluhm, and L. R. Schreiber, "Valley-splitting mapping by conveyor-mode spin-coherent single electron shuttling," 2023, manuscript in preparation.

[69] M. Künne, A. Willmes, M. Oberländer, C. Gorjaew, J. D. Teske, H. Bhardwaj, M. Beer, E. Kammerloher, R. Otten, I. Seidler, R. Xue, L. R. Schreiber, and H. Bluhm, "The spinbus architecture: Scaling spin qubits with electron shuttling. Preprint at https://arxiv.org/abs/2306.16348," 2023.

[70] T. Struck, A. Hollmann, F. Schauer, O. Fedorets, A. Schmidbauer, K. Sawano, H. Riemann, N. V. Abrosimov, Ł. Cywiński, D. Bougeard, and L. R. Schreiber, "Low-frequency spin qubit energy splitting noise in highly purified 28 Si/SiGe," *npj Quantum Inf.*, vol. 6, no. 1, pp. 1–7, May 2020.

[71] C. N. Hugh Collins. Intel's new chip to advance silicon spin qubit research for quantum computing. [Online]. Available: https://www.intel.com/content/www/us/en/newsroom/news/quantum-computing-chip-to-advance-research.html#:~:text=Intel%E2%80%99s%20New%20Chip%20to%20Advance,social%3A%20More%20New%20Technologies%20News

[72] F. Borsoi, N. W. Hendrickx, V. John, M. Meyer, S. Motz, F. van Riggelen, A. Sammak, S. L. de Snoo, G. Scappucci, and M. Veldhorst, "Shared control of a 16 semiconductor quantum dot crossbar array," *Nature Nanotechnology*, pp. 1–7, Aug. 2023, publisher: Nature Publishing Group. [Online]. Available: https://www.nature.com/articles/s41565-023-01491-3

[73] R. D. V. M. III, "Architecture of a quantum multicomputer optimized for shor's factoring algorithm," 2006.

[74] R. Li, L. Petit, D. P. Franke, J. P. Dehollain, J. Helsen, M. Steudtner, N. K. Thomas, Z. R. Yoscovits, K. J. Singh, S. Wehner, L. M. K. Vandersypen, J. S. Clarke, and M. Veldhorst, "A crossbar network for silicon quantum dot qubits," *Sci. Adv.*, vol. 4, no. 7, p. eaar3960, Jul. 2018.

[75] R. Xue, M. Beer, I. Seidler, S. Humpohl, J.-S. Tu, S. Trellenkamp, T. Struck, H. Bluhm, and L. R. Schreiber, "Si/sige qubus for single electron information-processing devices with memory and micron-scale connectivity function," 2023.

[76] M. Volmer, "Valley splitting mapping in electron shuttling devices," 2022.

[77] L. Visser, "Device quality evaluation and methods for coherent spin shuttling in a si/sige qubus," 2022.

[78] F. Schäffler, "High-mobility Si and Ge structures," *Semiconductor Science and Technology*, vol. 12, no. 12, p. 1515, Dec. 1997. [Online]. Available: https://dx.doi.org/10.1088/0268-1242/12/12/001

[79] D. J. Paul, "Si/SiGe heterostructures: from material and physics to devices and circuits," *Semiconductor Science and Technology*, vol. 19, no. 10, p. R75, Sep. 2004. [Online]. Available: https://dx.doi.org/10.1088/0268-1242/19/10/R02

[80] N. Focke, "Si/sige quantum bus simulation and concept of mass-characterization for scalable quantum computation," Master's thesis, RWTH Aachen University, 2022.

[81] M. Beer, "Optimized device design for long range coherent electron spin shuttling in si/sige," Master's thesis, RWTH Aachen University, 2022.

[82] Stanford Research Systems, *MODEL SR830 DSP Lock-In Amplifier*, 2011. [Online]. Available: https://www.thinksrs.com/downloads/pdfs/manuals/SR830m.pdf

[83] Keithley. 2400 standard series smu. [Online]. Available: https://www.tek.com/en/products/keithley/source-measure-units/2400-standard-series-sourcemeter

[84] Adlink. Usb/lpci/lpcie-3488a. [Online]. Available: https://www.adlinktech.com/Products/GPIB_Modular_Instruments/GPIB/LPCIe-3488A

[85] W. Albrecht, J. Moers, and B. Hermanns, "HNF - Helmholtz Nano Facility," *Journal of large-scale research facilities JLSRF*, vol. 3, p. A112, May 2017.

[86] VonRoll USA Inc. 7031 - ge varnish safety data sheet. [Online]. Available: https://estore.oxinst.com/INTERSHOP/static/WFS/Oxinst-US-Site/-/Oxinst/en_US/PDFS/VonRoll%207031%20-%20GE%20Varnish%20SDS%20Rev3%2029%2004%202015.pdf

[87] KLayout. [Online]. Available: https://www.klayout.de/

[88] "Qumada: Measurement abstraction and database access layer for qcodes." [Online]. Available: https://github.com/qutech/QuMADA

[89] H. N. We, S. Humpohl, K. Ramesh, and P. Surrey, "tuning toolkit framework." [Online]. Available: git-ce.rwth-aachen.de/qutech/lab_software/tuning_toolkit

[90] S. Kindel, "Electrical characterization of high-quality oxides for si-mos quantum devices," 2019.

[91] R. L. Puurunen, "Surface chemistry of atomic layer deposition: A case study for the trimethylaluminum/water process," *Journal of Applied Physics*, vol. 97, no. 12, pp. 1–52, 2005, publisher: American Institute of Physics. [Online]. Available: https://research.aalto.fi/en/publications/surface-chemistry-of-atomic-layer-deposition-a-case-study-for-the

[92] W. Mönch, "Role of virtual gap states and defects in metal-semiconductor contacts," *Physical Review Letters*, vol. 58, no. 12, pp. 1260–1263, Mar. 1987, publisher: American Physical Society. [Online]. Available: https://link.aps.org/doi/10.1103/PhysRevLett.58.1260

[93] H. B. Profijt, S. E. Potts, M. C. M. van de Sanden, and W. M. M. Kessels, "Plasma-Assisted Atomic Layer Deposition: Basics, Opportunities, and Challenges," *Journal of Vacuum Science & Technology A*, vol. 29, no. 5, p. 050801, Aug. 2011. [Online]. Available: https://doi.org/10.1116/1.3609974

[94] N. Ciroth, "Simulation of coherent spin-shuttling in a sige-qubus with dilute local defects," Master's thesis, RWTH Aachen University, 2023.

[95] M. Nurizzo, B. Jadot, P.-A. Mortemousque, V. Thiney, E. Chanrion, D. Niegemann, M. Dartiailh, A. Ludwig, A. D. Wieck, C. Bäuerle, M. Urdampilleta, and T. Meunier, "Complete readout of two-electron spin states in a double quantum dot," *PRX Quantum*, vol. 4, p. 010329, Mar 2023.

[96] P.-A. Mortemousque, B. Jadot, E. Chanrion, V. Thiney, C. Bäuerle, A. Ludwig, A. D. Wieck, M. Urdampilleta, and T. Meunier, "Enhanced spin coherence while displacing electron in a two-dimensional array of quantum dots," *PRX Quantum*, vol. 2, p. 030331, Aug 2021.

[97] M. Vasiliu and D. A. Dixon, "Silicon," in *Encyclopedia of Geochemistry: A Comprehensive Reference Source on the Chemistry of the Earth*, ser. Encyclopedia of Earth Sciences Series, W. M. White, Ed. Cham: Springer International Publishing, 2018, pp. 1335–1337. [Online]. Available: https://doi.org/10.1007/978-3-319-39312-4_236

[98] L. V. C. Assali, H. M. Petrilli, R. B. Capaz, B. Koiller, X. Hu, and S. Das Sarma, "Hyperfine interactions in silicon quantum dots," *Phys. Rev. B*, vol. 83, p. 165301, 2011.

[99] Ł. Cywiński, W. M. Witzel, and S. Das Sarma, "Pure quantum dephasing of a solid-state electron spin qubit in a large nuclear spin bath coupled by long-range hyperfine-mediated interaction," *Phys. Rev. B*, vol. 79, p. 245314, 2009.

[100] I. A. Merkulov, A. L. Efros, and M. Rosen, "Electron spin relaxation by nuclei in semiconductor quantum dots," *Phys. Rev. B*, vol. 65, no. 20, p. 205309, 2002.

Appendix A

Bondmaps

In this section, the bondmaps used for different interposer versions are provided.

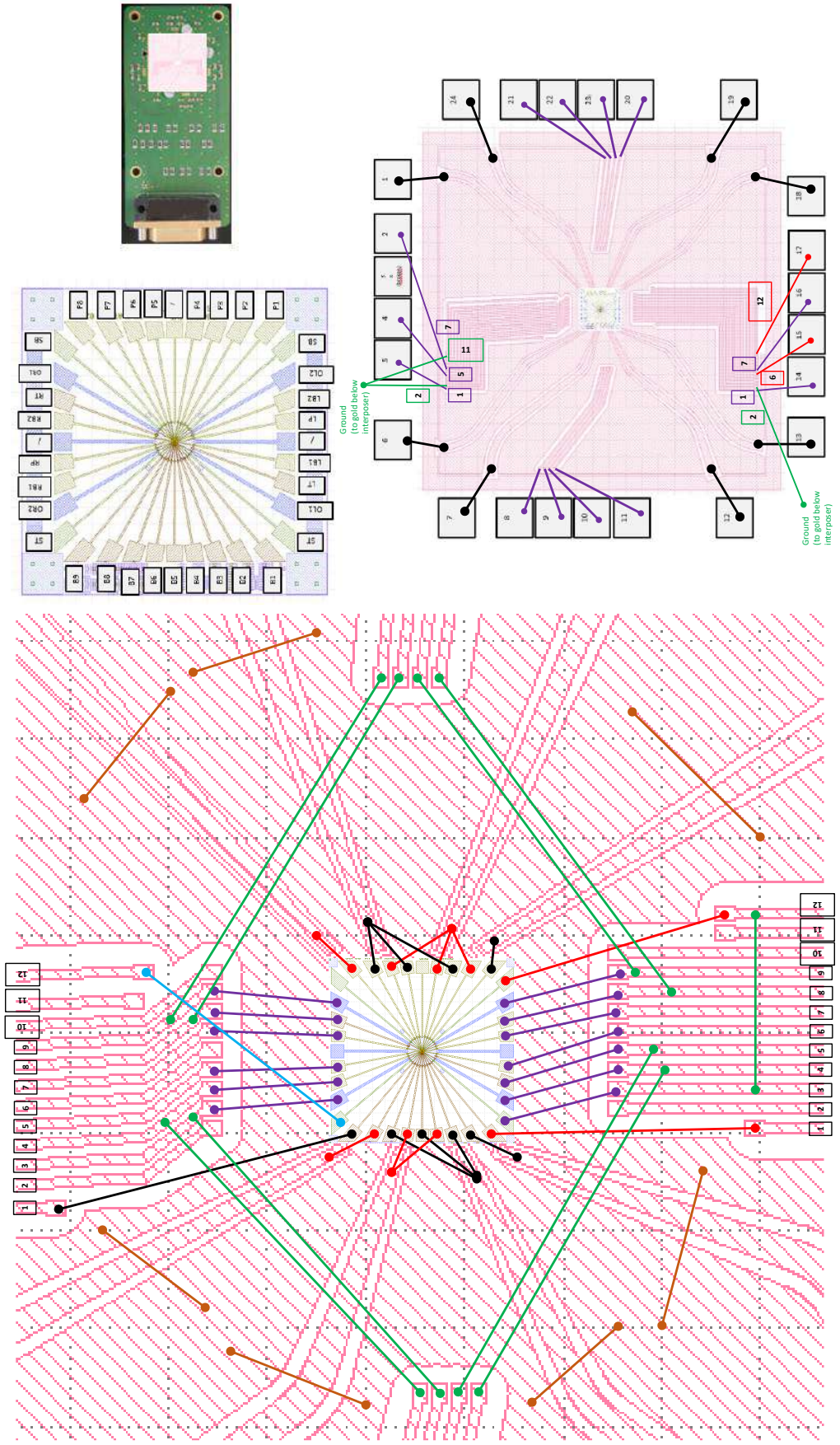

Figure A.1: Bondmap of the interposer version 1.

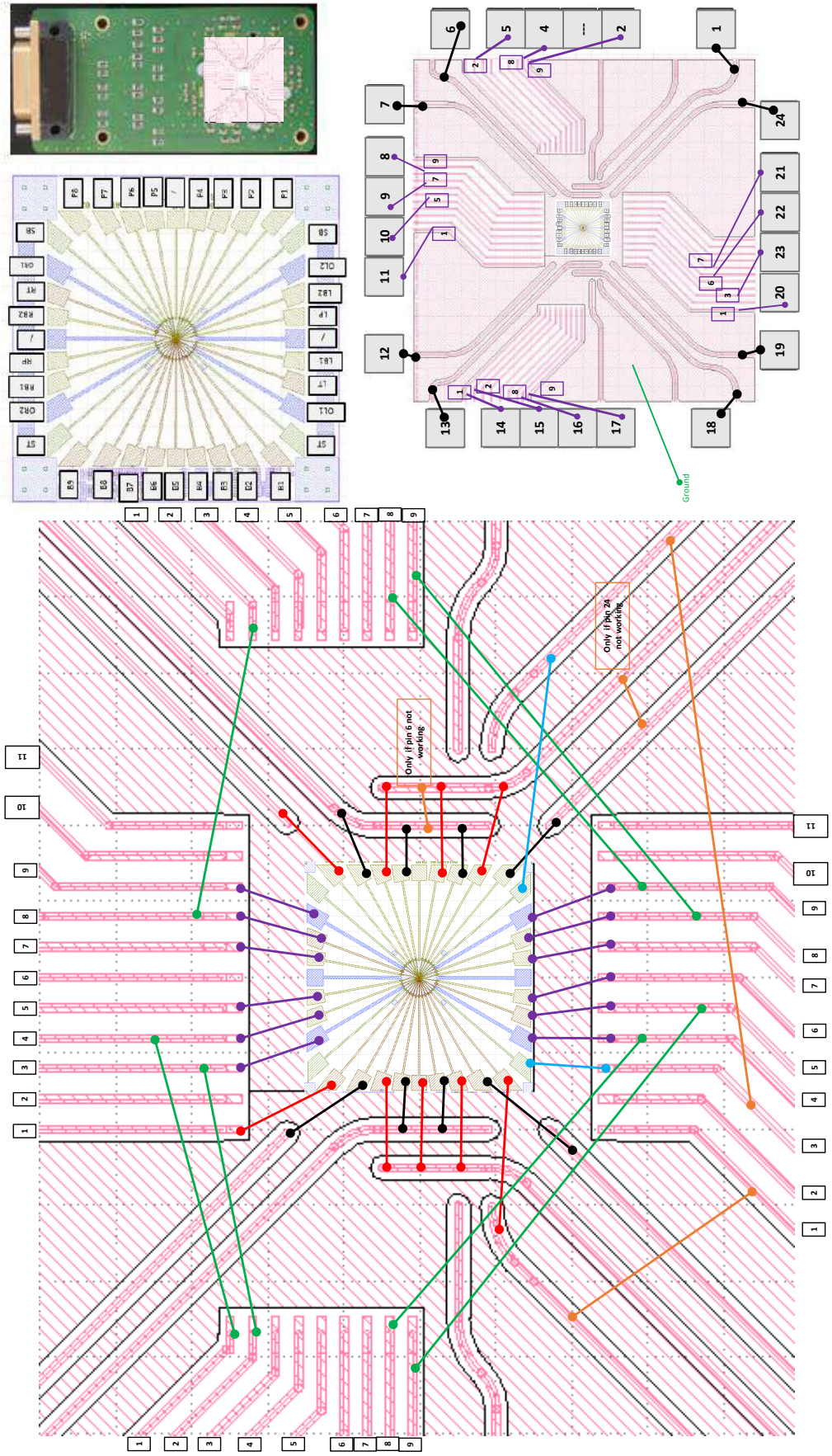

Figure A.2: Bondmap of the interposer version 2.

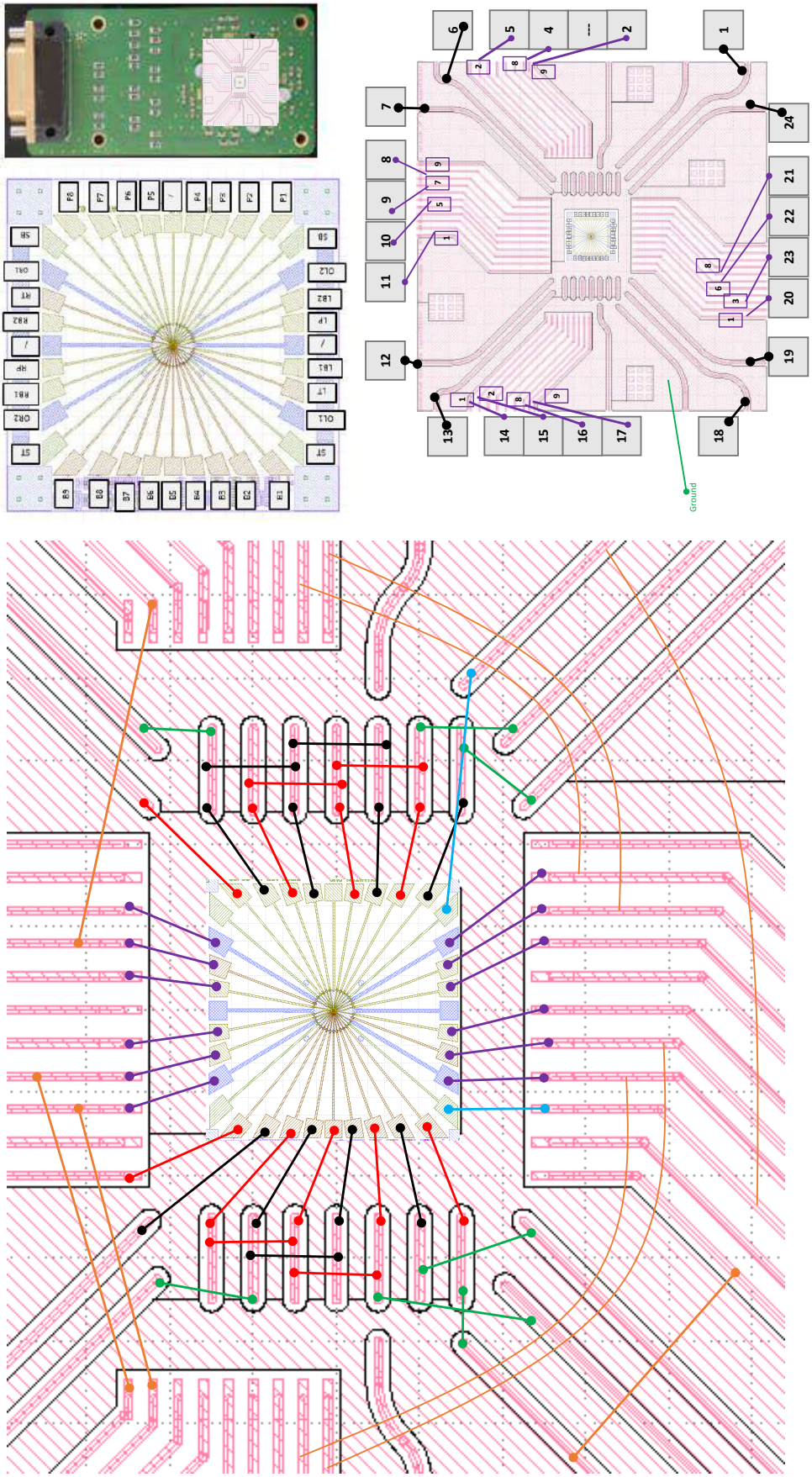

Figure A.3: Bondmap of the interposer version 3.

Appendix B

Frequency correlation plots

This chapter provides additional frequency correlation plots, as mentioned in section 5.4.

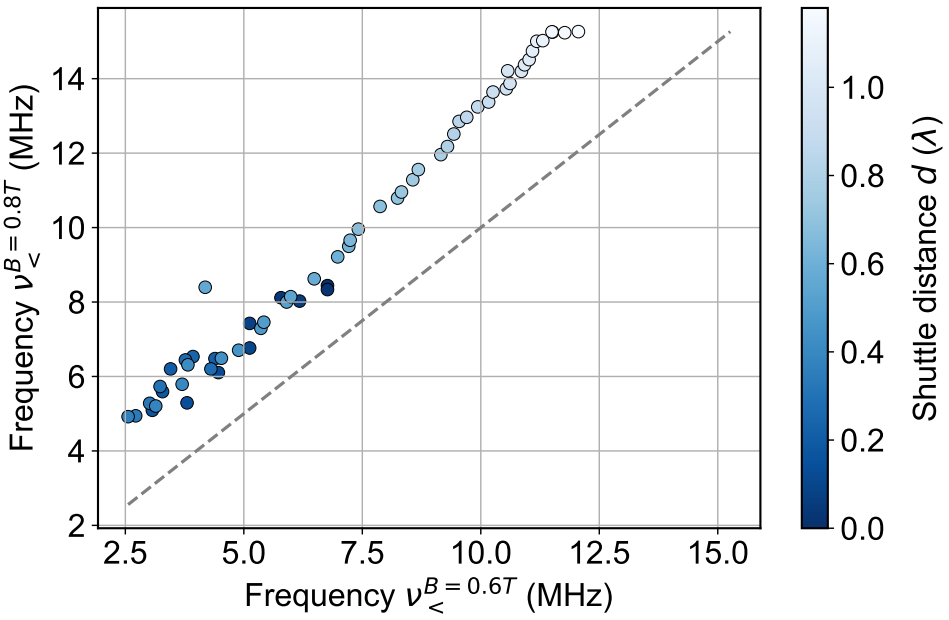

Figure B.1: Frequency correlation plot. One frequency branch from figure 5.15 each is plotted on the axes. The color of the dots indicates at which distance the two frequencies where measured.

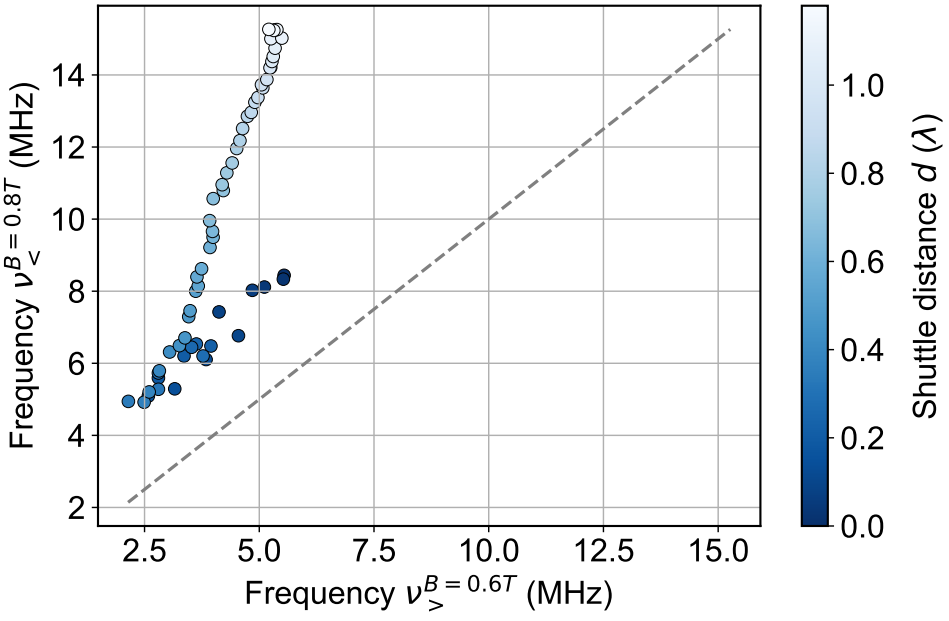

Figure B.2: Frequency correlation plot. One frequency branch from figure 5.15 each is plotted on the axes. The color of the dots indicates at which distance the two frequencies where measured.

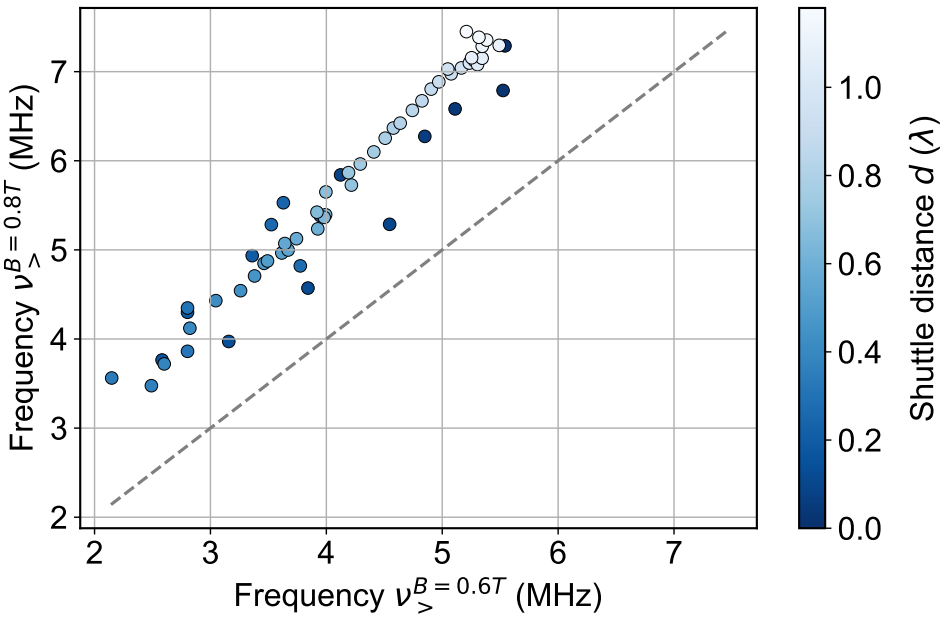

Figure B.3: Frequency correlation plot. One frequency branch from figure 5.15 each is plotted on the axes. The color of the dots indicates at which distance the two frequencies where measured.

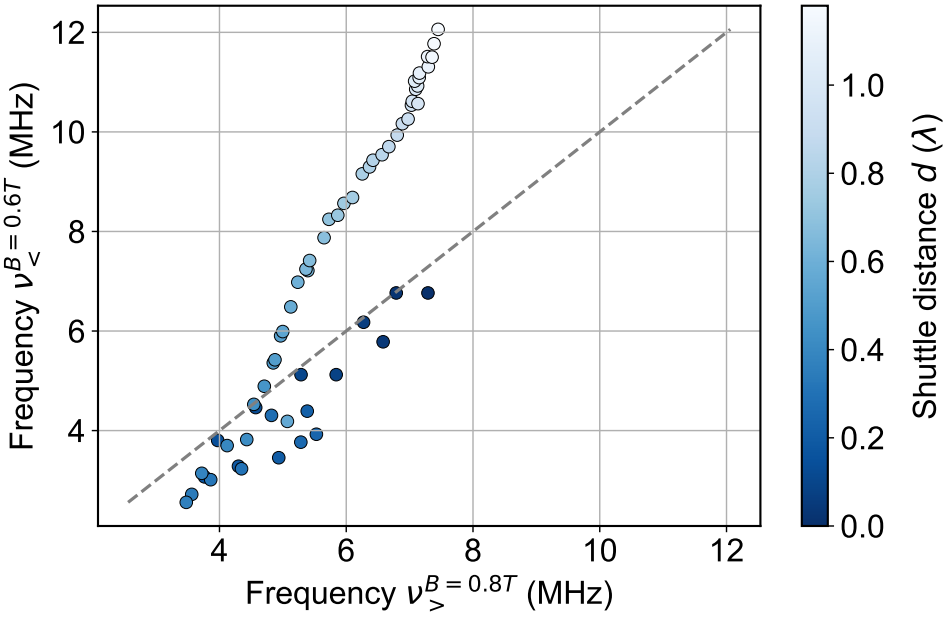

Figure B.4: Frequency correlation plot. One frequency branch from figure 5.15 each is plotted on the axes. The color of the dots indicates at which distance the two frequencies where measured.

Appendix C

Derivations of fit functions for motional narrowing

In this chapter, the formulas $f_1(d)$ and $f_2(d)$ used to describe motional narrowing in section 5.5 will be motivated or derived.

C.1 Motivation of $f_1(d)$

From reference [35], we know that the phase variation $\delta\phi^2$ of a static QD can be written as

$$\delta\phi^2_{\text{static}} = 2\left(\frac{t}{T_2^*}\right)^2, \tag{C.1.1}$$

while for a single, moving quantum dot with a shuttle distance larger than the correlation length the phase variation is

$$\delta\phi^2_{\text{moving}} = 4\left(\frac{t}{T_2^*}\right)^2 \frac{l_C}{d}. \tag{C.1.2}$$

Here, for a single moving QD, the shuttling factor is l_C/d. At this point, we redefine $T_2^* \equiv T_{2,\text{static}}^*$, as in both cases it refers to a static QD. Extending our system now to two QDs, one actually static, and one moving, we can add up the phase variations and rewrite the phase variation of the whole system in a term containing the total dephasing time $T_{2,\text{EPR}}^*$. This yields

$$\left(\frac{1}{T_{2,\text{EPR}}^*}\right)^2 = \left(\frac{1}{T_{2,\text{static}}^*}\right)^2 \left(1 + \frac{l_C}{d}\right), \tag{C.1.3}$$

where a factor containing the static dephasing time was factored out of the sum, leaving behind a one corresponding to the static dot and the shuttling factor corresponding to the moving dot. For our system of an EPR pair, both of these addends have to be modified to yield a correct description of our system. Both of these modifications are heuristic, making the final formula not a rigorous theoretical derivation and rather a phenomenological observation of how the system behaves. For the first addend, we might

have non-negligible influences of exchange interaction and a reduced dephasing time due to charge noise. We incorporate this possibility by promoting the one to an arbitrary variable s^2 with $s \geqslant 1$. Also, as the shuttling factor currently defined as l_C/d would break down for $d = 0$, we account for this effect by modifying the shuttling factor to be $l_C/(d + l_C)$. This modification is negligible for large shuttle distances so that we get back the theoretical prediction for a single moving dot (eq. C.1.2), while for the case of $d = 0$, we get the expected result of an overall factor of two for an EPR pair. With these modifications, we arrive at

$$\left(\frac{1}{T^*_{2,\mathrm{EPR}}}\right)^2 = \left(\frac{1}{T^*_{2,\mathrm{static}}}\right)^2 \left(s^2 + \frac{l_C}{d + l_C}\right). \tag{C.1.4}$$

As s is defined as an arbitrary variable specific to the left, static QD, we can factor the static dephasing time term back in and choose s so that we can identify the fitting function we used.

C.2 Derivation of $f_2(d)$

This section, primarily authored by Łukasz Cywiński, is an unpublished supplement to [67] and is provided for comprehensive coverage.

After a single realisation of the experimental procedure of singlet initiation, separation of electrons, and shuttling of one of them forth by distance d and then back, the expectation value of singlet return probability oscillates as $\cos(2\pi\nu\tau)$, where the frequency $\nu(d)$ is given by Eq. (2) in the main text. We write it as $\nu(d) = \nu_{\Delta g}(d) + \nu_{\mathrm{hf}}(d)$, and assume that the spatial variation of g-factor of the shuttled electron is due to frozen-in disorder. The contribution to frequency from the hyperfine interaction with the nuclear spins, $\nu_{\mathrm{hf}}(d)$, is given by

$$\begin{aligned} h\nu_{\mathrm{hf}}(d) &= \frac{1}{d}\int_0^d \Delta E_{\mathrm{hf}}(x)\mathrm{d}x = \frac{1}{d}\int_0^d [E^L_{\mathrm{hf}} - E^R_{\mathrm{hf}}(x)]\mathrm{d}x \ , \\ &= E^L_{\mathrm{hf}} - \frac{1}{d}\int_0^d E^R_{\mathrm{hf}}(x)\mathrm{d}x \ , \end{aligned} \tag{C.2.1}$$

where E^L_{hf} is the Overhauser field acting on electron in the L dot, while $E^E_{\mathrm{hf}}(x)$ is the Overhaused field acting on the shuttled electron when the expectation value of its position along the channel is x. We have

$$E^L_{\mathrm{hf}} = \mathcal{A}\int |\Psi_L(x' + |x_L|, y', z')|^2 I(x', y', z')\mathrm{d}^3r' \ , \tag{C.2.2}$$

where $\mathcal{A} \approx 2.15$ μeV [98] is the hyperfine coupling to ^{29}Si nuclei, $x_L < 0$ is the position of the L dot, $\Psi_L(x, y, z)$ is the envelope wavefunction of the static electron, and $I_z(x, y, z)$ is the nuclear spin polarization density along the z direction of the external magnetic field.

Note that the envelope wavefunction should be normalized in the the following way [99]

$$\int |\Psi(x,y,z)|^2 \mathrm{d}x\mathrm{d}y\mathrm{d}z = \nu_0 \ , \tag{C.2.3}$$

where $\nu_0 = a_0^3/4$ is the volume of the primitive unit cell (PUC) with $a_0 = 0.54$ nm being the lattice constant of Si. For the Overhauser splitting of the shuttled dot we have an analogous formula:

$$E_{\mathrm{hf}}^R(x_R) = \mathcal{A} \int |\Psi_R(x' - x_R, y, z)|^2 I(x', y', z') \mathrm{d}^3 r \ , \tag{C.2.4}$$

where x_R is the position of the R dot. The nuclear spins fluctuate on the timescale of the whole experiment, but on the timescale of a single shuttling ($\lesssim 1$ μs) they can be considered to be static. The meausured singlet return probabilty signal is then given by

$$\begin{aligned} \langle \cos\left(2\pi[\nu_{\Delta g}(d)\tau + \nu_{\mathrm{hf}}(d)\tau]\right)\rangle = \cos[2\pi\nu_{\Delta g}(d)\tau] \\ \langle \exp(-i2\pi\nu_{\mathrm{hf}}(d)\tau)\rangle \ , \end{aligned} \tag{C.2.5}$$

where $\langle ... \rangle$ denotes an ensemble average over nuclear states in the L dot and along the channel through which the electron is shuttled. At temperatures used in experiment and in absence of dynamical nuclear polarization, the distribution of Overhauser fields experienced by the electron at any location x is a zero-mean Gaussian [100], and the $\langle \exp(-i\phi(d)) \rangle$ term averages to $\exp\left(-\langle \phi^2(d) \rangle / 2\right) = \exp\left[-(\tau/T_2^*)^2\right]$, where

$$\left(\frac{1}{T_2^*(d)}\right)^2 = 2\pi^2 \langle \nu_{\mathrm{hf}}^2(d) \rangle \ , \tag{C.2.6}$$

in which

$$\langle \nu_{\mathrm{hf}}^2(d) \rangle = \frac{1}{h^2} \langle (E_{\mathrm{hf}}^L)^2 \rangle + \frac{1}{h^2 d^2} \int_0^d \int_0^d \langle E_{\mathrm{hf}}^R(x) E_{\mathrm{hf}}^R(x') \rangle \mathrm{d}x\mathrm{d}x' \ , \tag{C.2.7}$$

where we have used the fact due to vanishing overlap between the wavefunctions of the static electron and the shuttled electron in the EPR pair (i.e. $|x_L|$ much larger than the spatial extent of both wavefunctions along x), the Overhauser fields experienced by them are uncorrelated. We can thus write

$$\left(\frac{1}{T_2^*(d)}\right)^2 = \left(\frac{1}{T_{2,L}^*}\right)^2 + \left(\frac{1}{T_{2,S}^*(d)}\right)^2 \tag{C.2.8}$$

where the dephasing time in the L dot is given by

$$T_{2,L}^* = \frac{h}{\sqrt{2}\pi} \frac{1}{\sqrt{\langle (E_{\mathrm{hf}}^L)^2 \rangle}} = \frac{\hbar\sqrt{2}}{\sigma_L} \tag{C.2.9}$$

where σ_L is the standard deviation of the Overhauser splitting of the electron in the L

dot, $\sigma_L = \sqrt{\langle (E_{\mathrm{hf}}^L)^2 \rangle}$. In the same way we can write the contribution to dephasing time of the shuttled electron as $T_{2,S}^* = \hbar\sqrt{2}/\sigma_S(d)$, where

$$\begin{aligned}\sigma_S^2(d) &= \frac{1}{d^2}\int_0^d \int_0^d \langle E_{\mathrm{hf}}^R(x_R) E_{\mathrm{hf}}^R(x'_R)\rangle \mathrm{d}x_R \mathrm{d}x'_R \\ &= \frac{1}{d^2}\int_0^d \int_0^d C_{\mathrm{hf}}(x_R, x'_R)\mathrm{d}x_R \mathrm{d}x'_R \end{aligned} \tag{C.2.10}$$

and where we have defined the autocorrelation function of the Overhauser field along the channel, $C_{\mathrm{hf}}(x_R, x'_R)$. We assume that the shuttled electron envelope wavefunction $\Psi_R(x, y, z)$ has a fixed shape, i.e. the dot does not get deformed during the motion, and that is it separable in x, y, z coordinates. The autocorrelation of the Overhauser field along the channel that appears under the integrals in Eq. (C.2.10) is then given by

$$\begin{aligned} C_{\mathrm{hf}}(x_R, x'_R) = \mathcal{A}^2 \int \mathrm{d}^3 r \int \mathrm{d}^3 r' \langle I_z(x, y, z) I_z(x', y', z')\rangle \\ |\Psi_R(x - x_R, y, z)|^2 |\Psi_R(x' - x'_R, y', z')|^2. \end{aligned} \tag{C.2.11}$$

As $\Psi(\mathbf{r})_R$ is an envelope function that is approximately constant on lengtscale of a_0 and smooth on larger scales, the nuclear polarization density can be treated as "spatial white noise", i.e. its autocorrelation function is

$$\langle I(x, y, z) I(x', y', z')\rangle = \langle I_z^2\rangle \delta(x - x')\delta(y - y')\delta(z - z') \tag{C.2.12}$$

and $\langle I_z^2\rangle = I(I + 1)/3$ which is equal to $1/4$ for $I = 1/2$ pertinent to ^{29}Si nuclear spins. Using this we arrive at

$$\begin{aligned} C_{\mathrm{hf}}(x_R, x'_R) &= \mathcal{A}^2 \langle I_z^2\rangle \int \mathrm{d}^3 r |\Psi_R(x - x_R, y, z)|^2 \\ &\qquad |\Psi_R(x - x'_R, y, z)|^2 \\ &= \mathcal{A}^2 \langle I_z^2\rangle \int |\Psi_R(x, y, z)|^2 |\Psi_R(x + \Delta x, y, z)|^2 \mathrm{d}^3 r \ , \end{aligned} \tag{C.2.13}$$

where we can see that this autocorrelation is in fact a function of $\Delta x \equiv x_R - x'_R$. When evaluated for $\Delta x = 0$ it gives simply σ_R^2, the standard deviation of the Overhauser field experienced by an electron with envelope wavefunction $\Psi_R(x, y, z)$.

Assuming that the confinement potential along x is harmonic, the x-dependent part of the wavefunction is $\Psi(x) \propto \exp\left(-x^2/2L^2\right)$, and we have

$$\int e^{-x^2/L^2} e^{-(x+\Delta x)^2/L^2} \mathrm{d}x \propto e^{-\Delta x^2/2L^2} \ , \tag{C.2.14}$$

from which we get

$$C_{\mathrm{hf}}(\Delta x) = C_{\mathrm{hf}}(0)e^{-\Delta x^2/2L^2} \equiv \sigma_R^2 e^{-\Delta x^2/2L^2} \ . \tag{C.2.15}$$

We see now that L is the autocorrelation length of nuclear-spin induced spatially random spin splitting experienced by the traveling electron. We thus expect an enhancement of $T_{2,S}^*$ time compared to the static dot value of $T_{2,R}^*$ due to motional narrowing when $d \gg L$ [35].

After plugging the above formula for $C_{\mathrm{hf}}(\Delta x)$ into Eq. (C.2.10) we obtain

$$\begin{aligned}\sigma_S^2(d) &= \frac{\sigma_R^2}{d^2}\int_0^d\int_0^d e^{-(x-x'^2)/2L^2}\mathrm{d}x\mathrm{d}x' \ , \\ &= \sigma_R^2\Big[\frac{2L^2}{d^2}(e^{-d^2/2L^2}-1) + \frac{\sqrt{2\pi}L}{d}\mathrm{Erf}\left(\frac{d}{\sqrt{2}L}\right)\Big]\end{aligned} \tag{C.2.16}$$

and the exact formula for $T_2^*(d)$ dephasing time of the EPR pair with one electron shuttled over distance d and back is

$$\left(\frac{1}{T_2^*(d)}\right)^2 = \frac{\sigma_L^2}{2\hbar^2} + \frac{\sigma_S^2(d)}{2\hbar^2} \ , \tag{C.2.17}$$

with $\sigma_S^2(d)$ given by Eq. (C.2.16). Note that the σ_R^2 prefactor in Eq. (C.2.16) is related to the dephasing time for spin in a static R dot by $T_{2,R}^* = \hbar\sqrt{2}/\sigma_R$.

By least-square fitting $T_2^*(d)$ data points in Fig. 2g of the main text with Eq. C.2.16 and C.2.17 (labeled as $f_2(d)$ in Fig. 2g) yields $T_{2,\mathrm{R}}^* = (560 \pm 20)\,\mathrm{ns}$, $T_{2,\mathrm{L}}^* = (1040 \pm 50)\,\mathrm{ns}$ and $L = (8\pm2)\,\mathrm{nm}$. This results in $T_{2,\mathrm{S}}^*(280\,\mathrm{nm}) = (2130\pm220)\,\mathrm{ns}$. These values are close to the values fitted by the fitting function $f_1(d)$ discussed in the main text: $T_{2,\mathrm{L}}^* = (1110\pm90)\,\mathrm{ns}$, $T_{2,\mathrm{R}}^* = (520 \pm 20)\,\mathrm{ns}$ and $T_{2,\mathrm{S}}^*(280\,\mathrm{nm}) = (2460 \pm 310)\,\mathrm{ns}$.

For $d \ll L$ we have

$$\sigma_R^2(d \ll L) \approx \sigma_R^2\left(1 - \frac{d^2}{12L^2}\right) \ ,$$

while for $d \gg L$ we have

$$\sigma_R^2(d \gg L) \approx \sigma_R^2(\frac{L}{d}\sqrt{2\pi} - \frac{2L^2}{d^2}) \ .$$

In the $d \gg L$ regime we thus have

$$\begin{aligned}T_{2,S}^*(d \gg L) &\approx \frac{T_{2,R}^*}{(2\pi)^{1/4}}\sqrt{\frac{d}{L}}\frac{1}{\sqrt{1-\frac{2L}{\sqrt{2\pi}d}}} \ , \\ &\approx \frac{T_{2,R}^*}{(2\pi)^{1/4}}\sqrt{\frac{d+\frac{2L}{\sqrt{2\pi}}}{L}} \ .\end{aligned} \tag{C.2.18}$$

The d-dependence of the above formula is very similar to the dependence of the simple $\sqrt{(d+l_c)/l_c}$ expression used in the main text, explaining the good agreement between fits of $T^*_{2,R}$ and L or l_c to the results of measurements.

Finally, let us note that σ_R^2 given by Eq. (C.2.13) evaluated at $x = x'$ is

$$\sigma_R^2 = \frac{f\mathcal{A}^2}{2N} \quad \rightarrow \quad T^*_{2,R} = \frac{\hbar\sqrt{2N}}{\sqrt{f}\mathcal{A}}$$

where $N = \nu_0 / \int |\Psi_R(x,y,z)|^4 \mathrm{d}^3 r$ is the effective number of primitive unit cells encompassed by the wavefunction, f is the concentration of ^{29}Si (equal to 0.049 in the case of natural Si relevant here), and the factor of 2 comes from two Si atoms per primitive unit cell. If we assume that $\Psi_R(x,y,z) \propto e^{-x^2/2L_x^2} e^{-y^2/2L_y^2}$ and the z dependence is crudely approximated by a square function of width z_0, then using the normalization from Eq. (C.2.3), we obtain $N = 2\pi z_0 L_x L_y / \nu_0$. Assuming $L_y \approx 15\,\mathrm{nm}$ and $z_0 \approx 4\,\mathrm{nm}$, we estimate $T_2^* \approx 760\,\mathrm{ns}$ for $L_x = 8\,\mathrm{nm}$ and $T_2^* \approx 1040\,\mathrm{ns}$ for $L_x = 15\,\mathrm{nm}$ (left QD is not not in the shuttle potential and thus much less confined), which are in reasonable agreement with $T^*_{2,\mathrm{R}}$ and $T^*_{2,\mathrm{L}}$, respectively.

Appendix D

Physics of magnetospectroscopy experiments

This section will further describe the theoretical background of the magnetospectroscopy measurements. Firstly, figure D.1 shows the theoretical prediction of the transition positions and their dependence on the magnetic field. It is evident that E_0, the energy for which zero electrons are in the system, is constant. For one electron in the $|\downarrow\rangle$-state, the energy is proportional to the magnetic field, $E_1 \propto B$, with a slope of $-g\mu_B$. The form of the two-electron energy E_2 arises due to the system being in a singlet state below, and in the T_- state above a certain magnetic field B_{ST}. Below this field, the energy stays constant. Above it declines with a slope of $-2g\mu_B$, as there are now two electrons in the $|\downarrow\rangle$-state. By comparing the zero-and one-electron or one- and two-electron energies, we find the transitions (shown in black) that we measure in practical experiments. An additional sketch of the magnetic field dependent change of the ground state configuration is provided by figure D.2. For each electron number, the electronic states are shown. The spin state of each electron before and after the swap of the ground state is indicated.

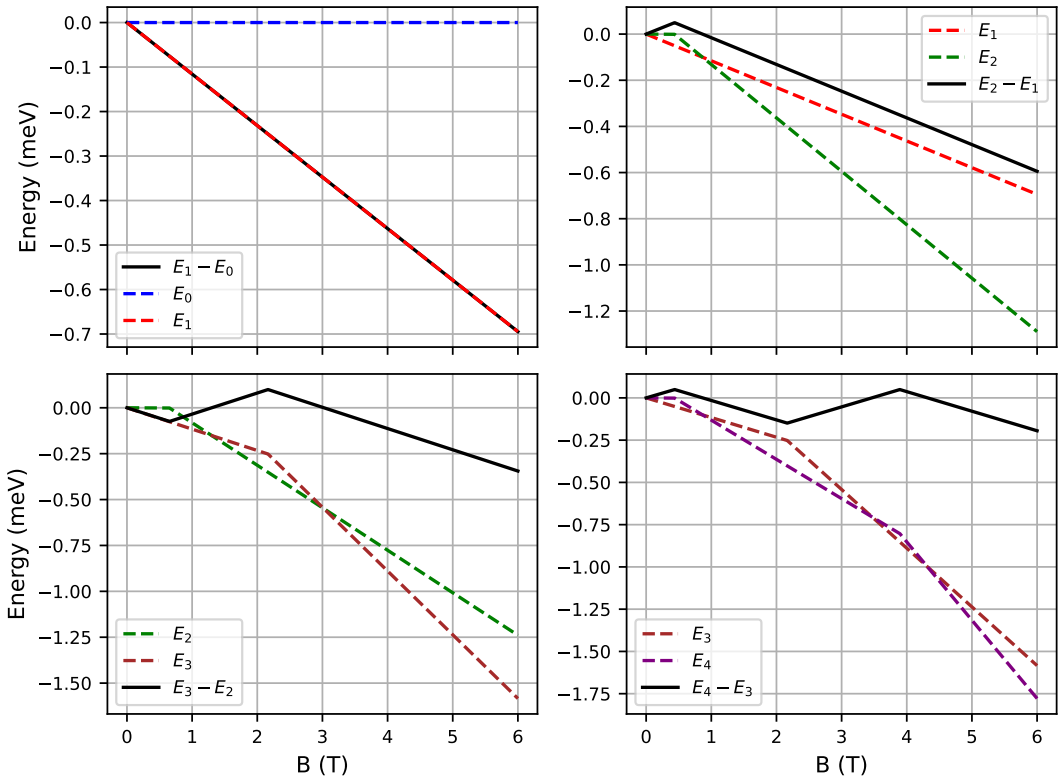

Figure D.1: Sketch of the magnetic field dependent charge transitions of an electron in a QD. The dashed lines show the energies E_i of an i electron system, the solid lines show the behaviour of the transitions. Figure taken from [76].

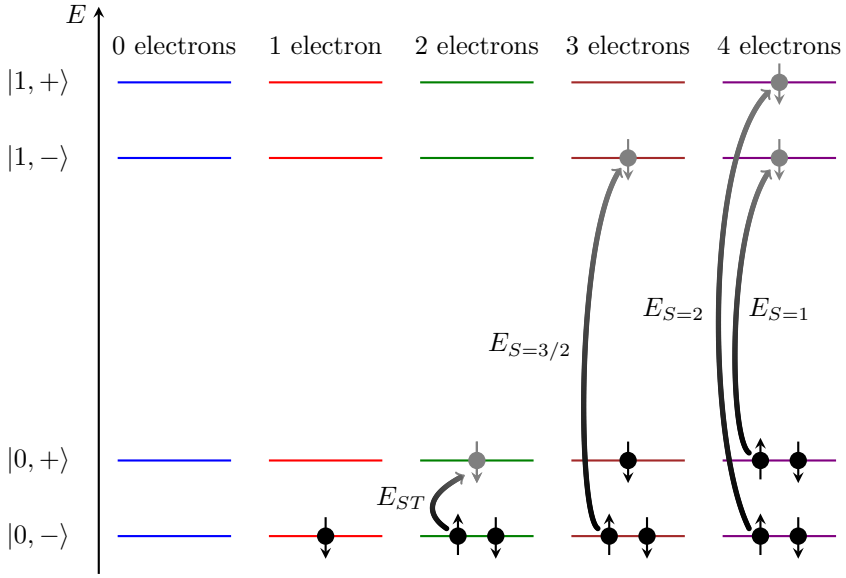

Figure D.2: A schematic illustrating the magnetic field-induced swap in the ground state configuration of a single electron is presented. Electrons depicted solidly represent the ground state charge and spin configuration at $0\,\mathrm{T}$. In contrast, the transparently illustrated electrons showcase the altered ground state that emerges under a specific magnetic field. Figure taken from [76].